

12-14-2023 9:45 AM

Analysis and Characterization of Embroidered Textile Strain Sensors for Use in Wearable Mechatronic Devices

Jose Guillermo Colli Alfaro,

Supervisor: Trejos, Ana Luisa, *The University of Western Ontario*

A thesis submitted in partial fulfillment of the requirements for the Doctor of Philosophy degree
in Biomedical Engineering

© Jose Guillermo Colli Alfaro 2023

Follow this and additional works at: <https://ir.lib.uwo.ca/etd>



Part of the [Systems and Integrative Engineering Commons](#)

Recommended Citation

Colli Alfaro, Jose Guillermo, "Analysis and Characterization of Embroidered Textile Strain Sensors for Use in Wearable Mechatronic Devices" (2023). *Electronic Thesis and Dissertation Repository*. 9868.
<https://ir.lib.uwo.ca/etd/9868>

This Dissertation/Thesis is brought to you for free and open access by Scholarship@Western. It has been accepted for inclusion in Electronic Thesis and Dissertation Repository by an authorized administrator of Scholarship@Western. For more information, please contact wlsadmin@uwo.ca.

Analysis and Characterization of Embroidered Textile Strain Sensors for Use in Wearable Mechatronic Devices

José Guillermo Collí Alfaro

PhD Thesis, 2023

School of Biomedical Engineering
The University of Western Ontario

Abstract

Stroke and musculoskeletal disorders affect hundreds of millions of people around the world. To aid in the recovery process of people affected by these conditions, the use of wearable mechatronic devices has been proposed during traditional rehabilitation therapies. However, factor such as rigidity, increased weight, and overall bulkiness have hindered the adoption of these devices in a clinical setting. Therefore, alternative solutions in the form of soft wearable mechatronic devices have been proposed recently. This is due to these devices being lightweight and comfortable, and compliant, which makes them easier to conform to the human body. To achieve such compliance, high emphasis has been placed on the development of soft sensing mechanisms, as they are in charge of collecting information from the device, the environment and user.

Among these sensing mechanisms, force and motion sensors have been extensively studied, as they are the simplest to integrate in wearable mechatronic devices. However, the majority of these sensors have been developed using soft materials that are not breathable and can cause skin irritations due to the materials used to fabricate them. For these reasons, textile sensors have been proposed as an alternative. Among these textile solutions, embroidered sensors have shown great potential, as they are relatively simple to manufacture and have high scalability characteristics. Unfortunately, embroidered sensors have the disadvantage of not being stretchable, which is one of the many characteristics of motion and force sensors. To address these issues, this thesis focuses on the design, development, characterization, and performance assessment of stretchable embroidered textile strain sensors.

To this end, a framework for the development of embroidered textile strain sensors was proposed. This framework included all the necessary steps to design and fabricate these sensors. To

achieve the required stretchability of embroidered sensors, a set of customizable parameters were included within this framework. Then, following the guidelines of the proposed framework, a novel embroidered strain sensor was created using a honeycomb pattern. This pattern had two main purposes: a distribution of the axial forces across the walls of the honeycomb design to protect the conductive thread; and the addition of stretchiness to the embroidered sensor. Sensors created using this pattern were embroidered onto an elastic band and then attached to a strain compensation system to increase the stretchability of the sensor further. After 50 stretching cycles, sensors showed good linearity, an average gauge factor of 0.24, an average hysteresis of 36.85% and up to 55.56% working range. This demonstrated the ability of the embroidered sensor to work as a strain sensor, without showing signs of damage and without showing signs of deformation.

Lastly, a series of embroidered sensors were fabricated using a Kirigami design. These sensors were created to measure forces under dynamic conditions. Before testing, these sensors were attached to a strain compensation mechanism, which in turn was attached to a force sensing device that served as ground truth for the data collected by the embroidered sensors. The embroidered sensors were tested under three different speed profiles: slow speed, medium speed, and high speed. On each speed profile, each sensor showed high linearity, a low hysteretic behaviour, and relatively good repeatability. These results established the capabilities of the embroidered strain sensors as force sensors that could be used inside soft wearable mechatronic devices.

Keywords — Soft wearable mechatronic devices, embroidered textile sensors, textile strain sensors, textile force sensors.

Lay Summary

Many people worldwide have conditions or disabilities that significantly impact their movement capabilities and their ability to participate in desired physical activities. To help them get better, therapists have been looking into implementing special robots that can be worn by the patients. However, because these robots are too heavy and bulky, many researchers have been studying ways to make these robots softer and lighter. One of the many solutions that have been found is to use embroidered devices that can detect movements and forces of people wearing the robot. However, in order for the embroidered device to detect movements and forces, they need to be able to stretch. This is why the goal of this thesis was to develop an embroidered device that was able to stretch in order to detect movements and forces. The first step to achieve this goal was to create a series of guidelines to create these embroidered devices. Then using these guidelines, several embroidered devices were created using a honeycomb design, as this design added stretchability to the embroidered device, while at the same time protecting it from breaking. After testing the embroidered devices for many stretching cycles, it was found that they were able to detect movements without many issues. Finally, other embroidered devices were created using a design with cuts, which allowed the embroidered device to stretch. To test the embroidered devices, they were stretched at different speeds. The forces acting on the embroidered devices were measured at each speed. After looking at the measured force information, it was observed that the embroidered devices were able to detect forces consistently and without breaking.

Dedicated to:

My dearest parents and my lovely wife

Acknowledgements

First and foremost, I would like to express my deepest and heartfelt gratitude to my supervisor, Dr. Ana Luisa Trejos. No words can express the amount of support I felt while working under your supervision, so thank you for being the most caring, kind, and extraordinary supervisor throughout my journey as a PhD student. I would also like to thank all of the members that are and have been part of the Wearable Biomechatronics Laboratory, thank you for making a really amicable and wonderful environment.

A special thanks goes to Yue Zhou and Anas Ibrahim, for all of those coffee trips to the UCC and all those times when we used to play ping pong while also discussing potential solutions to our research problems. Also, I would like to acknowledge Brandon Edmonds, for all those morning discussion that helped kick off the day. It was a pleasure working with you. A big thanks goes to Jacob Tryon, for being a really good friend inside and outside of the lab. Thank you for bringing so much joy to the lab. To Alex Lizotte and Sergio Salinas, thank you for all those social reunions that helped me focus on something else besides work.

I would also like to thank all the members of my advisory committee, Dr. Katarina Grolinger, Dr. Vijay Parsa, and Dr. George Knopf, for their valuable input during my committee meetings. Also, a big thanks goes to Eugen Porter, for always having the patience and willingness to help me whenever I had questions about my electronic designs.

To my parents, Militza Alfaro Gamboa and José Luis Collí Solís, thank you very much for your constant love and support, and for encouraging me to follow my dreams. Thank you, because even when we were far away, I knew I could always count on you. Los amo y los extraño.

To my lifelong friends Rocio, Shamir, Genny, Gabriel, David, Andrés, and Mariana. Thank

you for always being there to chat any day, at any time.

To my cat Purr, for being the best classmate I had during the time period of virtual classes. And last but not least, to my wife Maremy Castillo Ocampo, I have nothing but my most sincere appreciation for all the love you have given me during this journey. Thank you for all the kind words, for all the hugs, for all the laughs, and for all the times you were there when I needed you the most. I love you.

This work would not have been possible without the generous funding provided by the Natural Sciences and Engineering Research Council (NSERC) of Canada under grant RGPIN-2020-05648; by the Canadian Foundation for Innovation (CFI), by the Ontario Research Fund (ORF), and by the Canada Research Chairs Program under File #950-233069. I am also grateful to the Mexican National Council of Humanities, Science, and Technology (CONAHCYT) for funding my graduate studies.

Contents

Abstract	ii
Lay Summary	iv
Acknowledgements	vi
Table of Contents	viii
List of Figures	xii
List of Tables	xiv
1 Introduction	1
1.1 Motivation	2
1.2 General Problem Statement	2
1.3 Research Objectives and Scope	4
1.4 Overview of the Thesis	4
2 Literature Review	6
2.1 Introduction	6
2.2 Upper-limb Wearable Mechatronic Devices	6
2.3 Upper-Limb Soft Wearable Mechatronic Devices	8
2.4 Textile Strain Sensors Manufacturing Methods	8
2.4.1 Yarn Manufacturing	9

2.4.2	Dip Coating	10
2.4.3	Screen Printing	10
2.4.4	Electroless Plating	10
2.4.5	Vapor Deposition	11
2.4.6	Knitting and Stitching	11
2.5	Textile Sensors Modes of Operation	12
2.5.1	Resistive Textile Strain Sensors	12
2.5.2	Capacitive Textile Strain Sensors	13
2.5.3	Inductive Textile Strain Sensor	13
2.6	Textile Strain Sensors Sensing Mechanisms	13
2.6.1	Crack Propagation	14
2.6.2	Mechanical Deformation	14
2.7	Concluding Remarks	15
3	Design and Fabrication of Embroidered Textile Strain Sensors: An Alternative to Stitch-Based Strain Sensors	16
3.1	Introduction	16
3.2	Fabrication of Embroidered Textile Strain Sensors	20
3.2.1	Computer-Aided Design (CAD) Model	21
3.2.2	Digitization	22
3.2.3	Embroidery	23
3.2.3.1	Fabric Substrate	23
3.2.3.2	Conductive Thread	24
3.2.3.3	Stabilizer Substrate and Embroidery Needle	25
3.2.4	Embroidered Textile Strain Sensor	26
3.3	Performance Evaluation Metrics	27
3.3.1	Experimental Setup	30
3.4	Results	31
3.4.1	Working Range	31

3.4.2	Linearity	33
3.4.3	Sensitivity and Hysteresis	35
3.4.4	Repeatability	36
3.4.5	Reproducibility	37
3.5	Discussion	39
3.5.1	Working Range	39
3.5.2	Linearity	41
3.5.3	Sensitivity	42
3.5.4	Repeatability and Hysteresis	43
3.5.5	Reproducibility	45
3.6	Conclusions and Future Work	46
4	Performance Evaluation of Embroidered Honeycomb Textile Strain Sensors	49
4.1	Introduction	49
4.2	Materials and Methods	52
4.2.1	The Honeycomb Model	52
4.2.2	Sensor Fabrication	53
4.2.3	Hardware Interface	56
4.2.4	Experimental Setup	58
4.3	Results	61
4.3.1	Linearity and Working Range	61
4.3.2	Sensitivity	62
4.3.3	Hysteresis	63
4.3.4	Repeatability	64
4.4	Discussion	64
4.5	Conclusions and Future Work	67
5	Effects of Dynamic Forces on Embroidered Textile Strain Sensors	68
5.1	Introduction	68
5.2	Materials and Methods	70

5.2.1	Mechanical Characteristics of the Kirigami Pattern	70
5.2.2	Sensor Fabrication	72
5.2.3	Sensor Characterization	74
5.2.4	Experimental Setup	78
5.2.5	Dynamic Motion Tests	79
5.2.6	Signal Processing	80
5.3	Results	80
5.4	Discussion	84
5.5	Conclusions and Future Work	87
6	Concluding Remarks	89
6.1	Contributions	91
6.2	Future Work	93
	References	96
	Appendices	106
A	Permissions and Approvals	106
	Vita	107

List of Figures

2.1	An example of a wearable mechatronic device.	7
2.2	Examples of fibres and yarns.	9
3.1	Stitching and embroidery examples.	18
3.2	Appearance of a zigzag stitch on both sides of the fabric.	19
3.3	Design process of the embroidered textile strain sensor.	21
3.4	Examples of textile structures.	24
3.5	Digital representation of the embroidered textile strain sensor.	26
3.6	First prototype of the embroidered textiles strain sensor.	27
3.7	Strain sensor change in resistance due to strain.	29
3.8	Experimental setup used on the first textile strain sensor prototype.	30
3.9	First textile strain sensor prototype: Sensor S1 strain data over multiple stretching cycles.	32
3.10	First textile strain sensor prototype: Sensor S2 strain data over multiple stretching cycles.	32
3.11	First textile strain sensor prototype: Sensor S3 strain data over multiple stretching cycles.	33
3.12	First textile strain sensor prototype: linearity results for Sensor S1.	34
3.13	First textile strain sensor prototype: linearity results for Sensor S2.	34
3.14	First textile strain sensor prototype: linearity results for Sensor S3.	35
3.15	First textile strain sensor prototype: sensor drift over the course of 100 stretching cycles.	37

3.16	Average DTW cost across the three sensor samples of the first embroidered sensor prototype for Cycles 10 to 100.	38
3.17	Loops underneath the fabric substrate.	41
3.18	Rearrangement of fibres within the conductive thread used.	44
3.19	Data similarities assessed by applying the DTW technique on the resistance data of each sensor pair.	45
3.20	Data similarities assessed by applying the DTW technique on the resistance data of each sensor pair for Cycle 40.	46
4.1	Example of a honeycomb pattern based on an hexagonal unit cell.	52
4.2	Deformation of the honeycomb cell due to stretching in the horizontal plane. . . .	53
4.3	Rectangular shape honeycomb sensor fabrication process.	55
4.4	Embroidered textile strain sensor hardware interface.	56
4.5	Strain divider system.	59
4.6	Linear motion testing setup used during data collection of each sensor sample. . .	60
4.7	Slack on sensor due to deformation produced by overstretching.	60
4.8	Second textile strain sensor prototype: sensors response in the presence of strain. .	62
4.9	Stitch deformation on embroidered sensor.	66
5.1	Dimensions of a Kirigami design and its response in presence of strain.	71
5.2	Fabrication process of the embroidered sensors for force sensing.	74
5.3	Testing and characterization of an embroidery dummy sensor.	76
5.4	The strain compensation mechanism.	77
5.5	Testing setup used for data collection of the embroidered force sensor.	79
5.6	Average linear response of each of the three forces sensor samples at each speed profile.	81
5.7	Force sensors drift over each stretching cycle at the three speed profiles.	84

List of Tables

3.1	First textile strain sensor prototype: average sensor performance metrics.	36
3.2	Performance comparison of stitched sensors and the first prototype of the embroi- dered sensor.	39
4.1	Base resistance and compensation voltages measured for the sensor samples.	61
4.2	Average performance metrics of each sensor average data.	64
5.1	Average performance metrics of each sensor at 30 bpm.	83
5.2	Average performance metrics of each sensor at 60 bpm.	83
5.3	Average performance metrics of each sensor at 90 bpm.	83
6.1	Summary of the performance metrics of the three sensor types developed in this thesis.	91

Nomenclature

Acronyms

ADC	Analog to Digital Converter
ADL	Activities of Daily Living
bpm	Beats Per Minute
CAD	Computer-Aided Design
CNT	Carbon Nanotubes
DAQ	Data Acquisition
DTW	Dynamic Time Warping
DXF	Drawing Exchange Format
FCN	Fully Convolutional Network
GF	Gauge Factor
GRU	Gated Recurrent Units
ICF	Indirect Current Feedback
IMU	Inertial Measurement Unit
In-Amp	Instrumentation Amplifier
LSTM	Long Short-Term Memory
MAV	Moving Average

MSD	Musculoskeletal Disorders
PDMS	Polydimethylsiloxane
PEDOT	Poly(3,4-ethylenedioxythiophene)
PPy	Polypyrrole
PVB	Polyvinyl Butyral
spm	Stitches Per Minute
SWCNT	Single-Wall Carbon Nanotubes
TCN	Temporal Convolutional Network
TPU	Thermoplastic Polyurethane

Units

Ω	Ohms
$^{\circ}$	Degrees
A	Amperes
C	Celsius
cm	Centimetres
kHz	Kilohertz
m	Metres
mm	Millimetres
mm/min	Millimetres per minute
N	Newtons
N/m	Newtons/metres
V	Volts
V/N	Volts/Newtons

Chapter 1

Introduction

Musculoskeletal disorders (MSD) and neurological conditions, such as stroke, affect hundreds of millions of people around the world [1,2]. Furthermore, it is estimated that at least 55% of stroke survivors suffer from some sort of disability that impairs their ability to perform well during their activities of daily living (ADL) [3]. Therefore, it is imperative for MSD and stroke patients to engage in a series of rehabilitation therapies to regain some motor functions. Although traditional rehabilitation therapies have shown a positive effect on the patients' recovery, further improvements in the rehabilitation outcomes can be achieved when these therapies are used alongside robot-assisted technologies [4].

With respect to the upper-limbs, wearable mechatronic devices, or smart wearable devices, are an emerging type of robotic technology that can be used during these therapies. These devices have the advantage of providing personalized rehabilitation programs to MSD and stroke patients, as wearable devices can make the necessary adjustments in terms of forces and torques required to assist patients. Furthermore, given their portability capabilities, these devices have the potential to extend the rehabilitation therapies beyond clinical settings. However, in order for these smart devices to work properly, it is necessary to apply effective control strategies, which will dictate not only the mechanical behaviour of the system, but also the human-robot interactions [5]. In this sense, these smart devices must be able to collect and interpret data collected from the users, in order to enhance the rehabilitation outcomes in a safely manner.

1.1 Motivation

Despite having the potential to enhance rehabilitation therapies, the widespread adoption of upper-limb wearable mechatronic devices as a complementary method to traditional rehabilitation therapies is still pending. This is mainly because upper-limb wearable mechatronic devices present several challenges in terms of bulkiness, comfort, control strategies, and costs associated with the development of these devices [6, 7].

To address some of these issues, soft robotic devices have been proposed as an alternative to rigid wearable mechatronic devices. Within these soft devices, great attention has been placed on their sensing mechanisms. This is in large part due to sensors having the tasks of collecting information from the user, the environment, and the wearable mechatronic device itself; and to use these data to dictate the behaviour of the mechatronic device [7, 8]. Among the different sensing modalities used to provide feedback to the soft wearable mechatronic device, motion sensing and force sensing stand out due to them being easier to integrate within the wearable system [9]. In addition, force and motion sensing are often used in a multi-sensor configuration to track the interaction between MSD and stroke patients with the environment, and provide clinicians with a general idea of the gradual recovery of their patients [8]. Furthermore, having the ability to monitor patients outside of a clinical environment allows for a more realistic understanding of the patients' performance during ADLs. Although motion and force sensing add favourable characteristics to soft wearable robots, challenges exist regarding integration of these types of sensors in a comfortable and unobtrusive way.

1.2 General Problem Statement

As stated before, motion sensing and force sensing are two of the sensing modalities that are often used in soft wearable mechatronic devices. Among these types of sensors, inertial measurement units (IMUs) have been extensively used in the past [10–13], as their size makes them suitable for embedding them into garments that can be worn comfortably by MSD patients. Unfortunately, the performance of the IMUs is affected by cumulative errors produced due to integration of its accelerometer data to estimate positions [14]. Also, IMUs need to be placed at specific locations on

the human body, which equates to constant recalibration procedures. All of these issues can lead to sensor misreadings and an improper interpretation of the data. Other type of sensors that can be integrated onto garments are bending sensors [3, 15, 16], which show a change in resistance in presence of bending motions. Unfortunately, the accuracy of this type of sensors is also affected by changes in their location on the wearable systems [17]. Furthermore, the constant bending cycles can lead to sensor failure due to fatigue. With respect to force sensors, several studies [3, 18, 19] have implemented them in wearable mechatronic devices to measure the user–robot interactions so that these devices can provide the required assistance needed. However, one flaw with these sensors is that most of the times they are used as pressure sensors due to their non-stretchable characteristics. Other times, when used to measure forces exerted on the device, some studies have implemented load cells to measure forces. However, due to the physical characteristics of the load cells, they need to be well protected, which adds to the bulkiness of the wearable device [9].

Therefore, alternative solutions in the form of soft polymer-based sensors have been proposed. These sensors are typically made by combining a polymeric matrix with conductive nanoparticles. Usually, the stretchable matrix is made of polymers such as thermoplastic polyurethane (TPU), polydimethylsiloxane (PDMS), Ecoflex, among others. As for the conductive materials used for flexible sensors, different materials including carbon nanotubes (CNTs), carbon fibres, silver nanoparticles, and graphene sheets are typically chosen as viable candidates [20, 21]. Although promising, these solutions can bring discomfort due to the lack of breathability of the materials used. Furthermore, some users may present skin irritations due to allergic reactions to the materials used during the fabrication of these types of sensors [22].

Recently, textile-based sensors have been explored as a potential solution to the issues surrounding polymer-based strain sensors. Among these textile-based solutions, embroidered sensors have been gaining popularity due to their relatively simple manufacturing process, mass scalability, and ability to be directly embedded onto garments. Furthermore, these sensors are breathable, which makes them great candidates for long term use in applications involving soft wearable mechatronic devices. However, the biggest challenge with embroidered sensors is their limited stretchable capabilities. Therefore, it is paramount to find solutions aimed towards enhancing the stretchability of embroidered sensors so that they can be used alongside soft wearable mechatronic devices.

1.3 Research Objectives and Scope

This thesis specifically focuses on the development of soft strain sensors using the embroidery technique. The main goal is to demonstrate the feasibility of embroidered strain sensors as an alternative to other textile-based solutions. To achieve this goal, the following objectives have been established:

1. To provide a framework for the development of embroidered textile strain sensors, including the necessary parameters to consider when transitioning from concept to final sensor prototype.
2. To analyze the performance of embroidered textile strain sensors under cycling conditions when embroidered using a stretchable pattern.
3. To evaluate the feasibility of using the embroidered textile strain sensor as a force sensing element in the presence of dynamic motions.

1.4 Overview of the Thesis

The structure of this thesis is summarized in the outline below:

- | | |
|------------------|---|
| Chapter 2 | Literature Review: Presents a review of wearable mechatronic devices used in rehabilitation, as well as some of the methods aimed towards the implementation of soft sensing solutions used within wearable devices. |
| Chapter 3 | Design and Fabrication of Embroidered Textile Strain Sensors: An Alternative to Stitch-Based Strain Sensors: Presents a framework for the fabrication of embroidered resistive textile strain sensors. It also provides information about specific aspects to consider when developing strain sensors using the embroidery technique. |

-
- Chapter 4** Performance Evaluation of Embroidered Honeycomb Textile Strain Sensors: Proposes a method for achieving stretchability in resistive embroidered textile strain sensors using a honeycomb design. In this chapter, the effects of the honeycomb pattern on the textile strain sensor are analyzed in terms of working range, linearity, sensitivity and repeatability.
- Chapter 5** Effects of Dynamic Forces on Embroidered Textile Strain Sensors: Demonstrates the application of the embroidered textile resistive sensor as a force sensor. The chapter discusses the steps required to achieve force sensing, including the creation of the sensor using a Kirigami design, which allowed the sensor to achieve stretchability and robustness. To show the effectiveness of the sensor as a force sensor, the performance of the sensor is analyzed under dynamic motion conditions.
- Chapter 6** Conclusion and Future Work: Emphasizes the contributions of this work and provides recommendations for future work.
- Appendix A** Permissions and Approvals: Includes the permissions and approvals for the copyrighted material used throughout this document.

Chapter 2

Literature Review

2.1 Introduction

This chapter presents a review of the literature in the areas of wearable mechatronic devices (Section 2.2) and soft wearable mechatronic devices (Section 2.3) used in upper-limb robot-assisted therapies. In Section 2.4, some of the methods for fabrication of textile strain sensors are presented. Section 2.5 discusses the different changes in the electrical characteristics of textile strain sensors; and Section 2.6 describes the sensing mechanisms of textile strain sensors. A literature search was conducted using Google Scholar from January 2020 to October 2023. The keywords used in the search included combinations of the following: upper limb rehabilitation, soft wearable mechatronic devices, e-textiles, and textile strain sensors. A total of 131 papers and books were incorporated into the literature review.

2.2 Upper-limb Wearable Mechatronic Devices

As mentioned in Chapter 1, the ultimate goal of robot-assisted therapies is to enhance the rehabilitation outcomes of MSD and stroke patients. One type of robotic devices used to improve the recovery of these patients are upper-limb wearable mechatronic devices. These devices are designed in such a way that they can be attached directly to the patient's affected limb (Figure 2.1). Furthermore, the way upper-limb wearable mechatronic devices assist patients during their reha-

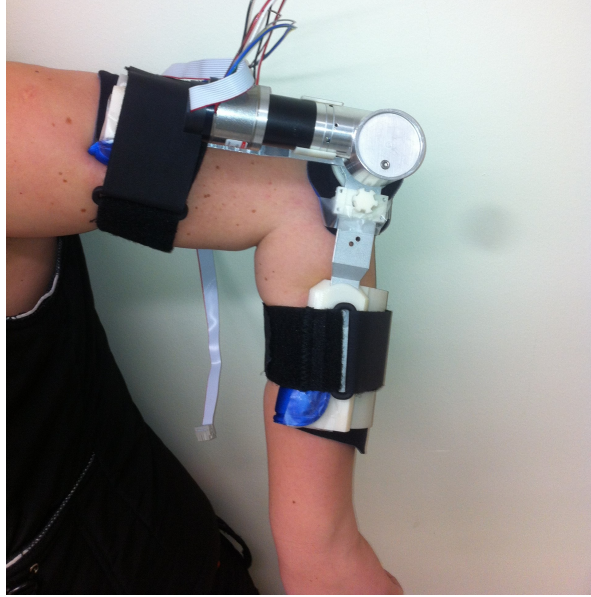


Figure 2.1: An example of a wearable mechatronic device attached to the arm of a user.

bilitation therapies is by providing the required forces to complete a desired task. Depending on the rehabilitation therapy, the mode of operation of the upper-limb wearable mechatronic devices can be resistive, assistive, or corrective [23–25]. During resistive mode, the wearable device will oppose the motion of the wearer, with the purpose of increasing the force required by the user to complete the motion. On the other hand, when the wearable robot is set to the assistive mode, it will help the user perform an action by providing the required forces to achieve the desired motion. Finally, while in corrective mode, the wearable mechatronic device will help the user to complete the desired motion within a predefined region to avoid motion compensations. If the user starts to deviate from the desired motion region, the wearable mechatronic device will produce forces that will help the user stay on track [24].

Although several upper-limb wearable mechatronic devices have been developed in recent years [26–28], they have the particularity of being bulky, expensive, and rigid, which make them less attractive for applications outside of the clinical setting, such as in-home rehabilitation. This is the reason why more recent studies have opted for the development of soft wearable solutions that can be compliant and comfortable to wear.

2.3 Upper-Limb Soft Wearable Mechatronic Devices

As mentioned before, soft wearable mechatronic devices have the advantage of easily conforming to the human body due to them being inherently compliant. The fact that they do not require precise alignment to the joints, are lightweight, and do not constrain the mobility of the wearer, makes them an attractive choice for robot-assisted therapies. For the upper limb, several studies have developed and tested different soft wearable mechatronic devices. In the study by Choi *et al.* [29], a soft wrist wearable mechatronic device was used in a corrective mode to help hemiplegic patients with exercises involving dart throwing. In [30] a soft pneumatic glove was used to assist with hand grasping motions. Similarly, in [3], a soft wearable mechatronic device was used to aid hemiparetic patients during mirror therapies. Furthermore, some studies have implemented soft wearable devices to assist with shoulder adduction [31,32], with others focusing on the assistance of the upper limb as whole [33].

Even though great advancements have been achieved within the field of upper-limb soft wearable mechatronic devices, there are still challenges that need to be addressed. Among these challenges is the implementation of right control strategies that allow for a simple interaction between the user and the device itself [6]. In this sense, the soft robotic device must be able to understand what the user is trying to do in order to provide the right amount of assistance needed. This is the reason why a large emphasis has been placed on the development of soft sensors that are able to track the wearer motions and to detect the interaction forces.

2.4 Textile Strain Sensors Manufacturing Methods

There are several ways to implement a soft sensing mechanism that is able to track the user's motion and detect the interaction forces between the environment, the wearable mechatronic device, and the user. The simplest method is to use textile strain sensors, as they have the unique characteristics of being breathable and preventing skin irritations. These characteristics help textile strain sensors with the comfort of the mechatronic device. Contrary to hard sensors, textile sensors can be directly embedded onto a garment, which helps with the reduction of the overall bulkiness of the wearable mechatronic device. As far as the fabrication of textile strain sensor

goes, these sensors can be created using some of the methods described below.

2.4.1 Yarn Manufacturing

The simplest fabrication method of textile strain sensors consists of using conductive yarns. These yarns are made from fibres, which are typically created using natural materials such as cotton or wool, or synthetic materials such as nylon or polyester [34]. Also, fibres can be divided into two main categories: filament fibres and staple fibres. The main difference between these two fibres is that filament fibres are characterized for having a long and continuous length (Figure 2.2a), whereas staple fibres are significantly shorter in length (Figure 2.2b). When a group of fibres are twisted together, the resulting product is a yarn. Depending on the type of fibres that were twisted together, these yarns will have a regular geometry that produces a perfectly helical shape (Figure 2.2c); or they may not be completely entangled, resulting in irregularities along the length of the yarn (Figure 2.2d) [35].

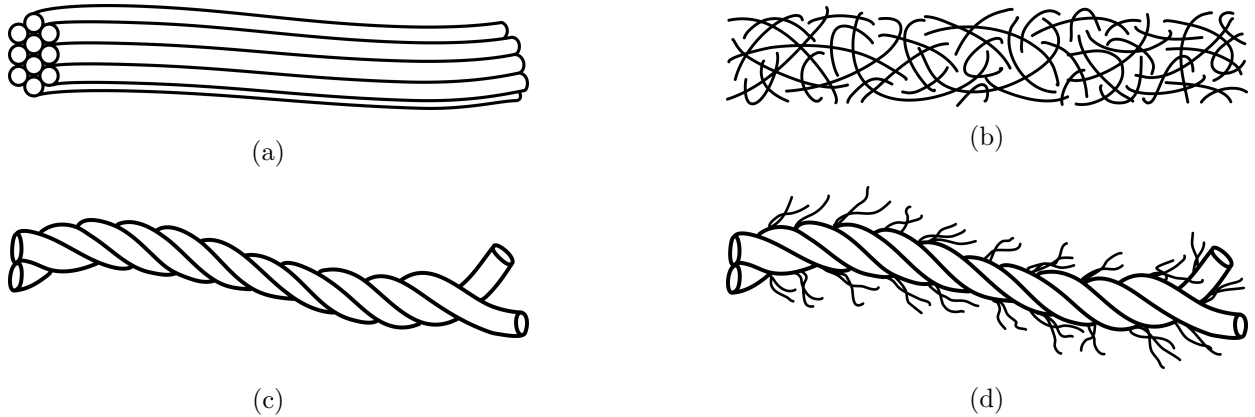


Figure 2.2: Examples of the different fibres and yarns used for the fabrication of textile strain sensors. (a) Filament fibres. (b) Staple fibres. (c) Yarn made from filament fibres. (d) Yarn made from staple fibres.

To make conductive yarns two processes can be used: wire drawing and metal coating. The first method consists of transforming the raw metals (copper, steel, silver, etc.) into small microfilaments, that are later annealed, and finally wrapped around a revolving cylinder [36]. This produces a series of staple fibres that are twisted together to form the conductive yarn. The second method for fabricating conductive yarns consists of coating the bare fibres or the yarn with a layer

of conductive material. This procedure is typically applied to filament fibres or yarns, and the conductive coatings that are commonly used are made of silver, PEDOT [37], single-wall carbon nanotubes (SWCNTs) [38], or polypyrrole (PPy) [39].

2.4.2 Dip Coating

One of the simplest methods to provide conductivity to fabrics and yarns is through dip coating. As the name implies, this process consists of submerging the fabric or yarns into a solution containing a conductive material, and then drying the coated material for a set amount of time. Different materials have been used inside the conductive solution, some of them include SWCNTs [40], PEDOT [37], reduced graphene oxide (rGO) [41], among others. Regardless of being the simplest method of fabrication, special attention should be placed on each stage of the coating process, as dipping the fabric for a short duration, or drying it for too long, can affect the quality of the conductive properties of textiles strain sensors fabricated using this method [42].

2.4.3 Screen Printing

Similar to dip coating, screen printing is another simple method used for the fabrication of conductive yarns or fabrics used by textile strain sensors. Screen printing consists of depositing a small layer of conductive ink on top of a fabric substrate, with the most common inks used being PEDOT-based inks [43, 44] and silver nanoparticles [36]. However, one of the drawbacks of screen printing is that the quality of the conductive layer is dependent on factors such as viscosity and curing temperature of the conductive ink [44], as well as the amount of penetration of the ink on the fabric substrate [36].

2.4.4 Electroless Plating

Another popular method for the manufacturing of textile strain sensors is called electroless plating. This method is similar to electrodeposition in the sense that the deposition of metal particles occurs via the reduction of metal ions. However, the main difference between both methods is that during electroless deposition, there is no need for an electrode that carries current, as electroless deposition is a redox reaction [45]. Although this method can be applied to both staple fibre yarns

and filament fibre yarns, it is recommended that this method is used on filament yarns, such as synthetic yarns, as they are less expensive to fabricate [44]. It is important to note that even when electroless plating allows the yarns to be conductive in all directions, the durability of the metal coating will always be affected by prolonged exposure to air and water.

2.4.5 Vapor Deposition

Similar to electroless plating, vapor deposition is a method used to add conductivity to fabrics or yarns by applying a layer of metallic particles on the surface of the material. This is achieved by enclosing the fabric and the material to be deposited into a vacuum chamber. Then through sputtering, the metallic material is converted into a vapor of small metallic particles that get deposited on the surface of the fabric substrate [46]. Although effective, this method has a big flaw: most of the conductive material gets lost during the vaporisation process. Furthermore, the need of specialized equipment to achieve the vapor deposition makes this method one of the most expensive methods for creating textile strain sensors [44].

2.4.6 Knitting and Stitching

The final two methods of fabrication of textile strain sensors are knitting and stitching. These methods are the most simple ones in the sense that they do not necessarily need to go through any of the previously mentioned methods. Instead, textile strain sensors can be created by using a conductive yarn or fibre that was previously coated with a metallic element. However, it is also possible that non-conductive fibres and yarns could be used to create a textile structure using knitting or stitching. In this case the textile strain sensor would have to be created by coating the knitted or stitched structure with a conductive material using any of the methods previously mentioned.

In the case of knitted structures, they are created by interconnecting a series of loops. When the loops are interconnected horizontally, that is, horizontal rows of loops are interconnected, the knitted structure is called a weft knit. On the other hand, when loops are interconnected vertically, that is, vertical columns of loops are interconnected, the knitted structure is called a warp knit [47]. Several studies have developed strain sensors using the knitting technique. For example, in the

study by Xie *et al.* [48], a weft knitted strain sensor was created using a combination of silver plated multifilament yarns and stainless steel staple yarns. Similarly, in the study by Li *et al.* [49], a weft knitted sensor was created using a blend of silver plated yarns and nylon-spandex yarns. The performance of this sensor was assessed by stretching and bending the sensor. Finally, in [50], different weft knitted sensors were created using different knitting parameters. The results of this study were the creation of sensors with relatively low drift, however, with the drawback of a reduction on the working range over time.

As for stitching, this is by far the simplest method used to fabricate textile strain sensors. Stitching is the process of interlacing two types of threads located inside a sewing machine: a bobbin (or bottom) thread and an upper thread. Depending on the type of sewing machine used, different stitches can be created, with the simplest one being the zigzag stitch. Stitched sensors have the innate characteristic of being easy to manufacture, which makes them attractive for many researchers looking into the development of textile strain sensors. Some studies that have successfully implemented stitched-based sensors include those developed by Tangsirinaruenart and Stylios [51], Dupler and Dunne [52], Martinez *et al.* [53], Park *et al.* [54], among others.

2.5 Textile Sensors Modes of Operation

Regarding their mode of operation, textile strain sensors can be divided into three different categories: resistive, capacitive, and inductive strain sensors. These categories are described below.

2.5.1 Resistive Textile Strain Sensors

Resistive strain sensors work by sensing the variations in the resistance of the material when it is being stretched, and their characteristics have been deeply studied in recent years. For example, in [37], a resistive strain sensor was fabricated by coating a knitted structure with conductive polymer, such as PEDOT to enhance its sensing capabilities. In [55], a flexible strain sensor was created by weaving conductive threads using a plain and a twill weave. Another example of a resistive strain sensor can be found in the study performed by Lin *et al.* [56], in which they implemented a new type of manufacturing process of a strain sensor coated with conductive

polymers.

2.5.2 Capacitive Textile Strain Sensors

On the other hand, capacitive strain sensors work by measuring the changes in the capacitance of two conductive materials separated by a dielectric material. Multiple studies have implemented this sensing modality in strain sensors, as capacitive strain sensors show a more stable performance when compared to resistive strain sensors. For example, in [57] multiple capacitive strain sensors were integrated onto a garment to track shoulder kinematics. Similarly, a capacitive strain sensor was implemented in [58] to measure ankle movements of subjects using the sensor.

2.5.3 Inductive Textile Strain Sensor

Finally, inductive strain sensors have been studied more recently. This type of sensors uses the inductance properties of conductive materials to sense changes in electromagnetic fields. Several examples of inductive strain sensors exist in the literature, such as in a study performed by Wu *et al.* [59], in which they presented the procedure for developing a highly sensitive inductive strain sensor. In a related study [60], an inductive strain sensor based on the coupling of two coils embroidered onto a fabric was used to monitor the breathing activity of several subjects. Finally, in [61], an inductive strain sensor was implemented to monitor the bending angle of the back of subjects wearing a garment with the sensor embedded onto it.

2.6 Textile Strain Sensors Sensing Mechanisms

Regardless of the mode of operation, textile strain sensors need to undergo through some physical changes in order to generate changes on its resistance, capacitance, or inductance. These physical changes will control the sensing response of the textile sensor. Among these physical changes, crack propagation across the sensor and mechanical deformations are two factors that play a major role in the electrical behaviour of the sensors.

2.6.1 Crack Propagation

As the name implies crack propagation is the formation of microcracks on the coating layer of the yarns whenever they are subjected to stretching forces. These yarns can vary in length, width, and depth, and are strain dependent. This means that the more the yarn is stretched, the higher the number of cracks that will appear on the surface of the conductive yarn. Typically, crack-based textile strain sensors will show an increase in their base resistance, as the cracks on the conductive layer will form a network of resistances in series and parallel. This was shown by Wang *et al.* [39], who studied the strain sensing behaviour of PPy-coated lycra yarns. They found that the sensitivity of the PPy-coated yarns is not only a function of strain, but also a function of the length, width, and number of cracks across the conductive thread. Crack-based textile sensors have also been developed in other studies, such as in the one performed by Ko *et al.* [40]. In their study cracks were formed on a fabric that was dip coated on a solution containing SWCNTs. In a similar study [62], changes in resistance of a coaxial fibre made of SWCNTs were measured after the formation of cracks across the SWCNTs core. These studies demonstrate that crack formations are an easy and consistent way to control the sensing response of textile strain sensors. However, as mentioned before, it is important to not go past the strain limits used to create the cracks, as increasing the amount of strain applied to the sensor could cause inconsistent readings due to the appearance of more cracks.

2.6.2 Mechanical Deformation

With respect to mechanical deformations, textile strain sensors experience a change in their electrical response whenever the conductive yarns show signs of deformation. A classic example of this behaviour is observed in the sensors presented by Atalay *et al.* [63]. In their study, whenever the sensors stretched, they showed a reduction in their cross-sectional area, which caused a change in the capacitance of the sensors. In another study [64], where different geometrical shapes were tested on fabric coated with SWCNTs, the resistance of the sensors increased due to changes in their geometrical shape as they were being stretched. This behaviour was similar to the one shown by the sensors used in [65]. In that study, a series of cuts were performed on a woven fabric that

was coated with a silver ink using ink jet printing. When the fabric was subjected to stretching forces, the cuts on the fabric caused an out-of-plane deformation that decreased the contact points between the yarns of the woven structure. This resulted in an increase of the overall resistance of the woven structure. On a similar note, mechanical deformation is also observed in knitted and stitched textile strain sensors. In the case of knitted sensors, the resistance change is due to a deformation of the knitted loops. On the other hand, the change in the electrical response of stitched sensors is given by the deformation of the stitches whenever axial forces are applied to the fabric. Although achieving mechanical deformation on the sensors is relatively simple, the constant changes in the mechanical characteristics of the sensor can cause the sensors to break or perform poorly.

2.7 Concluding Remarks

This chapter provided a brief overview of different soft wearable mechatronic devices and their applications in upper-limb robot-assisted therapy. Furthermore, the need for soft sensing mechanisms within these wearable mechatronic systems that are able to track user motions and detect interaction forces was identified. Also, in Section 2.4, textile strain sensors were introduced as a type of motion and force sensors that could be used in soft wearable mechatronic devices. Finally, the rest of this chapter focused on some of the different methods of fabrication, modes of operation, and sensing mechanisms of textile strain sensors. In the following chapters, the design and characterization of a novel textile strain sensor fabricated using an embroidery technique will be discussed. Furthermore, the application of this type of sensor as a motion sensor and as a force sensor will be presented.

Chapter 3

Design and Fabrication of Embroidered Textile Strain Sensors: An Alternative to Stitch-Based Strain Sensors

This chapter is adapted from “Design and Fabrication of Embroidered Textile Strain Sensors: An Alternative to Stitch-Based Strain Sensors,” published in MDPI Sensors, 2023 [66].

3.1 Introduction

Continuous monitoring of human motion has been shifting towards the use of smart textile sensors. This is especially important in the context of musculoskeletal rehabilitation, as textile strain sensors have the advantage of being able to be seamlessly integrated directly onto every-day garments, thus allowing for a continuous tracking of joint motions outside of a lab-constrained environment. Furthermore, when used alongside soft actuators, such as twisted coiled actuators [67], it would be possible to create a soft wearable mechatronic device that could be used during robot-assistive therapies. This would be possible because textile strain sensors are capable of reducing the overall bulkiness of the wearable robotic device by removing the need for bigger enclosures and reducing

the number of wires required for communication with the mechatronic device.

The working principle of these sensors is based on measuring the change in the electrical parameters (*e.g.*, resistance, capacitance, or inductance) of the material when it is being stretched. Based on this principle, different techniques for fabricating textile strain sensors have been proposed in the last couple of years. For example, several studies have successfully created resistive strain sensors by coating weaved or knitted textile structures with either a conductive polymer, such as the poly(3,4-ethylenedioxythiophene) (PEDOT) [37, 56], graphene particles [68], or carbon nanotubes (CNT) [69], to enhance its sensing capabilities. Other studies [63, 64, 70] have implemented a method that consists of modifying the physical properties of a conductive fabric by laser cutting different patterns on it, and then enclosing the cut fabric inside a silicone material to create an elastic structure. On the other hand, printing techniques have also been adopted to create textile strain sensors by printing gage patterns directly onto the fabric [71, 72]. Although textile strain sensors created using these methods demonstrate promising results, they can suffer from low durability due to the formation of microcracks produced after repeated strain cycles [73]. Furthermore, some of these sensors have low biocompatibility, as in the case of sensors made out of CNT, which sometimes can cause irritations when in contact with the skin for prolonged periods of time [44].

Stitching and embroidering, on the other hand, are two alternative methods used in the fabrication of textile strain sensors. Stitching can be created using three different techniques: interlooping, intralooping, and interlacing [74]. Each of these three categories can produce different classes of stitches, with the lockstitch being the most common on many commercial embroidery machines. The lockstitch stitch can be created by interlacing two threads—an upper thread and a bobbin thread—located inside an embroidery machine. An example of a lockstitch type of stitch is the zigzag stitch, as shown in Figure 3.1a, which is the most used in the fabrication of textile strain sensors. On the other hand, embroidering happens when multiple stitches are combined to form a specific pattern (Figure 3.1b). The main advantages of these two methods are that they do not require a change in the physical properties of the textile structure; instead, they use conductive threads that are directly attached to the fabric. Furthermore, the ease on the manufacturability of stitched and embroidered structures allows for a mass production of textile sensors without

compromising their cost and reproducibility [75].



Figure 3.1: Stitching and embroidery examples. **(a)** A zigzag stitch formed by the interlock of a bobbin and needle thread. **(b)** An embroidery pattern formed by the combination of multiple stitches.

Although stitching and embroidering can be used to build textile strain sensors, stitching has been regarded as the preferred method of fabrication. This is because the disadvantage of embroidering is that it creates rigid structures that are not stretchable, independent of the fabric substrate onto which they are attached. Another advantage that stitching has over embroidery is that, in its relaxed state, most stitches have multiple contact points that reduce the resistance of the conductive thread used to make them. Whenever the stitches are stretched, the number of contact points between stitches decreases, which causes an increase in the resistance of the conductive thread. Several studies have taken advantage of this behaviour with good results. For example, in the study by Tangsirinaruenart and Stylios [51], different stitches were tested to create a textile resistive strain sensor. They found that the one that demonstrated the best characteristics was the zigzag stitch made out of a silver-plated conductive thread. Similarly, Park and Lee [54] studied the effect that different stitch parameters, such as stitch length, stitch shape, and stitch size, had on the performance of the strain sensor. Another study, in which a stitched sensor was implemented, was the one performed by Martínez Estrada *et al.* [53]. In this study, two zigzag stitches with different shapes and dimensions were overlapped on top of each other to increase the number of contact points of the conductive thread. Other studies, such as the one by Dupler and Dune [52], demonstrated that specialty stitches are more suitable for strain applications.

Even when stitching presents a reliable solution for fabricating textile strain sensors, it has several inconveniences. One is that some specialty stitches require the use of technical embroidery machines that can create stitches using any of the three methods of fabrication. The other issue is

that almost all stitches have different shapes on each side of the fabric, and those who do not, need to have specific parameters adjusted to maintain a consistent shape on each side. For example, a zigzag stitch will have its characteristically triangular shape on the upper side of the fabric, whereas underneath the fabric, it will look like a group of perpendicularly spaced lines if the stitch is too small (Figure 3.2).

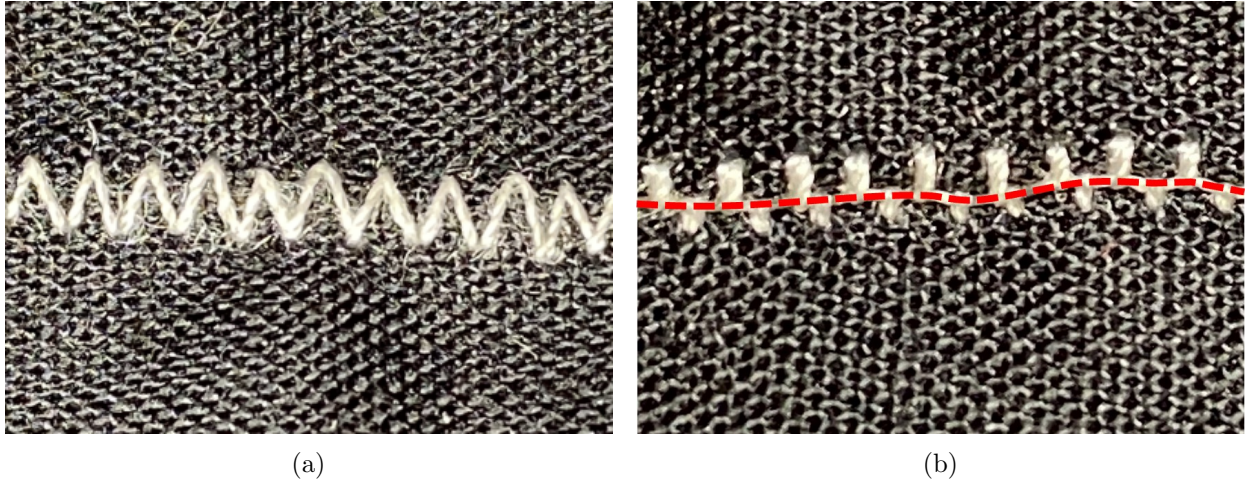


Figure 3.2: (a) A zigzag stitch is observed on the upper side of the fabric. (b) The same zigzag stitch as observed on the bottom side of the fabric. The dashed red line shows the bobbin thread.

This means that in almost all cases, the conductive thread should be used as the top fabric thread (the needle thread), so that there exist contact points within the stitch itself. This, however, is not always possible, as many commercial embroidery machines are not built to handle specialized threads such as metallic fibres. Unlike regular threads, conductive threads suffer from breaking and fraying due to the high friction produced as the thread goes through the many thread guides inside the machine. This issue can severely affect the performance of the strain sensor by creating discontinuous conductive paths, which result in a poor sensing ability. On the other hand, every time the conductive thread penetrates the substrate fabric, there is a chance that small fibres within the conductive thread could break and fall on the surface of the fabric. These small fibres will create conductive paths that can affect the overall performance of the strain sensor. Another problem of using the conductive thread as the top thread is that in some cases, the conductive thread can jam the embroidery machine, as this thread is thicker than regular threads. This is a

major issue, as it hinders the ability of the machine to mass produce the sensors.

These problems can be avoided by using the conductive thread as the bobbin thread (on the bottom of the fabric). Moreover, by using regular embroidery machines to embroider sensors, the need for specialty stitches, that can only be made using highly specialized machines, would be avoided. However, as mentioned before, the major challenge that needs to be addressed with embroidering is creating a structure that can be stretchable, without compromising the integrity of the conductive thread. Therefore, in this study a method for building resistive textile strain sensors is presented. The main contribution of this paper is the development of a sensor fabricated using a stretchable embroidered structure, created using a commercial non-technical embroidery machine, and that shows good sensing performance. The remainder of this paper is divided as follows: Section 3.2 presents the methods of this study, including the design guidelines for the embroidered textile strain sensor, the data collection, and data analysis. Section 3.3 describes the performance metrics used to assess the sensors. Section 3.4 and Section 3.5 demonstrate the results and discussion, respectively. Finally, in Section 3.6, the conclusion of this study is summarized and some recommendations for future work are given.

3.2 Fabrication of Embroidered Textile Strain Sensors

Before embroidering, it is necessary to decide on the principle of operation of the textile strain sensor. As mentioned before, these sensors can work by measuring the changes in resistance, capacitance, or inductance produced when the sensor is stretched. In this study, it was decided that resistive sensors were the better option, as capacitance-based strain sensors can be susceptible to electromagnetic interference from anything that is conductive, such as the human body; inductive-based sensors can also be affected by other sources of noise due to their design, which resembles that of an antenna. Therefore, the proposed fabrication method for the embroidered resistive textile sensor is shown in Figure 3.3 and is summarized below.

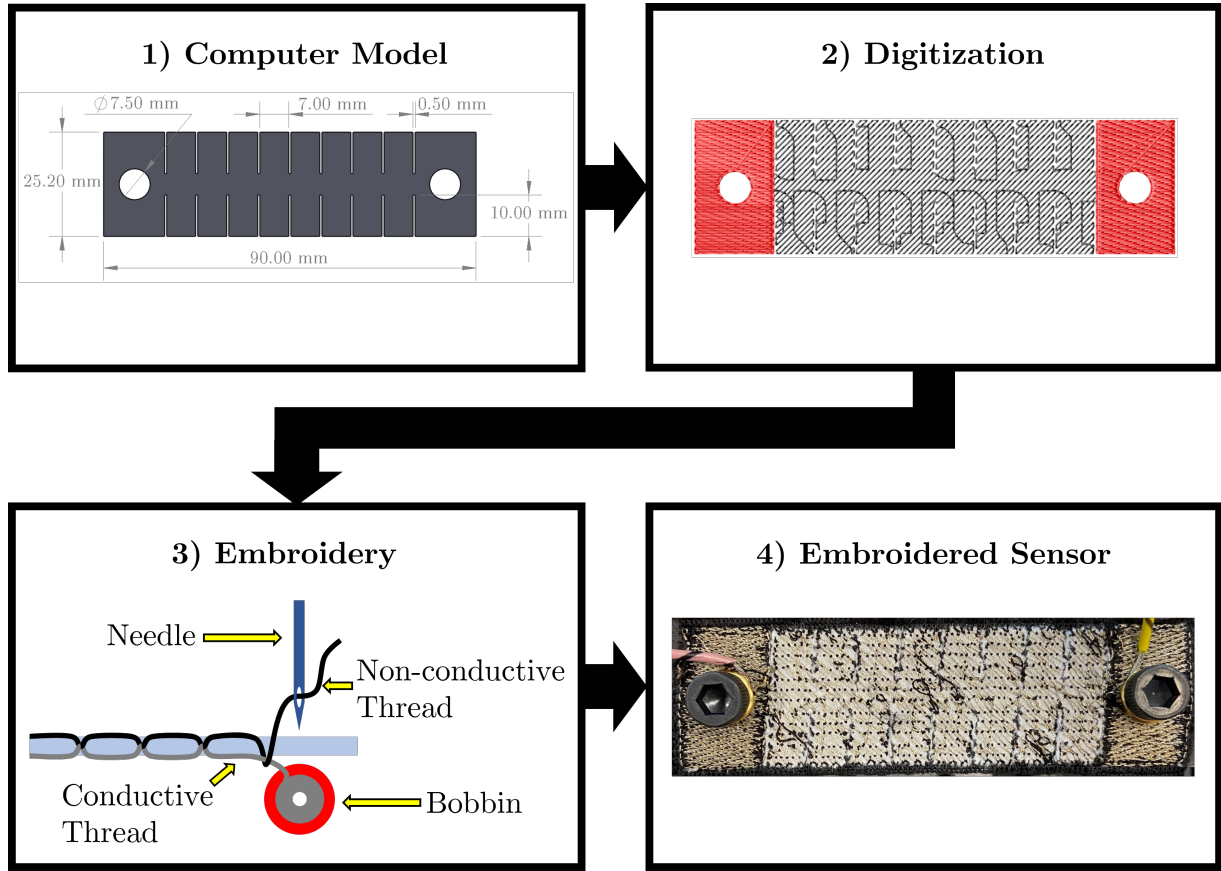


Figure 3.3: Design process of the embroidered textile strain sensor. First, a CAD model of the sensor is created. Then, the CAD model is digitized to produce an embroidery compatible file that will be read by an embroidery machine. Finally, the sensor is embroidered based on a set of specifications defined during the digitization phase.

3.2.1 Computer-Aided Design (CAD) Model

The first step taken in the fabrication of the embroidered textile strain sensor was to create a model of the sensor using a CAD software. The use of a CAD software is important, as it allows the sensor to be drawn with precise dimensions. One important aspect to consider during the sensor design phase is that the sensor will change its dimensions when going through the embroidery step. Depending on the embroidery setup parameters, such as the type of embroidery stitch used, the sensor length or the sensor width will be reduced depending on the stitch direction. Therefore, care should be taken when designing the sensor, as the change of dimensions can affect the sensor behaviour. This issue can be minimized by using a CAD software, as the reduction on size can be estimated and an offset can be added as part of the design.

3.2.2 Digitization

After the CAD model of the sensor is designed, it needs to be exported as a vector file, such as a drawing exchange format (DXF) file, in order to be converted into a digitized stitching pattern, which will indicate the needle paths for the embroidery machine. During the digitization step, it is important to set the appropriate parameters that will change the mechanical behaviour of the embroidered textile strain sensor. The following are the most important parameters that need to be adjusted:

- **Stitch type:** Embroidering machines are capable of creating three major types of stitches, the stroke stitch, the fill stitch, and the satin stitch. Stroke stitches can be made of running stitches and zigzag stitches and are very useful for creating lines and outlines. On the other hand, as their name implies, fill stitches are used to fill closed areas. It is important to know that fill stitches are made of multiple running stitches bundled together. Finally, satin stitches are a variation of fill stitches and are mostly used to fill small areas.
- **Stitch length:** This parameter refers to the length of each stitch. A small value will increase the total thread count of the design. For the zigzag stitch, the stitch length controls its width.
- **Stitch direction:** This option controls the direction of the stitch pattern. If the type of thread used for embroidering is not stretchable, it is important to avoid 0° angles, as they will create a rigid conductive path that will break upon stretching.
- **Row spacing:** The density of the design is controlled by the row spacing. This density will affect the electrical behaviour of the sensor, *i.e.*, the higher the density, the higher the current that will flow through the sensor [76, 77]. A high density is not always desired in resistive strain sensors, as reducing the space between stitch rows may create unwanted short circuits between the conductive thread.
- **Underlay:** Enabling the underlay option will generate a series of running stitches that will secure the fabric substrate used during the embroidery process to a stabilizer substrate. Furthermore, the underlay will also prevent any distortion of the design produced by stitches pulling the fabric during the embroidery step.

- **Underpath:** This optional parameter will modify the travelling path of the stitch when moving between sections. Turning the underpath off will make the stitches run on the outline of the embroidery design. For strain sensors, enabling the underpath is preferable, as stitching around the outline of the design will prevent the embroidered structure from stretching.

3.2.3 Embroidery

After digitizing the embroidery design, the next step consists of using an embroidery machine to create the physical strain sensor. However, before embroidering, it is necessary to select the appropriate materials that will form the sensor.

3.2.3.1 Fabric Substrate

The first material that needs to be considered is the fabric substrate that will be used to attach the embroidered design. This fabric should be made out of a textile structure that allows a certain degree of stretchability without losing its original shape, i.e., the fabric should not deform after being stretched. Furthermore, if the fabric substrate presents a degree of hysteresis after being stretched, the textile strain sensor will also show this nonlinear behaviour [51]. Generally, fabrics can be made by weaving or knitting multiple yarns together. A weaved fabric is constructed by interlacing yarns that are perpendicular to each other (Figure 3.4a), whereas a knitted fabric is made by looping together consecutive rows of yarns (Figure 3.4b).

While both weaving and knitting can be used as the main textile structure for the fabric substrate [78], knitted structures are preferred, given their stretchable capabilities. The amount of stretchability also depends on the type of fibres used to create the textile structure. Ideally, the fabric substrate should be made of a blend of fibres that have enough elasticity so that they can regain their original shape after being stretched. Some examples include fabrics made of polyester/span-dex materials [64], polyamide fabrics combined with elastomers (Shieldex Medtex-130, V Technical Textiles Inc., Palmyra, NY, USA), polyester/elastodiene [53], and nylon/spandex [51], among others.

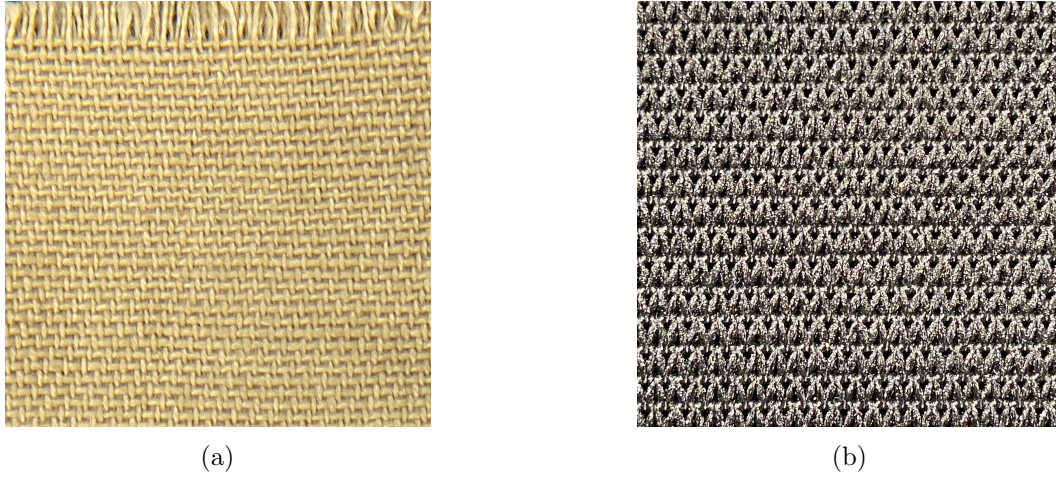


Figure 3.4: Examples of textile structures. (a) A close up view of a weaved structure. (b) A close up view of a knitted structure.

3.2.3.2 Conductive Thread

The second material that needs to be selected before embroidering the textile strain sensor should be the type of conductive thread. Different types of conductive yarns exist, but the most common ones found in the development of strain sensors are metallic threads (*e.g.*, 100% stainless steel threads), synthetic yarns coated with a fine metal layer (*e.g.*, silver plated conductive thread), or a blended combination of metal fibres with synthetic yarn. Out of these three types of conductive threads, blended yarns are not recommended to create textile strain sensors, as the way in which the fibres within the blended yarn are arranged during its fabrication can change significantly its conductive behaviour, which can greatly affect the change in the electrical characteristics of the resulting sensor [47]. Similarly, bare metallic threads can represent a challenge, given that some of their properties may be incompatible with fabric substrates [79]. For example, dense conductive threads, such as stainless steel threads, can create a rigid structure that may not be stretchable. Instead, it is preferable to select 100% metallic threads made of very fine filaments (with diameters in the order of μm) twisted together. On the other hand, care should be taken when working with metal-coated yarns as the friction and tensile forces produced while embroidering can damage the conductive layer on the thread. This can create discontinuities in the electrical path, which can render the sensor unusable.

3.2.3.3 Stabilizer Substrate and Embroidery Needle

Finally, the last two elements that should be taken in consideration before embroidering are the stabilizer substrate and the type of embroidering needle used. Stabilizers are another type of non-stretchable fabric that is used alongside the fabric substrate. For every embroidery design, it is important to use a stabilizer, as it will prevent the fabric substrate from moving when it is being embroidered. There are three types of stabilizer substrates: the tear-away, the cut-away, and the water-soluble stabilizer. Cut-away stabilizers are not recommended for strain applications, as they are mostly used to create fixed and rigid structures. On the contrary, tear-away and water-soluble stabilizers can be removed after the embroidery process is finished, with the water soluble stabilizer being the one that can be completely removed.

Regarding the embroidery needle, it is important that it is suitable for the type of thread and the type of fabric substrate used. Embroidering needles fall in two categories, ballpoint needles and cutting needles. Ballpoint needles are the preferred type when using stretchy fabrics, as their rounded tip can pierce the fabric without damaging its fibres. Cutting needles should be avoided, as they pierce the fabric by cutting its fibres. This can lead to the fabric substrate losing its stretching capabilities, and in more severe cases, create microcracks that can rip the fabric after a certain number of stretching cycles.

Another important aspect when choosing the type of needle is to select the appropriate needle size. Needle sizes are given by two numbers in the form of $Nm/S\#$, where Nm is a metric number that represents the diameter of the needle blade in hundredths of a millimetre, and $S\#$ is a standard number that represents the size of the needle in the Singer (American) system. For example, a 70/10 needle indicates a needle that has a diameter of 0.7 mm, which corresponds to a number 10 needle in the Singer system. Smaller needles can damage the upper thread if the thread used is too thick, causing thread breakages. Moreover, the needle can bend, causing issues during the interlacing of the bobbing and the needle thread, which can lead to needle breakages [80].

3.2.4 Embroidered Textile Strain Sensor

After conducting some preliminary tests, the embroidered textile strain sensor was fabricated using a Janome Memorycraft 15000 automated embroidery machine that embroidered a Bekinox VN14/1x90/100Z stainless steel conductive thread (Bekaert, Zwevegem, Belgium) onto a 64%/36% polyester–rubber elastic knit structure. This knit structure was a commercially available elastic band, and its fibre composition was specified by the manufacturer. The sensor was designed in SolidWorks 2021 (Dassault Systèmes, SolidWorks Corporation, Waltham, Massachusetts, USA) using a rectangular shape, as shown in Figure 3.3. A series of 10 by 0.5 mm cuts were added to the rectangular shape so that the sensor could be stretched after being embroidered. Furthermore, two holes of 7.5 mm of diameter were added to each end of the design, so that they could be used to attach wires to the sensor using grommets.

The resulting CAD model was further digitized using an open source scalable vector graphics editor named Inkscape with the Inkstitch extension. During digitization, a 3 mm running stitch at a 45° angle with an underpath was selected to form the sensor, as shown in Figure 3.5.

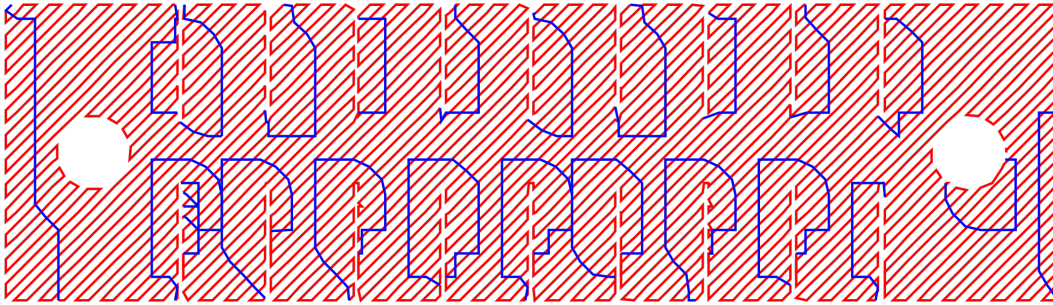


Figure 3.5: Digital representation of the embroidered textile strain sensor. The red lines represent the running stitch direction and the blue lines show the underpath that will be followed by the needle when embroidering. Changes in resistance happen when the running stitch contacts the underpath.

The underpath was added because it allowed the sensor to be stretched by preventing the running stitches to run through the outline of the sensor. The second reason was to create more conductive paths when the running stitch and the underpath touched each other. Given that the Bekinox VN14/1x90/100Z stainless steel thread is made out of 90 strands of stainless steel filaments of 14 μm twisted together, the total number of strands that are in contact with the underpath

changes under the applied strain. When stretched, the cross-sectional area of the conductive thread decreases, which increases the total number of contact points between the fibres that form it, therefore reducing its total resistance [81]. Furthermore, a fill stitch was used to cover each end of the strain sensor in order to attach wires for data collection. This fill stitch also prevented the sensor from being damaged after repeated cycles of stretching and unstretching.

As mentioned before, the sensor was embroidered onto a polyester–rubber elastic knit fabric substrate. This type of fabric was selected as the stretchability of the knit structure combined with the rubber properties of the material, made for an elastic substrate that would regain its original shape after being stretched. Furthermore, the elastic fabric substrate was slightly stretched when placing it on the embroidery hoop; and a double layer of a tear-away stabilizer was used, as it was noted that a single layer caused irregularities in the stitches during the embroidery process. Finally, the sensor was embroidered at 400 stitches per minute (spm), which is the lowest speed that the embroidery machine used could achieve. The reason for using a low speed is to reduce the damage caused to the conductive thread during the embroidery process [82]. The completed sensor can be observed in Figure 3.6.



Figure 3.6: The embroidered textile strain sensor with dimensions of 90 by 25 mm. Wires are attached to each end of the sensor using grommets.

3.3 Performance Evaluation Metrics

In order to assess the performance of the embroidered textile strain sensor, several properties of the sensor response were measured. Some of these properties are depicted in Figure 3.7, and are

defined as follows [47, 51]:

- **Working range:** The working range is defined as the range over which the resistance changes within the range of the strain that follows a non-constant and monotonic function, *i.e.*, the resistance increases or decreases its value as the strain changes in one direction. A sensor that increases its resistance proportionally to an increase in strain is called monotonically increasing, whereas one that decreases its resistance proportionally to an increase in strain is called monotonically decreasing.
- **Linearity:** The proportion of change in the sensor resistance with respect to the proportion of change in strain defines its linearity. The linearity of a sensor is given by the R^2 , with a sensor having an R^2 equal to one being perfectly linear.
- **Sensitivity:** The sensitivity of a resistive strain sensor indicates the change in resistance (ΔR) with respect to an applied strain. This property is represented by the gauge factor GF and is given by the following equation:

$$GF = \frac{\Delta R/R_0}{\varepsilon}, \quad (3.1)$$

where ε represents the strain, which indicates a change in the sensor overall length (ΔL) under stretching conditions, and R_0 indicates the initial resistance of the sensor before stretching. The strain can be calculated as follows:

$$\varepsilon = \frac{\Delta L}{L_0}, \quad (3.2)$$

with L_0 indicating the sensor initial length.

- **Hysteresis:** This property refers to the difference of the sensor resistance change during an increasing and decreasing strain on any given stretching cycle. The sensor hysteresis H_ε can be measured by finding the maximum strain difference ($\Delta\varepsilon_h$) between the loading and unloading cycle for a specific measured resistance value, and normalizing it with respect to

the difference of the maximum (ε_{max}) and minimum (ε_{min}) applied strain, as follows [47]:

$$H_{\varepsilon} = \frac{\Delta\varepsilon_h}{\varepsilon_{max} - \varepsilon_{min}}. \quad (3.3)$$

- **Repeatability:** The repeatability indicates the ability of the sensor to keep its original electrical response over a certain number of cycles. When a sensor performance changes, it is said that the sensor drifts (Figure 3.7). Repeatability is an important parameter, as it indicates whether a sensor is reliable or not.
- **Reproducibility:** Differently from repeatability, reproducibility indicates the ability of the sensor to show the same electrical response on different sensor samples. This metric is very important, as it highlights one of the advantages of embroidery, which is the mass sensor production capabilities.

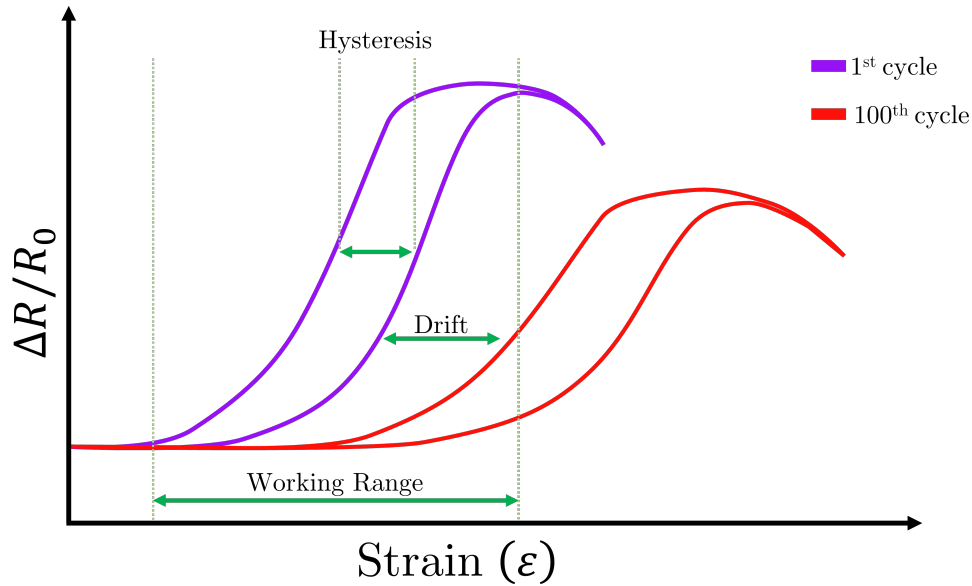


Figure 3.7: Typical response of a strain sensor when stretched. Here, several properties are shown, including hysteresis, sensor drift, and working range. Note that no scale is provided for the x and y axis, as no real data were used in this example.

3.3.1 Experimental Setup

After defining the performance metrics of the embroidered textile strain sensor, three sensor samples were created and left idled at the Wearable Biomechanics Laboratory for one week, to condition them to the ambient temperature and relative humidity. Then, each sensor sample was tested at an ambient temperature between 22.5 and 23 °C. Data were collected using a DM3058E digital multimeter (RIGOL Technologies Inc., Portland, OR, USA). To reduce any measurement errors due to the resistance of the test probes and the sensor wires, the digital multimeter was configured to perform a 4-wire resistance, as the initial resistance of each sensor was around 26 Ω . Finally, the sampling frequency of the multimeter was set to 2.5 Hz to achieve a resolution of 0.001 Ω . This resolution was chosen because preliminary testing demonstrated that the change in the resistance of the sensors was around 15 Ω .

During the experiments, the sensors were clamped onto a moving mechanism that consisted of a lead screw attached to a motor, whose speed and position were controlled using an EPOS2 24/2 motor driver (Figure 3.8).

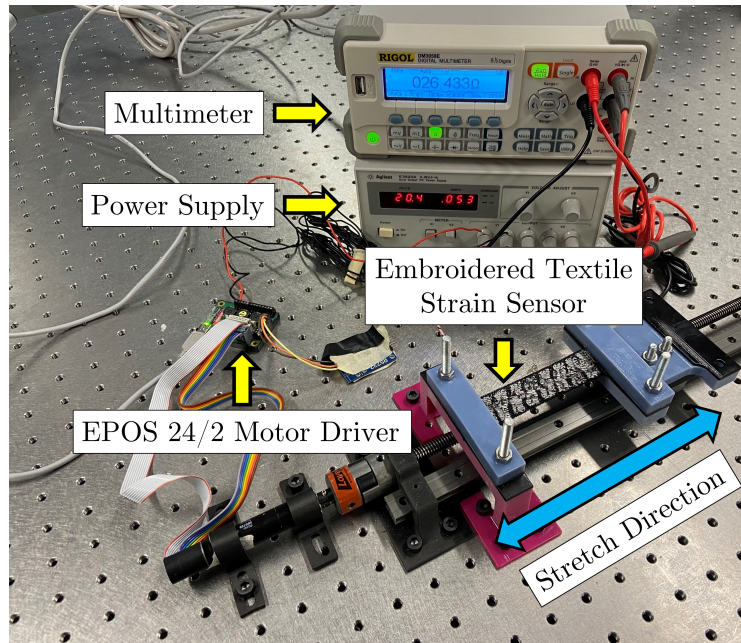


Figure 3.8: Testing setup used for collecting data from the embroidered textile strain sensors.

Each of the three sensors were subjected to a 66% strain at a constant speed of 69 mm/min

during 100 cycles. The number of cycles was selected so that the performance of the sensors could be compared to the results obtained by Tangsirinaruenart and Stylios [51], who used the same number of stretching cycles. The speed was set to obtain as many resistance samples as possible from the multimeter, as the low change in resistance from the sensors made it difficult to obtain enough data as needed, for the further evaluation of the properties discussed in the previous section. With this speed, it was possible to obtain 218 resistance samples during each cycle, which were enough for data analysis. Finally, data from the motor driver and the digital multimeter were sent to a computer that matched the position and resistance data using a custom program written in Python [83].

3.4 Results

After testing the embroidered textile strain sensors, the collected data were post-processed and analyzed offline using MATLAB R2021a (MathWorks, Inc., Natick, Massachusetts, USA). For each of the three sensor samples, the resistance data of each stretching cycle were smoothed using a 3rd order Savitzky-Golay filter with a window length of size 13. The Savitsky-Golay filter was used over other traditional smoothing methods, such as the window moving average, as it does not tend to distort the data or reduce its signal intensity [84]. The metrics discussed in Section 3.3 were extracted from each sensor sample.

3.4.1 Working Range

The first performance metric extracted was the working range. Figures 3.9–3.11 show the plots of the change in resistance due to the strain for Sensors S1, S2, and S3, respectively, during the 1st, 11th, 40th, and 100th stretching cycle. As can be observed, the working range from each sensor decreases with each stretch cycle. For example, from Figure 3.9, it can be observed that Sensor S1 had an initial 7.5–66% working range. However, this working range started to decrease rapidly until the 10th cycle, when a smaller reduction on the working range was observed before stabilizing to a 40–66% range on the 40th. Although all of the three sensor samples stabilized to the same working range, Sensor S1 and S3 were the only ones that started with a working range

between 7.5% and 10% of strain to a maximum of 66% of strain. On the other hand, Sensor S2 had an initial 22–66% working range (Figure 3.10).

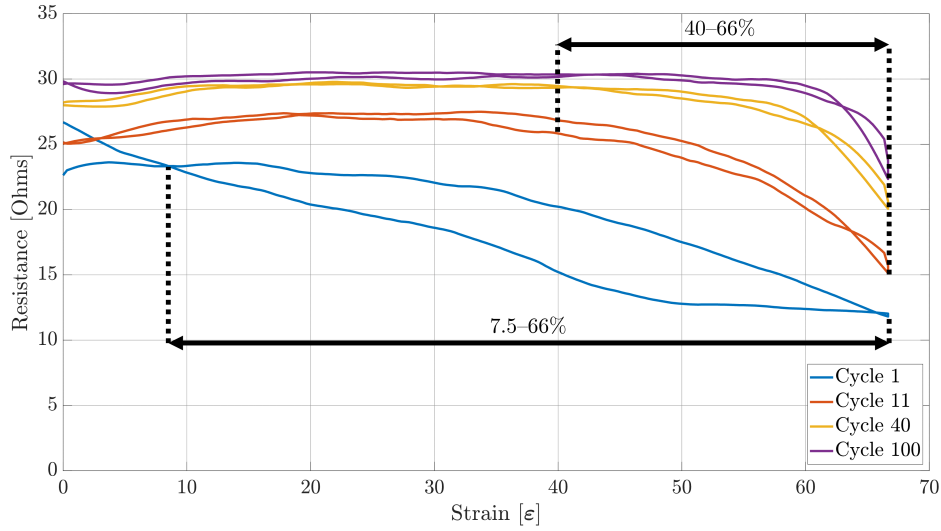


Figure 3.9: Sensor S1 strain data over the 1st, 11th, 40th, and 100th stretching cycle.

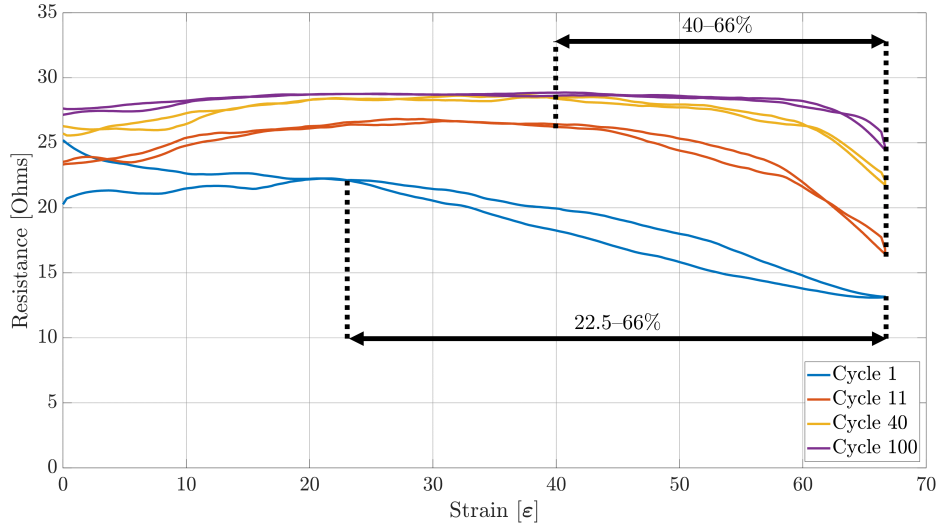


Figure 3.10: Sensor S2 strain data over the 1st, 11th, 40th, and 100th stretching cycle.

Another important aspect that can be noted is that each of the three sensor samples present a decreasing monotonic behaviour during the 1st stretching cycle. However, as the stretching cycles increase, each sensor starts presenting an increasing monotonic behaviour over the range of 0–20% strain, with Sensors S2 and S3 being the ones that show a steeper increase. On the other hand,

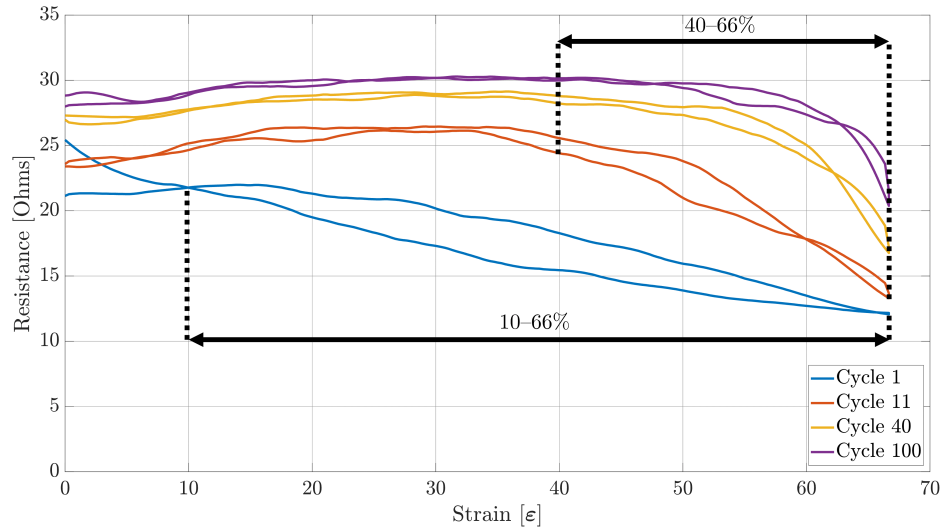


Figure 3.11: Sensor S3 strain data over the 1st, 11th, 40th, and 100th stretching cycle.

each of the three sensor samples present a non-monotonic behaviour on the range of 20–40% of strain, ending with a decreasing monotonic behaviour on the range of 40–66% of strain produced by a decrease in the resistance as the strain increases.

3.4.2 Linearity

Having found the working range of each sensor sample, the next performance metric obtained was the sensor linearity. This parameter was obtained for each of the 100 stretching cycles across the three sensor samples. For each cycle, the linearity was obtained only for its specific working range. That is, a line of best fit was applied to a working range between 7.5% and 66% for the first 10 stretching cycles on each sensor sample; and for the remaining 90 cycles, a line was fitted to the data over the 40–66% working range for all of the three sensor samples. An example of these linear fits can be observed in Figures 3.12–3.14.

From these figures, it can be observed that, for the particular case of each of the embroidered textile strain sensor, the sensors demonstrated a more linear behaviour during the first stretching cycle. This linear behaviour was consistent during the first 10 cycles for each sensor. However, as the working range of the sensor decreased, so did its linearity. Interestingly, the sensor that showed the highest linearity score during the first stretching cycle was Sensor S2, with an R^2 equal to 0.898, followed by Sensor S3 and S1 with an R^2 of 0.889 and 0.798, respectively. On the other

hand, at the 100th stretching cycle, Sensor S3 had the highest linearity with an R^2 equal to 0.738; and Sensors S1 and S2 had a similar low linearity with an R^2 of 0.629 and 0.646, respectively.

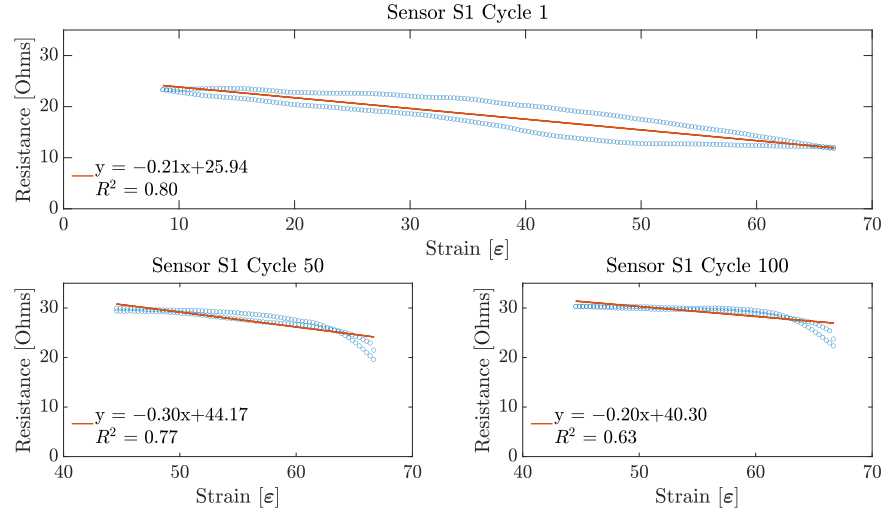


Figure 3.12: Linearity results for Sensor S1. Linearity data from Cycle 1 are shown over a 7.5–66% working range, whereas linearity data from Cycles 50 and 100 are shown over a 40–66% working range.

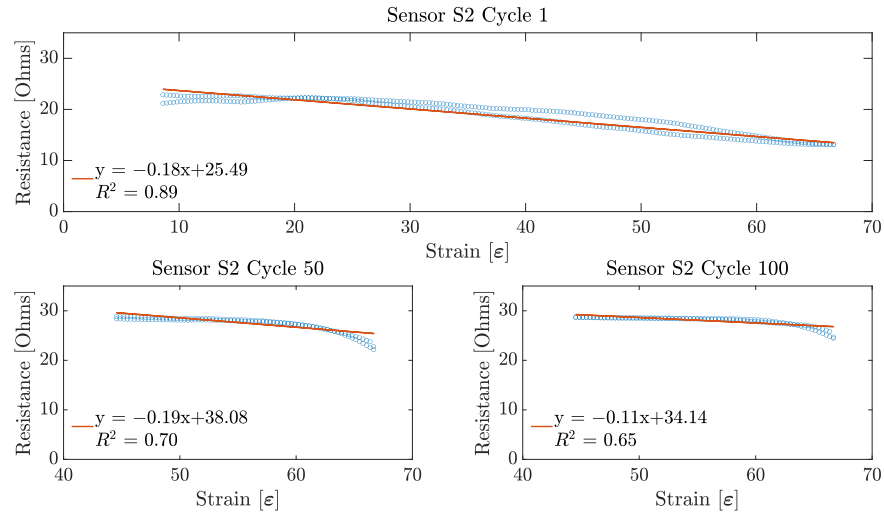


Figure 3.13: Linearity results for Sensor S2. Linearity data from Cycle 1 are shown over a 7.5–66% working range, whereas linearity data from Cycles 50 and 100 are shown over a 40–66% working range.

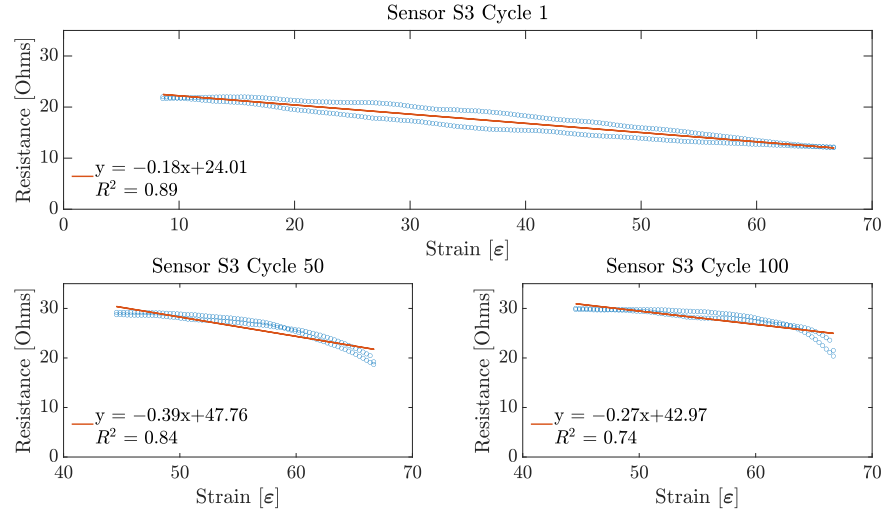


Figure 3.14: Linearity results for Sensor S3. Linearity data from Cycle 1 is shown over a 7.5–66% working range, whereas linearity data from Cycles 50 and 100 are shown over a 40–66% working range.

3.4.3 Sensitivity and Hysteresis

With the sensors' working range and linearity already obtained, the sensitivity and the hysteresis of each sensor during each cycle was measured. Similarly to the linearity performance, both the sensitivity and hysteresis of the sensor were obtained over the appropriate working range. From Figures 3.9–3.11, it can be observed that all of the three sensors demonstrated a large hysteresis during the first stretching cycle. This behaviour varied until the 10th stretching cycle, at which point the hysteresis was around 52.11%, 70.09%, and 52.11% for Sensors S1, S2, and S3, respectively. However, starting from the 11th cycle, the total hysteresis dropped to around 7.84%, 6.46%, and 9.68% for Sensors S1, S2, and S3, respectively. These low values for each sensor remained at a similar level until the last stretching cycle.

Table 3.1 shows the hysteresis performance of all of the three sensor samples alongside their overall gauge factor and their linearity score. It is important to note that the hysteresis value presented in this table is the average value of the first 10 cycles, when the sensors had the highest hysteresis; and the average hysteresis percentage for the last 90 cycles, when the sensors demonstrated the lowest hysteresis score.

Furthermore, from Table 3.1, it can be noted that the sensitivity of the three sensors was around 1.88, as shown by the average gauge factor. Similarly to its hysteresis performance, all of

Table 3.1: Average sensor performance metrics. Each column in the table represents a specific parameter for a sensor sample (rows) averaged across all 100 cycles (except for the hysteresis score) over its specific working range. For reference, the maximum strain applied to each sensor sample was 66%.

Sensor Sample	Linearity (R^2)	Gauge Factor	Hysteresis (%)	
			Cycles 1–10	Cycles 11–100
Sensor S1	0.76 ± 0.07	1.87 ± 0.49	39.61 ± 12.6	9.15 ± 2.77
Sensor S2	0.74 ± 0.09	1.49 ± 0.47	48.15 ± 22.01	7.99 ± 2.79
Sensor S3	0.81 ± 0.06	2.29 ± 0.57	40.44 ± 15.42	8.48 ± 2.42
Average	0.77 ± 0.07	1.88 ± 0.51	42.73 ± 16.68	8.54 ± 2.66

the three sensor samples started with a low gauge factor, which was around 0.93, 0.8, and 0.85 for Sensors S1, S2, and S3, respectively. On the 11th stretching cycle, the gauge factor increased to 2.78, 2.43, and 3.02 for Sensors S1, S2, and S3, respectively. Unfortunately, this increase in sensitivity happened only during a few couple more cycles, as a slow decrease in sensitivity was later observed on all of the three sensors after a certain number of cycles. However, even when the sensors showed an increase and then a decrease in their sensitivity, each of the three sensors ended with an overall gauge factor that was higher in magnitude than its initial sensitivity value, as shown in Table 3.1.

3.4.4 Repeatability

For each sensor sample, data from each stretching cycle were combined to observe the sensor repeatability performance. These data are shown in Figure 3.15, in which each plot represents data from each of the three sensor samples. From this figure, it can be noted that the initial resistance of each sensor on each cycle drifted upwards until it stabilized around the 40th cycle. The exception to this behaviour was during cycle number one, in which all of the three sensors demonstrated an initial mean resistance of $25.681 \pm 0.712 \Omega$, which dropped to an average resistance of $21.463 \pm 1.129 \Omega$ on the second stretching cycle, and continued drifting upward for the rest of the 98 cycles. Similarly, an upward drift was observed for the resistance of the sensor at the maximum strain applied (66%). This drift caused a constant reduction on the working range and the sensitivity of the sensor until the 40th stretching cycle, which is when these two performance

metrics stabilized. Interestingly, both Sensors S1 and S3 had a similar drift for the working range and their sensitivity across all 100 cycles. Sensor S2, on the other hand, showed a similar stabilization for its resistance value at rest with respect to the other two sensor samples. However, Sensor S2 showed a greater reduction on its resistance at the maximum strain applied compared with the other two sensors.

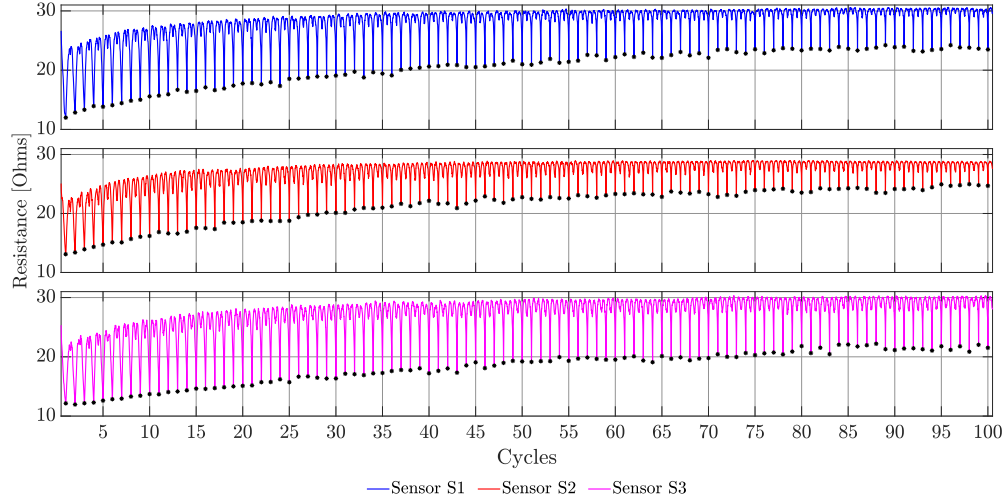


Figure 3.15: Sensor drift over the course of 100 stretching cycles. For each of the three sensor samples, the drift stabilizes around the 40th cycle. The black stars on each plot indicate the maximum strain applied (66%), which was measured halfway through the stretching cycle.

3.4.5 Reproducibility

Finally, the reproducibility of the embroidered textile strain sensor was assessed by finding the similarity between the data on each stretch cycle between all of the three sensor samples. This similarity test was performed using the Dynamic Time Warping (DTW) technique. DTW is a signal processing method used for aligning two time series data by nonlinear mapping the data to a feature space, and then finding the optimal path (known as the warping path) that minimizes the overall cost function that compares each sample of these datasets in a one-on-one fashion [85]. The cost function will measure the distance between two points in the datasets. If the distance is small, *i.e.*, if the two points are similar to each other, the cost function will be small. Furthermore, the similarity of the two datasets compared will be high if the cumulative cost obtained after

comparing each of their data points is small.

Before applying the DTW technique, some data preprocessing was required. First, for each sensor sample, the resistance data collected during all the stretching and unstretching cycles were stored into a single vector to form a time series data. Then, these data were normalized using the Z-normalization, *i.e.*, data from each sensor sample on each cycle had their mean subtracted and then divided by the standard deviation. This was performed because, as explained before, data from each sensor drifted over each cycle, creating a change in the amplitude of the signals that would have impacted the computation of the cost function on the DTW algorithm. Normalizing solves this issue by making the amplitudes of each signal similar to each other [86]. Finally, the DTW algorithm was applied to Cycles 10 to 100 over a 40–66% working range, based on the results found for the previous performance metrics. These results demonstrated that the working range of the sensor was within these limits for the last 90 stretching cycles. Moreover, the cost function used for the DTW was the squared euclidean distance, as it is the most common metric used for computing the distance between sample points in applications involving DTW. The average cost function across the 3 sensor samples for each of the 90 stretching cycles is shown in Figure 3.16.

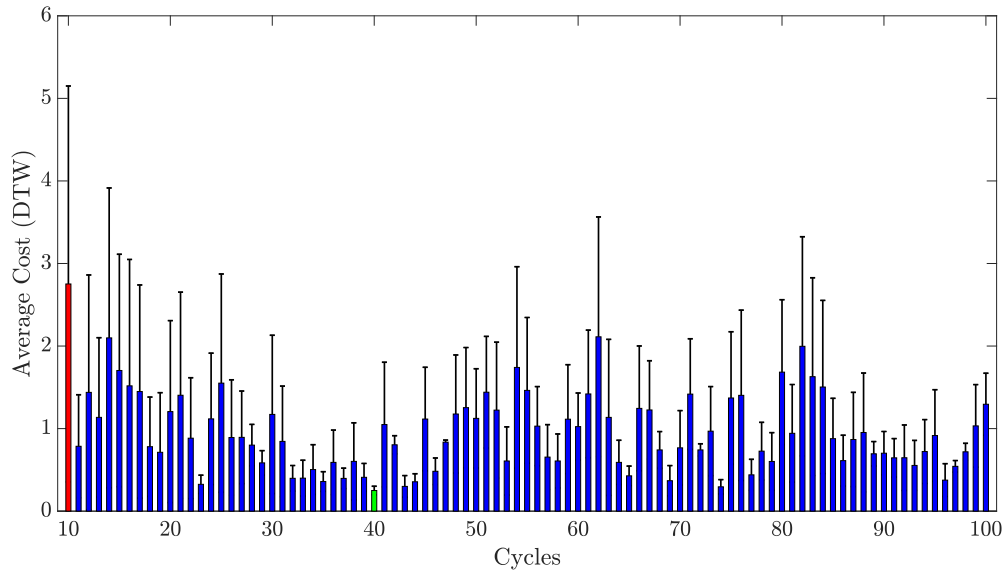


Figure 3.16: Average DTW cost across the three sensor samples for Cycles 10 to 100. The cost function was computed using the squared euclidean distance for each sensor pair combination. The highest average cost function (2.752 ± 2.398) was for the 10th cycle (in red), whereas the lowest average cost function (0.25 ± 0.052) corresponded to the 40th cycle and is shown in green.

Data on Figure 3.16 indicate that each stretch cycle was similar to its homologous cycle on a different sensor sample. With exception of the 10th cycle, the cost for all of the cycles was within the range of 0.25–2.11. Finally, the standard deviation of the average of the cost function for all cycles is also shown in Figure 3.16. It can be observed that similarly to the average cost, the maximum standard deviation was for the 10th cycle. On the other hand, the smallest standard deviation of the cost function happened on the 47th cycle, with a value of 0.025.

3.5 Discussion

Data presented in Table 3.2 show that the embroidered sensors developed in this study have a similar or improved performance in some characteristics when compared to the same characteristics presented in different studies. Note that some of the characteristics were estimated from these studies based on their presented data. To further analyze the performance of the embroidered sensor, a more detailed comparison is discussed in the following sections.

Table 3.2: Performance comparison of stitched sensors and the embroidered sensor presented in this study.

Reference	Method of Fabrication	Stitch Type	Linearity (R^2)	Gauge Factor	Working Range (%)	Hysteresis (%)
This study	Embroidering	N/A	0.77 ± 0.07	1.88 ± 0.51	26	8.54 ± 2.66
[51]	Stitching	Zigzag	0.98	1.61	50	6.25
		Chainstitch	0.96	3.71	25	15.1
		Overlock	0.83	0.1	16	0.98
		Coverstitch	0.97	0.21	18	2.02
[53]	Stitching	Zigzag	N/A	0.5	40	<1
[52]	Stitching	Chainstitch ¹	0.96 ± 0.01	-1.97 ± 0.12	21	34.68 ± 3.33
		Coverstitch ¹	0.97 ± 0.01	-1.12 ± 0.05	21	10.69 ± 4.99
		Chainstitch ²	0.94 ± 0.01	-2.25 ± 0.09	15	38 ± 6.18
		Coverstitch ²	0.93 ± 0.04	-1.01 ± 0.09	21	9.98 ± 2.14

¹ Stitched on a 4-way knit fabric; ² Stitched on a 2-way knit fabric.

3.5.1 Working Range

As shown in Figures 3.12–3.14, the working range of all three sensors decreased considerably over each stretching cycle to an overall 26%, which corresponds to the 40–66% strain. This could have

happened due to changes in the lockstitch formed between the needle and the bobbin thread during the embroidery of the sensor. Initially, when the sensor has just been fabricated, the lockstitch that forms the embroidery stitches is under a certain tension produced by the needle and the bobbin thread. If this tension is unbalanced due to differences in the weight between the needle and bobbin threads, or the tension parameters on the machine are not well adjusted, some looping may occur on either side of the fabric substrate. If these loops appear underneath the fabric, it is said that the bobbin thread tension is higher than the needle thread tension. When this happens, the conductive thread will move away from its initial position, which will produce an inconsistent number of contact points between the conductive thread and the underpath, or between adjacent conductive thread paths. In the case of the embroidered textile strain sensors presented in this study, small loops were observed underneath the fabric substrate, as shown in Figure 3.17. After stretching the sensor for the first time, the correctly formed lockstitches may have pulled the threads that were loose due to the loops formed. The change of the initial position of the thread caused a decrease in the working range of the sensor by increasing the amount of strain required to make the loose threads touch the embroidery underpath. In order to overcome this issue, slight modifications can be made during the sensor digitization phase. For example, increasing the row spacing between stitches may reduce the number of inconsistent contact points due to tension issues with the embroidery machine.

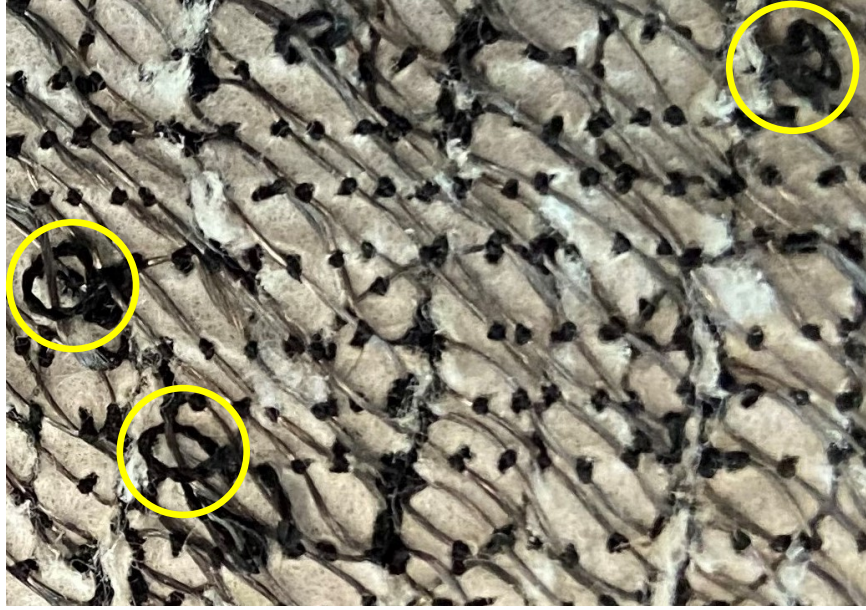


Figure 3.17: Formation of loops (circled in yellow) underneath the fabric substrate. These loops are produced due to thread tension imbalances that affect the performance of the sensor over a continuous number of stretching cycles.

3.5.2 Linearity

Regarding the linearity of the sensors, the results presented in Section 3.4.2 demonstrate that the sensor is only linear during the first 10 cycles. For the remaining 90 stretch cycles, the sensor demonstrated a nonlinear behaviour, as shown in Figures 3.12–3.14. However, it is important to mention that all of the three sensors show a slow decrease in their resistance at the beginning of their working range (40–55% strain), which seems to be linear. Moreover, on the last part of their working range, the sensors demonstrate a steeper decrease in its overall resistance. Individually, these two changes in resistance demonstrate a linear behaviour that could be useful for applying linearizing techniques. A major issue with strain sensors is that they tend to demonstrate nonlinear behaviours in the form of an exponential or logarithmic change in resistance with respect to strain, by demonstrating a non-monotonic behaviour, or simply by showing a high amount of hysteresis. However, these nonlinearities can be minimized by applying deep learning techniques to create a linear model of the electrical performance of the sensor. As explained before, data from the change in resistance due to strain are a form of a time series data. This characteristic allows for the application of methods that can infer the nature of the data from past and present values.

For example, in the study performed by Oldfrey *et al.* [87], a long short-term memory (LSTM) network was used to linearize the strain data from a stretchable conductive fabric. The results from that study demonstrated that an the LSTM network was able to accurately track the changes in resistance due to a change in the length of the conductive fabric. Similarly, in the study by Nguyen *et al.* [88], different linearizing methods such as LSTM networks, gated recurrent units (GRU), fully convolutional networks (FCN), and temporal convolutional networks (TCN) were tested on multiple datasets corresponding to strain sensors to compare their linearizing performance. Nguyen *et al.* demonstrated that both LSTM and TCN were good candidates for linearizing the strain data. This indicates that even when the embroidered sensors presented in this study showed a nonlinear behaviour, it would be possible to implement the linearizing techniques discussed to improve the sensor performance.

3.5.3 Sensitivity

With respect to the sensitivity, the results demonstrated in Table 3.1 indicate that the sensors presented in this study demonstrate improved performance over some of the other sensors presented in the literature. For example, the sensors presented in [51] demonstrate a gauge factor between -0.0059 and 1.56 for different stitches after stretching their sensors for 99 cycles. In the case of the sensors presented here, the gauge factor varied between 1.012 (Sensor S2) and 1.713 (Sensor S3) after 99 stretching cycles. In another study [53], a gauge factor of approximately 0.5 was presented. When comparing this value to the average gauge factor of 1.491 ± 0.465 from the sensor that had the lowest score (Sensor S2), it can be observed that Sensor S2 performs the best.

Furthermore, after observing the average gauge factor of the three embroidered strain sensors, it can be observed that its value falls somewhere in between those presented by Dupler and Dunne [52]. In their study, they created different strain sensors by stitching them at different angles on a fabric substrate. The sensors developed using that technique demonstrated an average gauge factor between -1.01 and -2.24 .

3.5.4 Repeatability and Hysteresis

In order to discuss the repeatability of the sensor, it is important to also discuss the hysteresis behaviour of the embroidered textile strain sensors. As observed from Figures 3.12–3.14, a constant hysteresis decrease after cycling was observed. Table 3.1 shows that this decrease in hysteresis happened most noticeably after the first 10 stretching cycles. From Cycles 10 and 11, the sensors demonstrated a large reduction in their average hysteresis, which went from 42.73 ± 16.68 to 8.54 ± 2.66 . Typically, hysteresis is produced by intrinsic properties of the material, or by the friction caused between the thread when it is stretched [47]. However, this behaviour is only common in the case when the strain sensor is made using other techniques such as knitting. In the case of the sensors presented in this study, the reduction on the hysteresis can be explained by changes in the physical characteristics of the conductive thread. The conductive thread used is made of 90 fibres of $14 \mu\text{m}$. These fibres are plied together to form a single strand of conductive thread. When the conductive thread is subjected to a continuous mechanical motion, such as the one that happens during the stretching of the embroidered strain sensor, the fibres forming it change its initial position (Figure 3.18). This rearrangement of fibres creates gaps within the conductive thread that cause the overall hysteresis to decrease by preventing any further mechanical changes within the structure of the conductive thread.

As for the repeatability of the sensor, the change in position of the fibres of the conductive thread causes a drift on the performance of the sensors, as an increase in resistance can be observed. This behaviour can also be confirmed by Figures 3.9–3.11, in which a rapid decrease in resistance is observed during stretching, but a slower increase in resistance happens during the unstretching phase of the sensor.

The second reason as to why the sensor drifts over time can be explained by the heating produced due to currents flowing through the sensor. Similarly to traditional strain gauges, textile strain sensors act as resistors, in which the amount of current that flows through them varies depending on the strain applied. Unfortunately, this current dissipates in the form of heat, which causes an increase in the temperature of the sensor. This increase in temperature causes the output of the sensor to vary, therefore reducing its repeatability.

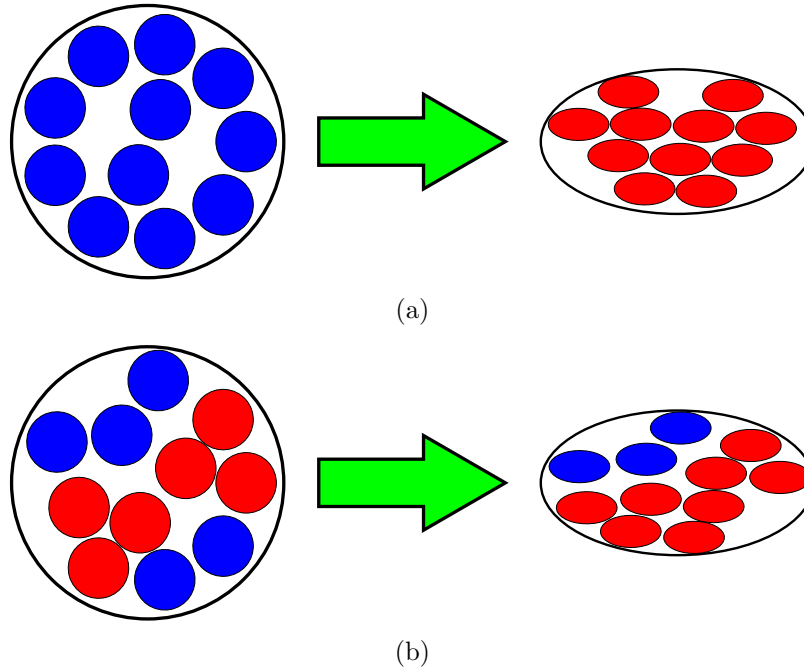


Figure 3.18: Rearrangement of fibres within the conductive thread used. **(a)** Initial position of the fibres. Each blue dot represents a fibre that is not in contact with neighbouring ones. When the sensor is stretched, the cross-sectional area of the conductive thread decreases, which increases the total number of fibres that touch each other (red dots). **(b)** Position of the fibres within the conductive thread after unstretching the sensor. Some of these fibres remain in contact with their neighbouring ones, which decreases the overall resistance of the sensor and its working range. When stretching the sensor consecutive times, some of the fibres stop contacting each other, which affects the ability of the sensor to detect changes in resistance.

Finally, the conductive thread used could have become damaged during the first stretching cycles, if the stitch direction set during the digitization step (Section 3.2.2) was aligned with the stretching direction. As mentioned before, this alignment should be avoided, especially if the type of stitch used is a running stitch, as being stretching in the same direction as the stitch direction may cause thread breakages.

Although the sensors demonstrate a non-repeatable behaviour, this only happens during a few initial cycle iterations. From Figure 3.15, it can be observed that the performance of the sensor stabilizes after the 40th stretching cycle for all of the three sensor samples. This performance remains constant for the remaining cycles, which is an indication of good repeatability. Furthermore, this behaviour shows that the sensors need to be conditioned by pre-stretching them a couple of

cycles before being usable, which is similar to what other studies have found [51, 89]. This pre-stretching is usually necessary because during the first few stretching cycles, some thread slippage may occur [47], the thread may suffer from creeping, or some microsnaps may be produced on the fibres that form the conductive thread, which could change its overall resistance.

3.5.5 Reproducibility

The sensors presented in this study demonstrated consistent reproducibility between stretching cycles, as shown in Figure 3.16. However, it is important to address an important aspect regarding the reproducibility of the sensors. As observed on Figure 3.16, the standard deviations of the average cost function for some comparisons were relatively high. This was because sensor pairs had similar higher scores than others. An example of this comparison is shown in Figure 3.19, in which the similarity plots from the 10th cycle are shown.

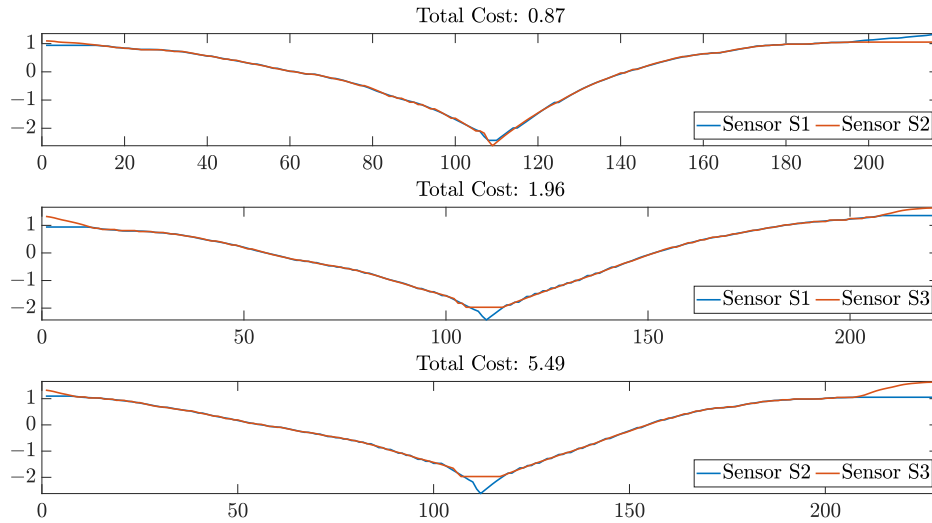


Figure 3.19: Data similarities assessed by applying the DTW technique on the resistance data of each sensor pair for Cycle 10. The y axis on each plot represents the normalized resistance data; and the x axis on each plot represents the resistance sample number compared during the computation of the warping path of the DTW algorithm.

Data shown in Figure 3.19 correspond to the average cost obtained from sensor pairs that had the lowest DTW scores. It can be observed that the sensor pairs that were the most similar between each other were Sensors S1 and S2. On the other hand, sensor pairs that included Sensor S3 were the ones that had fewer similarities between each other. This could be because during the

10th cycle, specifically, Sensor S3 demonstrated a higher normalized change in resistance, which increased the distance between samples computed during the DTW algorithm. However, as the sensor response stabilized over cycles, as shown in Figure 3.15, the similarities between sensors increased considerably. For example, during the 40th stretching cycle, all of the sensors had the highest similarity score, with the sensor pair S2 and S3 being the most similar (Figure 3.20).

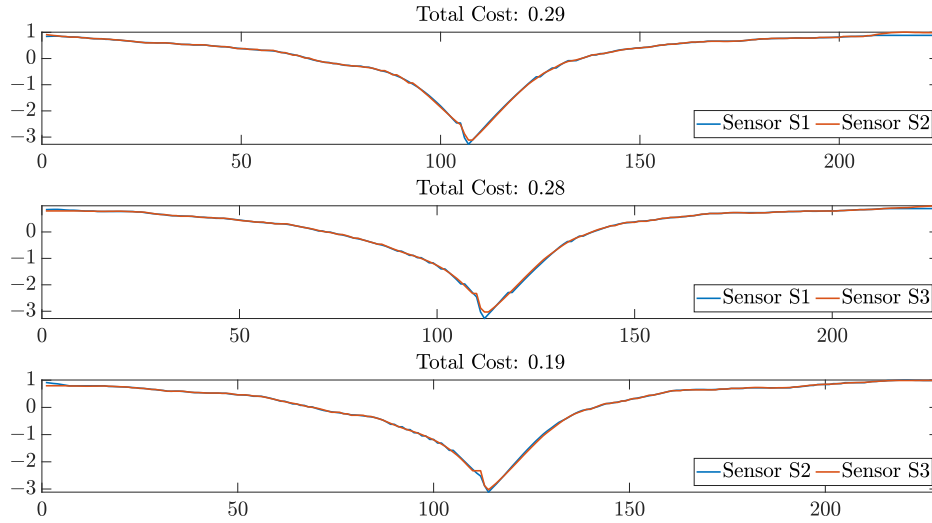


Figure 3.20: Data similarities are assessed by applying the DTW technique on the resistance data of each sensor pair for Cycle 40. The y axis on each plot represents the normalized resistance data; and the x axis on each plot represents the resistance sample number compared during the computation of the warping path of the DTW algorithm.

3.6 Conclusions and Future Work

The work presented in this study aimed towards the design of embroidered resistive textile strain sensors for use in soft robotic wearable mechatronic devices during robot-assistive therapies. The purpose of the study was to demonstrate the steps required to create a sensor that does not require a complicated fabrication procedure and that can be mass-produced. Moreover, the difference between stitching and embroidery was highlighted, and the advantages that the embroidery technique has over stitching were shown.

Furthermore, to demonstrate the feasibility of the design steps for the embroidered strain sensor, three sensor samples were created using the proposed methods, and they tested over 100

stretching cycles. In general, all of the three sensors demonstrated good sensitivity, which is comparable to recent textile strain sensors, low hysteresis behaviour, and good repeatability, as the performance of the sensor was similar after the 40th stretching cycle. However, room for improvement exists. For example, it was demonstrated that the working range of the sensors shown in this study was about 26%. As discussed by Jansen [47], the suggested working range for strain sensors used for motion tracking applications should be at least 30%. Therefore, future work should focus on increasing the working range of the embroidered textile strain sensor by tuning the embroidered parameters shown in Section 3.2.2, changing the overall embroidery design, or implementing a strain divider model, such as the one presented in the study performed by Basla *et al.* [90]. The implementation of the strain divider would be an interesting approach, as it would allow the sensor to keep the same embroidery design by adding another elastic band with a higher stiffness coefficient in parallel with the embroidered textile strain sensor. This would cause a proportional change in strain on the sensor with respect to the strain applied to the elastic band.

Regarding the repeatability of the embroidered textile strain sensor, it would be beneficial to increase the performance showed in this study. It is well known that strain sensors drift over time due to changes in the physical properties of the materials used and changes in their internal temperature. To help with this drifting behaviour, future work should focus on implementing sophisticated techniques such as transfer learning [91], to reduce changes in the electrical performance of the sensor as much as possible. Transfer learning is a useful technique, as it would allow the sensor to adapt to unknown changes by slowly shifting their data distribution until a point where this data distribution does not change significantly.

Future work should also focus on implementing the sensors created using the steps shown in this study in a sensor fusion scenario [92]. By combining the embroidered textile strain sensors with other textile sensors, such as embroidered electromyography sensors [76], it would be possible to improve the control of wearable mechatronic devices used during robot-assisted therapies. In this sense, by embedding these sensors directly on the garments, there is potential for reducing the sources of noise that traditional hard sensors present. Furthermore, embedding the sensors directly onto the garment would allow for a reduction in the number of wires required for communication, by substituting these wires with conductive thread [93,94]. However, before being able to use the

textile strain sensors in a wearable mechatronic system, it would be important to properly isolate them, as sweat and other impurities can affect their correct functionality. This could be conducted by embedding the sensor within a non-conductive fabric that is also waterproof, such as neoprene. Finally, it would be beneficial to test the strain sensor over a higher number of stretching cycles (in the order of the thousands), as certain factors not mentioned in this paper, such as fatigue [89], can affect the performance of the strain sensor in the long run.

Chapter 4

Performance Evaluation of Embroidered Honeycomb Textile Strain Sensors

4.1 Introduction

Textile wearable sensors have been gaining popularity in recent years as an alternative to traditional non-soft wearable sensors. This is especially important in the context of upper limb rehabilitation and monitoring, as textile wearable sensors have the advantage of being able to easily conform to the human body in an unobtrusive way. This characteristic enables soft wearable sensors to be used outside the rehabilitation clinic. For example, by using textile strain sensors it would be possible to collect motion data during activities of daily living, which would provide physicians with a better understanding about the recovery progress of their patients.

Many studies have focused on the development of textile strain sensors based on resistive [95,96], capacitive [97,98], or inductive [59,99] sensing. In contrast with capacitive and inductive sensors, resistive textile strain sensors do not need a complex data acquisition interface, produce signals that are simple to analyze during postprocessing [100], and do not require expensive shielding against electromagnetic interferences that affect capacitive and inductive sensors [101].

Most resistive textile strain sensors are fabricated using different techniques. For example, these sensors can be developed by creating conductive fibres, such as carbon nanotube (CNT) fibres, and combining them with polymers such as polydimethylsiloxane (PDMS) [102]. Other methods of fabrication include crack-based strain sensors, such as the one developed by Lu *et al.* [103]. In their study, a resistive strain sensor was created by stretching a nylon fabric coated with a mixture of multiwalled CNTs and polyvinyl butyral (PVB). This stretching produced microcracks on the surface of the nylon fabric, which caused a change in the resistance of the sensor on successive stretching cycles. Another example of textile resistive sensors includes those made using screen printed techniques [104]. Resistive sensors made using this method experience an increase in their base resistance when stretched, due to a separation of conductive particles inside the ink used during the fabrication process.

Although these methods have shown great results, they have the disadvantage of having high production costs and not being easily scalable [36]. This is why many studies have opted for simpler methods such as knitting [105], weaving [106], embroidering [66], and stitching [107]. These four methods make use of conductive thread (*e.g.*, silver plated polyamide thread or stainless steel thread) during fabrication to create a sensor that changes its resistance during stretching. Depending on the fabrication method, the conductive thread may be intertwined perpendicularly (woven), used to create a series of loops interlaced together (knitting), or stitched in certain patterns to create a series of electrical contact points that, when pressed or separated, create a change in resistance on the sensor.

Unfortunately, having a sensor that relies on contact points to detect a change in resistance imposes some problems. For example, the main disadvantage of woven structures is their limited stretchability capabilities, which is why most woven resistive sensors are typically used in pressure sensing applications [108–110]. In the case of knitted resistive sensors, thread slippage and change in the knitted geometry often occur the longer the sensor is used [47]. This affects the number of contact points in the knitted geometry, which change the resistance measurement of these sensors. A similar behaviour can be observed in stitched sensors, as stitches deform under tension applied at specific angles [111]. This deformation also changes the number of contact points between stitches, resulting in discrepancies on the resistance readings of the sensors.

Embroidered resistive strain sensors on the other hand, can be constructed to avoid stitch deformation issues by creating patterns that do not heavily base their change in resistance on the number of contact points between the conductive thread, as embroidered structures are formed by a series of straight stitches (known as running stitches) that do not create gaps when stretched. Instead, when running stitches are stretched, their resistance behaviour is affected by the physical changes in the conductive thread itself. These changes will vary depending on the type of conductive thread used. For example, stainless steel thread will show a reduction in its resistance due to its filaments bundling up together more tightly under a longitudinal force [66]. In the case of silver plated conductive threads, the resistance change will come from cracks formed in the coating on the surface of the thread [112]. These cracks will create openings as the thread is put under strain, which will cause an increase in the conductive layer base resistance.

Although these characteristics provide embroidered strain sensors with great potential, there are challenges that need to be addressed first before using these sensors in motion tracking applications. For instance, embroidered patterns need to be placed onto an elastic fabric substrate using a low-density stitch count during the embroidery process to enable them to stretch. This low density may lead to tension issues where the stitches forming the embroidery pattern get loose over time. As this tension is lost, stretching of the conductive thread in the embroidered pattern decreases, causing little to no changes in the resistance of the sensor [66]. Also, the constant application of stretching forces on the sensor can cause irreparable damages to the conductive thread, thus, affecting its sensing capabilities.

To address these issues, this work presents a novel embroidered strain sensor using a honeycomb pattern. The rationale behind using these patterns is that they have the property of enduring high deformation forces by distributing the resulting strain across localized areas in the honeycomb pattern [113–115]. This property can be beneficial for the embroidery strain sensor, as the honeycomb pattern will allow the sensor to be stretchable, while preventing tension issues due to stretching. The following sections present the procedure used to test the performance of the embroidered honeycomb pattern created using a silver-plated conductive thread. Also, the steps followed to select the best honeycomb geometry are described. Finally, the embroidered strain sensor was assessed in terms of working range, hysteresis, and repeatability.

4.2 Materials and Methods

4.2.1 The Honeycomb Model

As stated before, the textile strain sensor presented in this study was fabricated using an embroidered honeycomb pattern. This pattern consists of a unit cell that is repeated along the length of the sensor as shown in Figure 4.1. The unit cell is symmetric across the horizontal plane, and its shape is given by five parameters: the length of the cell diagonal walls (l), the length of the horizontal wall (h), the angle (θ) between a diagonal wall and an imaginary line normal to the horizontal wall, the diagonal wall thickness (t_l), and the horizontal wall thickness (t_h). When the honeycomb cell is subjected to an external axial force, the diagonal walls of the cell will tend to angle outwards, which will increase the θ angle, and creating a deflection of the horizontal walls (Figure 4.2). By adjusting the five cell parameters, it is possible to control the amount of deformation of the unit cell, which will also affect the stretchability of the sensor.

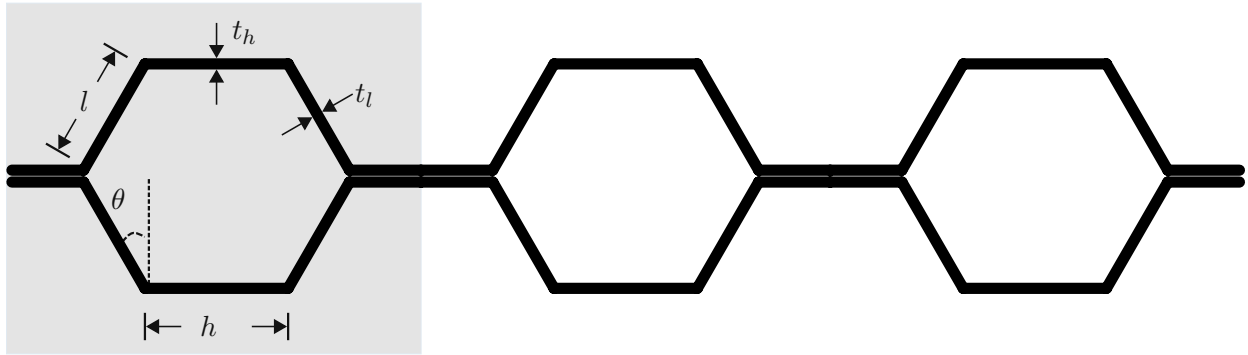


Figure 4.1: An example of a honeycomb pattern based on an hexagonal unit cell. The unit cell (highlighted in grey) is repeated three times on the horizontal direction. The length of the diagonal wall in the unit cell is represented by the variable l , variables t_h and t_l indicate the horizontal wall and the diagonal wall thickness, respectively; h represents the length of the horizontal wall, and θ corresponds to the angle formed between the diagonal wall and an imaginary line normal to the horizontal wall.

In this study, a rectangular shape was considered for the honeycomb unit cell. This shape was selected because it would be capable of providing more robustness to the cell walls, however, with the trade off of reduced stretching capabilities of the sensor. Other shapes were considered for the honeycomb pattern, such as a diamond shape. However, preliminary studies showed that diamond

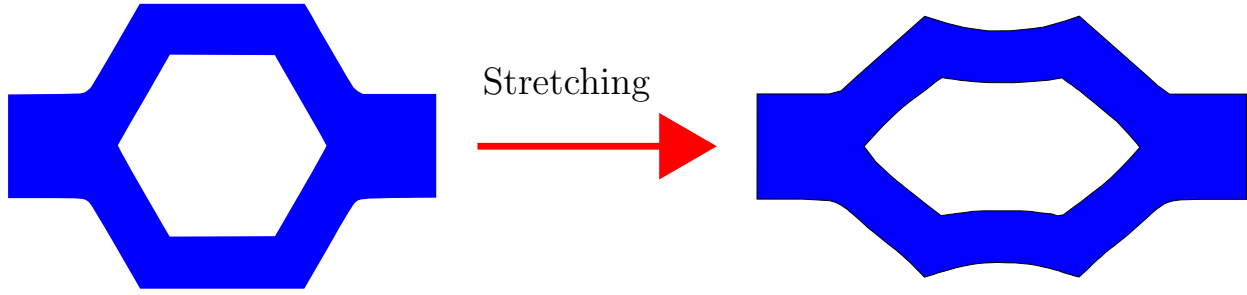


Figure 4.2: Deformation of the honeycomb cell due to stretching in the horizontal plane.

shape patterns required thin cell diagonal walls to be able to stretch. These thin walls ended up breaking after the stretching, making them not suitable for this application. The rectangular honeycomb structure was created using the following values: $l = 8$ mm, $h = 14$ mm, $t_h = 3$ mm, $t_l = 6.5$ mm, and $\theta = 0^\circ$. These values were chosen to satisfy the dimension constraints of the embroidery hoop used, which had an embroidery area of 40 mm \times 100 mm. Using these parameters, the final dimensions of the embroidered strain sensor were 25 mm \times 90 mm.

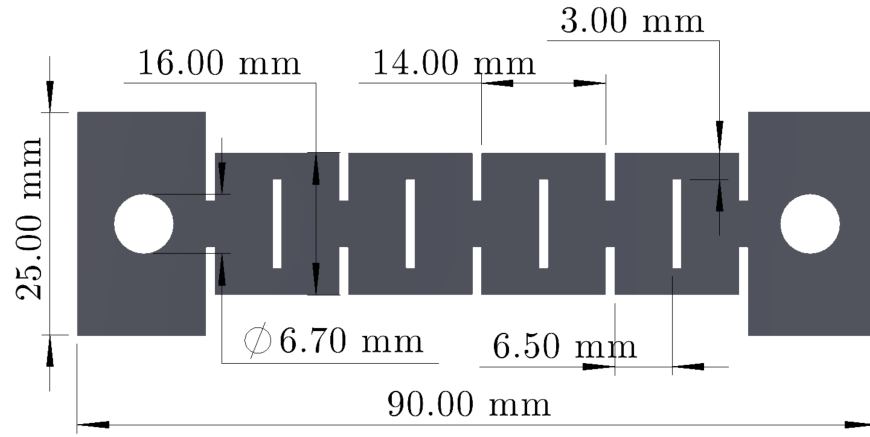
4.2.2 Sensor Fabrication

Following the development of the honeycomb patterns the resistive textile strain sensor was created following the steps highlighted in [66]. First, each resistive strain sensor was designed in SolidWorks 2021 (Dassault Systèmes, SolidWorks Corporation, Waltham, MA, USA) to create a computer aided design (CAD) model with an accurate geometry of the honeycomb shapes (Figure 4.3a). Then, the CAD model of each honeycomb pattern was digitized using the Inkstitch extension for Inkscape (Inkscape Project, Version 1.3). Because the stitches created using conductive thread would be bundled up together in the final embroidered design, it was important to minimize the amount of surface area covered by the conductive thread during the digitization process. This was required because the contact points between the conductive thread would create an array of resistors in parallel, which would reduce the base resistance of the completed sensor. Therefore, the conductive thread was digitized as a fill stitch of 3 mm to cover small areas of the honeycomb pattern in the final embroidered design. These areas were connected together using a running stitch, as shown in Figure 4.3b. Another fill stitch was digitized so that a polyester non-conductive thread was used to cover the rest of the honeycomb pattern.

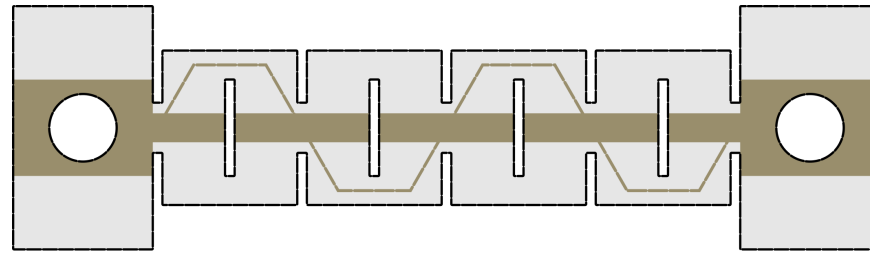
After the digitization step, the sensors were embroidered onto a 70%/30% polyester-rubber elastic band using a Janome Memorycraft 15000 automated embroidery machine and two layers of tear-away stabilizer. The elastic band was chosen to provide some elasticity to the embroidered sensor during stretching, as embroidered patterns tend to create rigid structures that have low stretchability properties. In the case of the tear-away stabilizer, two layers were used to prevent stitch deformations during the embroidery process. As for the conductive thread, a Madeira HC-40 silver plated polyamide thread (Madeira, USA) was used to embroider the strain sensor. In contrast with other conductive threads, the Madeira HC-40 thread was selected as it could be used as the upper thread in the embroidery machine. This was especially important as many non-technical embroidery machines (such as the one used in this study) require the conductive thread to be placed as the lower thread (*i.e.*, the bobbin thread), otherwise the conductive thread can get damaged and suffer from fraying.

The embroidery machine was set with an upper thread tension of 3.6 units and at the lowest speed possible (400 stitches per minute) to minimize damages to the conductive thread during the embroidery process [82]. Once the sensor was embroidered, the excess elastic band and the tear-away stabilizer were manually removed using scissors. Furthermore, the gaps of the honeycomb pattern were carefully cut to obtain the final sensor design.

Finally, to provide a connection interface to the hardware acquisition system, wires were added to the ends of the sensor using grommets as shown in Figure 4.3c.

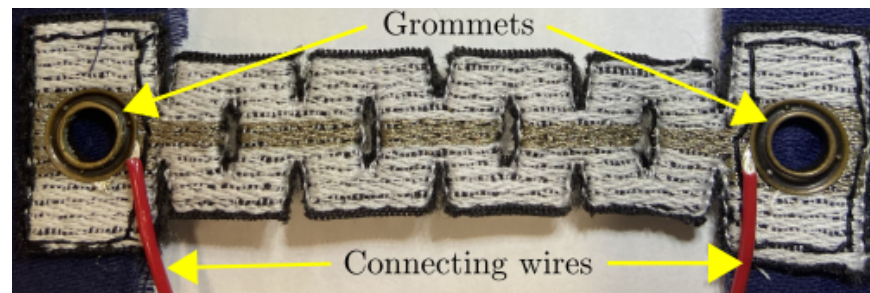


(a)



■ Conductive Thread □ Non-Conductive Thread

(b)



(c)

Figure 4.3: Rectangular shape honeycomb sensor fabrication process. (a) CAD model of the rectangular shaped honeycomb pattern. (b) The digitized rectangular shape honeycomb pattern. The path followed by the running conductive stitch to connect regions of the conductive fill is shown for demonstration purposes. This running stitch was covered by a non-conductive fill in the final design. (c) Embroidered textile strain sensor. Grommets are used to attach wires to the sensor.

4.2.3 Hardware Interface

Once the sensor was embroidered, it was necessary to create a data acquisition system capable of collecting data from the resistance textile strain sensor. The block diagram of this system is shown in Figure 4.4. First, a constant current Wheatstone bridge in a quarter bridge configuration was used to detect resistance changes in the sensor. The decision for driving the Wheatstone bridge with current instead of voltage was based on two main reasons. Firstly, constant current bridges are known to have less linearity errors at their output, which is beneficial for highly nonlinear sensors such as resistive-based sensors. Secondly, current driven bridges have the advantage of ignoring errors introduced due to long wirings, *i.e.*, when the sensing element is located far away from the main bridge circuit. These errors typically occur because long wires are more susceptible to changes in resistance due to heating. This change in resistance can modify the base resistance of the resistive element in the bridge, producing erroneous measurements [116].

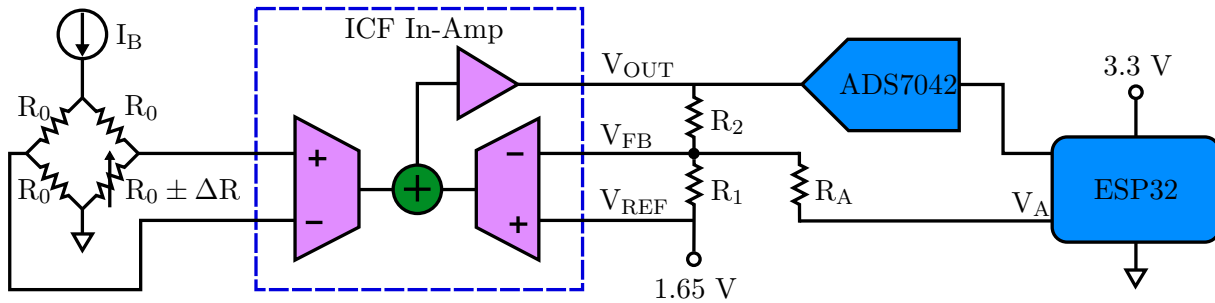


Figure 4.4: Embroidered textile strain sensor hardware interface. A current I_B is used to drive the Wheatstone bridge formed by four resistances R_0 , being one of these resistances the embroidered sensor. The change in resistance ΔR of the embroidered sensor produces a voltage at the output of the Wheatstone bridge, which is amplified by an indirect current feedback (ICF) instrumentation amplifier. The combination of the voltages V_A and V_{REF} , with resistors R_1 , R_2 , and R_A create a voltage V_{FB} used to offset any voltages produced by an imbalanced Wheatstone bridge. The output of the amplifier (V_{OUT}) is sent to the ADS7042 (a 12-bit analog to digital converter) controlled by an ESP32 microcontroller.

The output of the Wheatstone bridge was further amplified using an indirect current feedback (ICF) instrumentation amplifier (In-Amp). The main difference between a traditional instrumentation amplifier and an ICF In-Amp is that the latter possesses two transconductance stages, which convert the differential input and a portion of the ICF In-Amp output voltage into two currents

that get subtracted to achieve a balance state. This property is useful as specific external voltages can be added at the ICF In-Amp feedback loop to minimize offset voltage errors in the differential input terminals. In the case of Wheatstone bridge circuits, these offset voltages are produced due to high resistor tolerances, or due to variability introduced during the manufacturing process of the bridge sensing elements.

After the amplification stage, sensor data were digitized using the ADS7042 12-bit analog to digital converter (ADC), which was connected to an ESP32 microcontroller. Finally, the ESP32 microcontroller was in charge of sampling the sensor data, controlling the offset compensation voltage of the ICF In-Amp, and sending the data through serial communication to a PC where it was further processed and analyzed.

The resistor elements of the Wheatstone bridge and the ICF In-Amp were selected by analyzing the circuit shown in Figure 4.4. First, the transfer function of the circuit was obtained using the following equation [117]:

$$V_{OUT} = \left(1 + \frac{R_2}{R_1} + \frac{R_2}{R_A}\right) \cdot V_{IN} - \frac{R_2}{R_A} \cdot (V_A - V_{REF}) + V_{REF}, \quad (4.1)$$

where V_A is the offset compensation voltage set by the ESP32 internal 8-bit digital to analog converter (DAC); V_{REF} is the reference voltage equal to 1.65 V; R_1 , R_2 , and R_A are the resistors used to set the gain of the ICF amplifier; and V_{IN} is the ICF In-Amp differential input given by the equation below.

$$V_{IN} = I_B \cdot R_0 \left(\frac{\pm \Delta R}{4R_0 \pm \Delta R} \right), \quad (4.2)$$

where I_B is the constant current driving the Wheatstone bridge, R_0 is the base resistance of the embroidered sensor, which matches that of the other resistors in the legs of the bridge, and ΔR is the change in resistance of the sensor.

Because the magnitude of the change in ΔR produced a small differential input voltage, R_1 , R_2 , and R_A in Equation (4.1) were set to 1 k Ω , 97.6 k Ω , and 49.9 k Ω , respectively, to achieve a gain of 100.

4.2.4 Experimental Setup

Before testing the embroidered strain sensor, it was necessary to overcome the low displacement due to the honeycomb pattern used. As mentioned in Section 4.2.1, the rectangular shape pattern allows the sensor to be more robust to inline forces with the drawback of having a reduced stretchability. For this reason, a strain divider [90] was implemented to compensate for this limitation. The procedure implemented was follows:

First, using velcro hooks, the embroidered sensor was placed in parallel to an additional elastic band (EB_1) made of the same materials as the elastic band used for the sensor. This was done to aid in the recovery process of the sensor shape after being stretched. Then, assuming that the sensor behaved as a spring, a third elastic band (EB_2) of the same length as the sensor was placed in series with it so that the overall arrangement of the two elastic bands and the embroidered sensor had a small spring constant. According to Hooke's law, this small spring constant would allow the embroidered sensor to stretch at a slower rate, as most of the force required to stretch the sensor was distributed equally between the sensor, EB_1 , and EB_2 . However, it was noted during experiments that the elastic band in series with the sensor exhibited significant elongation before the sensor itself showed any noticeable stretching. Therefore, a fourth elastic band (EB_3) was placed in parallel to EB_2 (Figure 4.5), to minimize the amount of elongation needed on EB_2 to stretch the embroidered sensor.

Having implemented the strain divider system, four sensor samples were created. One of the sensor samples was used to test the maximum strain limit that could be achieved while the sensor was attached to the strain divider system explained before. To do this, the strain divider system was clamped on both ends to a linear motion mechanism that consisted of a lead screw that was driven by a motor controlled by an EPOS2 24/2 driver (Maxon Group, Sachseln, Switzerland) (Figure 4.6). Then, the strain divider system was stretched 5 mm at a constant speed of 69 mm/min, unstretched back to its original length, and then stretched the previous length plus an additional 5 mm each time. This process was repeated until the sensor presented signs of slacking due to the sensor deforming as shown in Figure 4.7.

The testing explained above showed that a maximum displacement of 50 mm could be achieved

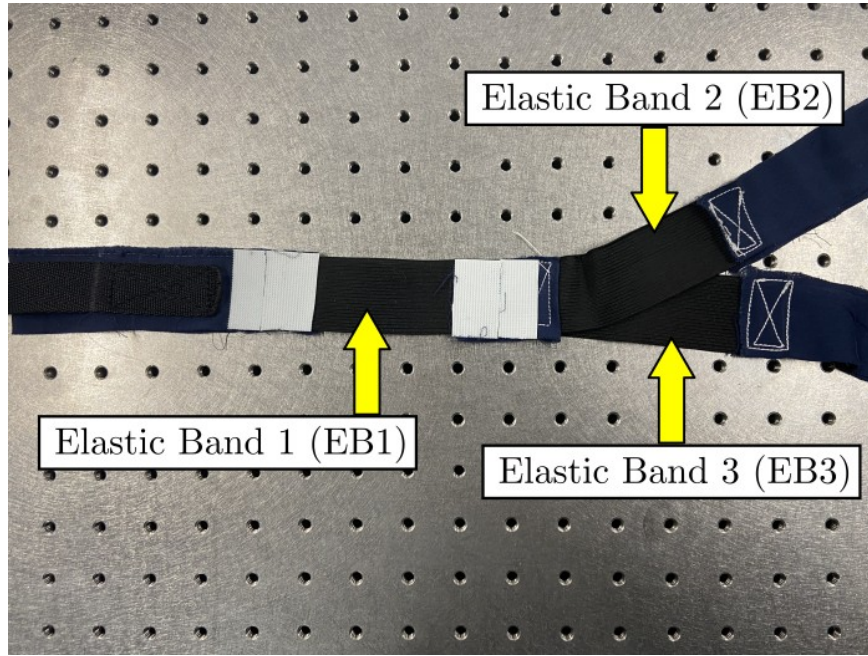


Figure 4.5: Top view of the strain divider system. EB1 is connected in series with the parallel arrangement of EB2 and EB3. The white squares are the velcro hooks used for attaching the embroidered strain sensor. Note that for clarity, EB2 and EB3 are shown splitting apart, but they are coaligned in the actual application.

(corresponding to a 55.56% strain) for the whole strain divider system without slacking. With the maximum displacement of the system found, the remaining three embroidered sensor samples were tested on the same mechanism. However, before testing it was necessary to first find the resistance value that would balance the Wheatstone bridge described in Section 4.2.3. To do so, the base resistance of each sensor sample was measured and an average resistance of $103\ \Omega$ was found between the three sensors. Therefore, a resistance of $100\ \Omega$ was used as the base resistance R_0 for the Wheatstone bridge, as this resistance was the closest standard resistor value to the average $103\ \Omega$ that could be obtained.

After finding the resistor values that would be used for the Wheatstone bridge, an offset compensation voltage that would minimize the errors on the bridge due to unmatching resistors was determined for each of the sensor samples. The importance of this compensation voltage lies in the fact that each sensor had a base resistance slightly different to the three fixed $100\ \Omega$ resistors of the bridge. Therefore, this voltage was found by measuring the output of the bridge with each of the sensor samples connected to it. For all of the sensor samples, a current of $1.7\ \text{mA}$ was used

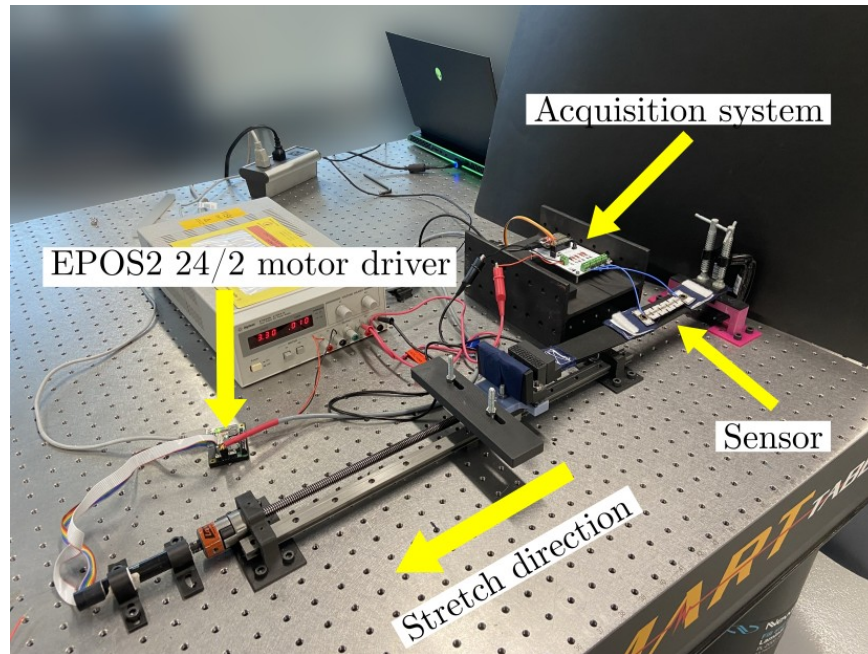


Figure 4.6: Linear motion testing setup used during data collection. The strain divider system with the sensor attached is shown clamped on each end to the linear motion mechanism, which is controlled by an EPOS2 24/2 motor driver. Data from the sensor are collected using a custom hardware acquisition system.

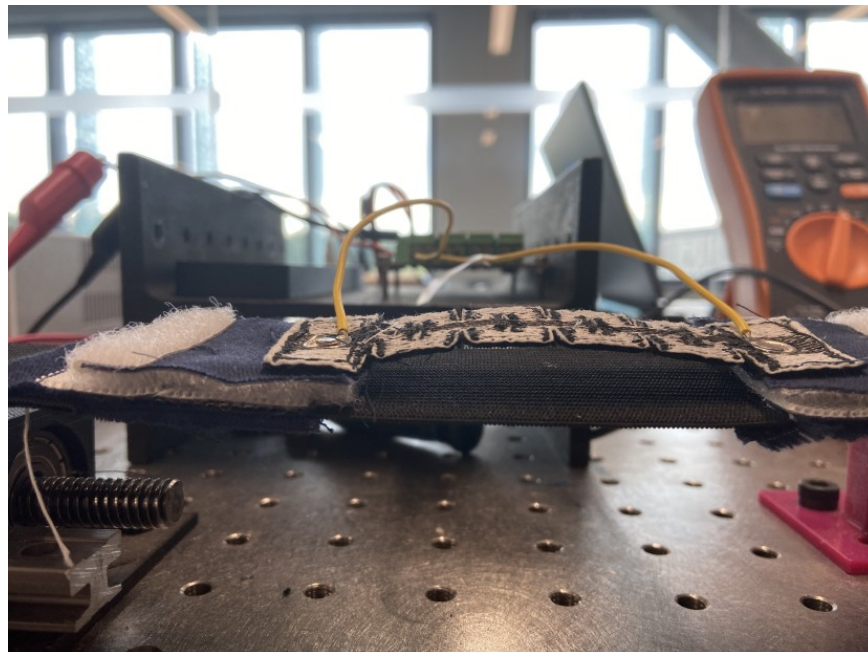


Figure 4.7: Slack on sensor due to deformation produced by overstretching.

to drive the bridge. The details of these measurements are summarized in Table 4.1.

Finally, to evaluate the sensors, each sensor sample was attached to the strain divider system, which was then stretched to 50 mm and unstretched to its original length at a constant speed of approximately 2.3 mm/s for 50 cycles. With this speed, a smooth motion was achieved and a total of 5436 samples were obtained per stretching cycle. Displacement data from the EPOS2 motor driver, and voltage data from the sensor after being collected by the hardware acquisition system were sent to a computer running a custom-made acquisition software for Python.

Table 4.1: Base resistance and compensation voltages measured for the sensor samples.

Name	Base Resistance R_0 (Ω)	Offset Voltage V_A (V)	Wheatstone Bridge Supply Current I_B (mA)
Sensor S1	95	1.55	1.7
Sensor S2	104.7	1.76	1.7
Sensor S3	109.2	1.86	1.7

4.3 Results

After experiments, data from each sensor were post processed in MATLAB R2021a (MathWorks, Inc., Natick, MA, USA). A window moving average filter with a window length of size 501 was used to smooth the data. Then, to assess the performance of the sensors while they were attached to the strain divider system, each sensor was evaluated using the metrics explained below.

4.3.1 Linearity and Working Range

The first performance metric assessed was the sensor linearity, which was calculated over the working range of each sensor sample. This working range was determined by the portion of the range that showed a non-constant and monotonic change of voltage within a specified range of strain [66]. To find the working range of each of the three sensor samples, the average of each sensor data was computed over the 50 stretching cycles. From the resulted averaged signal, the linearity and working range of each sensor sample was identified. A working range of 6.52–55.56% strain was found for Sensor S1, with both sensors Sensor S2 and Sensor S3 having a full 0–55.56%

working range (Figures 4.8b, 4.8e and 4.8h). As for the linearity, a line of best fit was used for each sensor over their respective working range. Sensor S1 had the lowest linearity score, with an R^2 of 0.77, followed by Sensor S2 and Sensor S3 with an R^2 of 0.82.

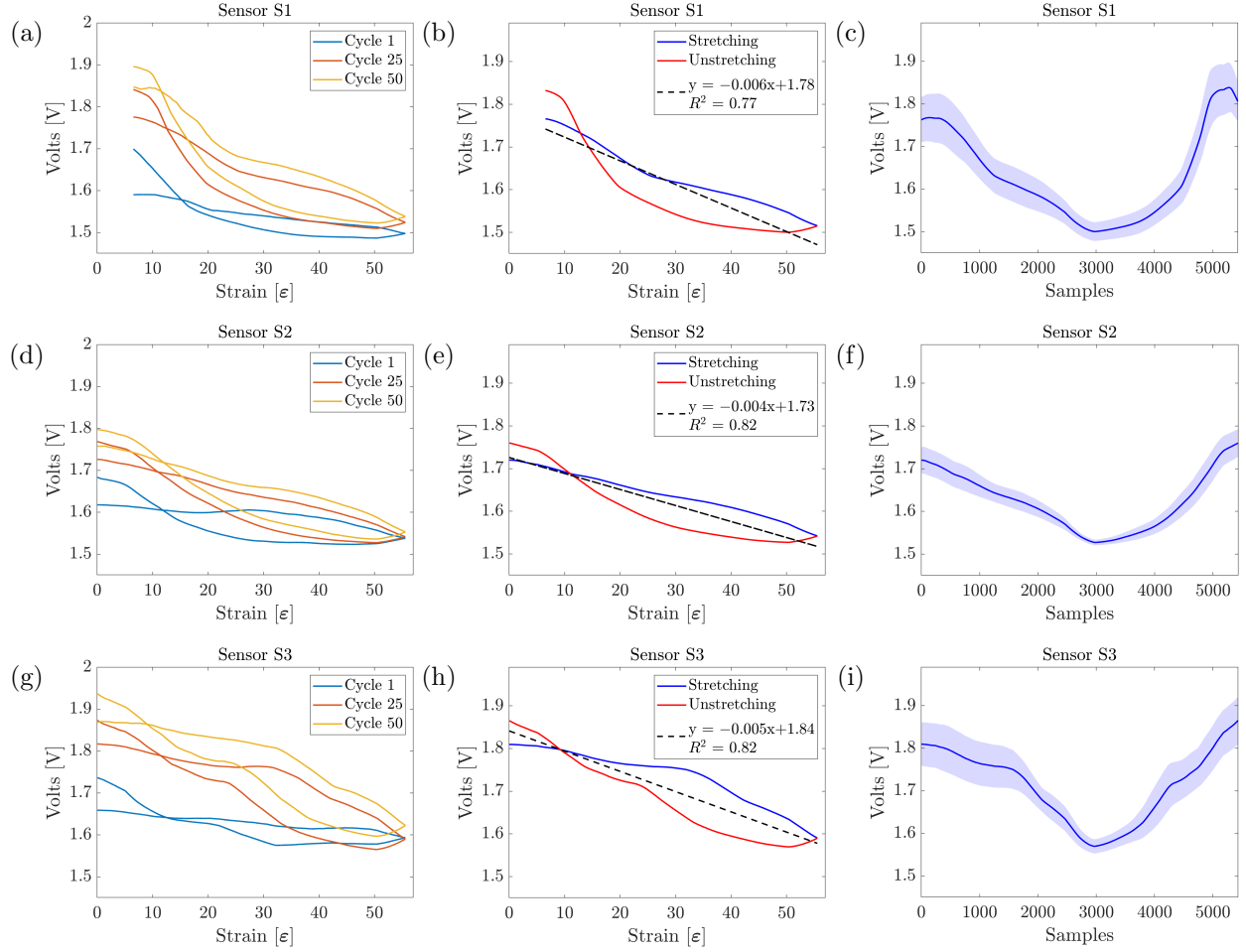


Figure 4.8: Sensor response in the presence of strain. Each row represents a sensor, Sensor S1 at the top, Sensor S2 in the middle, and Sensor S3 at the bottom. The first column represents the change in voltage due to applied strain over three cycles. The second column shows a line of best fit applied to the averaged data across all 50 stretching cycles. The third column shows the averaged data and its standard deviation (shaded region) represented as a time series data.

4.3.2 Sensitivity

After obtaining the working range and linearity of the sensors, their sensitivity was measured. This metric indicates the response of a sensor in the presence of stimulus, which in this case is given by

the strain applied. The ideal sensitivity of a sensor will vary depending on the application, as the sensor should be able to detect changes of what is being measured without affecting its accuracy. To represent the sensitivity of a sensor, a measure of the gauge factor (GF) was used. For the sensor samples tested, this measurement is given by the ratio of the change in voltage ΔV with respect to their base voltage V_0 , in the presence of an applied strain (ε), as shown in the equation below [66].

$$GF = \frac{\Delta V/V_0}{\varepsilon}, \quad (4.3)$$

where ε represents the ratio of the change in the sensor length (ΔL) to its original length L_0 .

Similar to the linearity, the sensitivity of all of the three sensors samples was obtained over their working range and using the averaged signal described in Section 4.3.1. For Sensor S1, a gauge factor of 0.31 was found. This was followed by Sensor S3 with a gauge factor of 0.22; and Sensor S2 with the lowest gauge factor of 0.19.

4.3.3 Hysteresis

Another performance metric assessed was the hysteresis of the sensor, H_ε . This metric is defined as the maximum deviation in strain $\Delta\varepsilon_h$ given a specific measured voltage. The hysteresis should be normalized between the maximum ε_{max} and minimum strain ε_{min} over the sensor working range, and computed as follows:

$$H_\varepsilon = \frac{\Delta\varepsilon_h}{\varepsilon_{max} - \varepsilon_{min}} \times 100. \quad (4.4)$$

An average $36.85\% \pm 4.95\%$ hysteresis was found for all the three sensor samples, with Sensor S1 showing the greatest hysteresis of 41.05% and Sensor S3 showing the lowest hysteresis with a value of 31.39%. Table 4.2 shows a summary of the average hysteresis of each sensor, including the sensitivity and linearity scores assessed in previous sections.

Table 4.2: Average performance metrics of each sensor average data.

Sensor Name	Linearity (R^2)	Gauge Factor	Hysteresis (%)	Working Range (%)
Sensor S1	0.77	0.31	41.05	6.52–55.56
Sensor S2	0.82	0.19	38.10	0–55.56
Sensor S3	0.82	0.22	31.39	0–55.56
Average	0.80 ± 0.03	0.24 ± 0.06	36.85 ± 4.95	

4.3.4 Repeatability

The final performance metric measured was the repeatability of the sensor. This metric refers to the amount of drift each sensor had over the span of each stretching cycle. The drift of each sensor can be observed in Figures 4.8a, 4.8d and 4.8g, where the response of each sensor on Cycle 1, Cycle 25, and Cycle 50 is shown. Sensor S3 shows the highest drift, followed by Sensor S1 and Sensor S2, with the later showing the least amount of drift. The amount of drift of each sensor can be understood better by observing Figures 4.8c, 4.8f and 4.8i, which show the average and standard deviation of each sensor sample across all cycles. These images show each stretching and unstretching cycle as time series data to help visualize the dispersion of the data.

4.4 Discussion

The results obtained show that the sensors presented in this study have sufficient working range to be used in human motion applications. For this type of application, a working range between 30% and 35% is required to accurately track limb motions [47]. In contrast to a previous study [66], in which the working range of the embroidered strain sensors decayed over time, each of the three sensor samples analyzed in this study maintained a constant working range throughout each stretching cycle. This can be attributed to the honeycomb pattern, which as explained before, distributed the stretching forces across the walls of the honeycomb unit cells. This is especially important considering that the reduction of the working range can happen due to stitches deforming in the presence of axial forces.

Regarding the linearity of the sensor, the average linearity of 0.80 ± 0.03 obtained between all three sensor samples shows an improvement over a previous study that implemented embroidered

strain sensors [66], where an R^2 of 0.77 ± 0.07 was obtained. Although this linearity is relatively low (0.8 vs. values above 0.9) when compared with the linearity of studies that implemented stitch-based resistive strain sensors, such as in [52], it is important to remember that stitch-based sensors can suffer from deformations in the contact points between the stitches. This can cause nonlinear behaviour over time, which makes embroidered strain sensors a better option. Furthermore, the low linearity of the sensors presented in this study can be attributed to the hysteretic behaviour shown by the sensor. This affects the computation of the R^2 value, as scattered data heavily affects the calculation of this parameter.

With respect to the sensitivity and hysteresis of the sensor samples, there is room for improvement. The low sensitivity of the sensors can be attributed to the strain divider system used in this study. As explained before, the strain divider system was used to overcome the limited displacement observed in the sensors. By controlling the rate of change in strain of the sensor using the elastic bands, it was possible to achieve a better working range, with the drawback of a reduced sensitivity. It could be possible then, to implement a different strain divider system that limits the rate of change in strain depending on the application for which the sensor is needed. For example, by creating a system that works on the range of 35% strain, the sensitivity of the embroidered sensor could be improved. Similarly, the hysteretic behaviour of the sensors may be a result of a combination of the strain divider system and the shape of the honeycomb cell used. Because the restoring force required for the elastic band EB1 in parallel with the sensor to regain its original length is less than the restoring force of the parallel arrangement of EB2 and EB3, it is possible that the sensor was close to regaining its original length before EB2 and EB3. This would also explain the overshoot observed in each stretching cycle during the unstretching motion as shown in Figures 4.8a, 4.8d and 4.8g.

As for the repeatability of the sensors, it can be observed in Figures 4.8a, 4.8d and 4.8g that each of the sensor samples drifted over time. Interestingly, each of the sensor samples shows a major drift between the first cycle and the remaining ones. This is inline with what other studies found, in which the resistive strain sensors developed needed to go through a prestretching phase. This prestretching varied between one cycle [51, 89] and ten cycles [66].

Finally, it is important to mention that the results also show that the sensor response is different

to what the theory of embroidered sensors described. It is well established that the resistance changes in the conductive thread are a product of the microcracks formed on the coating layer of the conductive thread. These cracks produce an increase of the base resistance of the conductive thread, which results in an increased output voltage (according to Ohm's law) detected by the hardware acquisition system described in Section 4.2.3. However, as shown in Figure 4.8, each of the sensor samples produced a decrease in voltage when stretched. Upon further inspection, it was noted that the sensor response was given by the conductive thread bundling together at the zones of the honeycomb pattern that deformed the most, as shown in Figure 4.9. Although, this indicates that the main mechanism that governs honeycomb embroidered sensors is due to a combination of structural changes in the conductive thread as well as contact points, embroidered honeycomb sensors have the advantage of being robust to resistance degradation as shown in their constant working range over all stretching cycles.

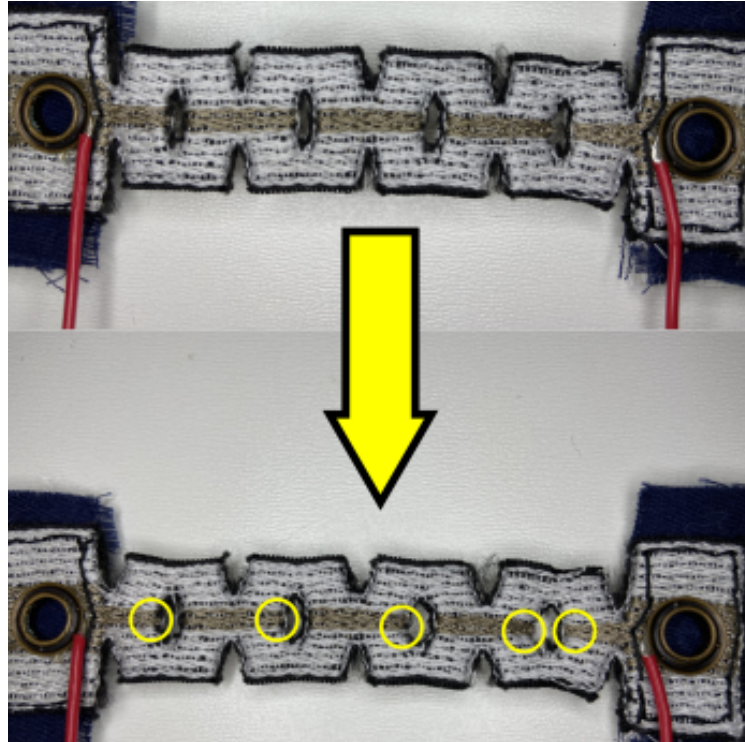


Figure 4.9: Unstretched sensor on top and stretched sensor on bottom. Circled in yellow are the bundling of threads occurring at specific regions of the honeycomb pattern after stretching. This bundling reduces the base resistance of the sensor, causing a drop in voltage read at the hardware acquisition system.

4.5 Conclusions and Future Work

In this study, a novel embroidered resistive strain sensor based on a honeycomb pattern was presented. The main advantage of this type of sensor over the ones found in the literature is that the sensing mechanism of these sensors is resistant to axial forces that can damage the conductive thread and affect the performance of the sensor in the long run. Another advantage of these sensors is that the forces acting on the sensor are distributed at specific regions of the honeycomb pattern, which helps to prevent damage to the conductive thread used. However, it is important to note that although effective, there is room of improvement in terms of sensitivity, linearity, and repeatability. To do so, future work should focus on the implementation of techniques aimed at solving these issues. For example, by implementing transfer learning and domain adaptation algorithms such as the ones used in [91], it would be possible to minimize sensor drift issues. Furthermore, by using other deep learning methods like the ones presented in [87], hysteresis and linearity issues can be avoided.

Overall, the sensors presented in this study are a stepping stone in the direction of frugal soft wearable sensors that could potentially be used in musculoskeletal rehabilitation of patients affected by musculoskeletal disorders or neurological conditions such as stroke.

Chapter 5

Effects of Dynamic Forces on Embroidered Textile Strain Sensors

5.1 Introduction

Stroke is a life-threatening cerebrovascular condition characterized by a sudden interruption of blood flow to certain parts of the brain. It is estimated that at least two thirds of stroke survivors present some type of post-stroke condition that severely impairs their upper limb motions [118]. Therefore, it is paramount for stroke survivors to engage in rehabilitation therapies to regain as much motor function as possible. These therapies can be further enhanced by using robot assistive devices as a complementary method to aid in the recovery process [92], as robotic devices are able to provide personalized assistance to stroke patients in the form of repetitive training motions [119].

Wearable mechatronic devices are one type of robotic assistive device used during upper limb rehabilitation therapies. The main advantage of these devices lies in their portability potential, as they can be attached directly to the patient's limbs, which opens the possibility of at-home rehabilitation therapies or constant monitoring and control. To facilitate this portability, several studies [3, 29, 120] have focused on the development of soft wearable mechatronic devices that aim to reduce the overall bulkiness of traditional exoskeleton-type devices. This can be achieved by substituting the hard actuators and sensors with soft versions of these elements. For example, some studies have explored the use of twisted coiled nylon actuators [121] or shape memory alloys [120]

instead of motors to produce motions. On the other hand, a significant amount of research has focused on the development of soft wearable sensors that can be used within the framework of soft wearable mechatronic devices. This is essential because sensors are the principal means of communication between the patient and the wearable mechatronic device, as they are used to detect changes within the environment, the user, and the device itself [9].

Among the different types of sensors used within wearable mechatronic devices, force and motion sensors are frequently used to provide feedback in terms of kinematic data and interaction forces between the user and the device [9]. With respect to motion sensors, recent studies have successfully implemented soft versions of this type of sensing modality. For example, in the study performed by Kim *et al.* [91], a silicon-based soft sensor was developed to detect the ankle position during walking. In another study [57], several soft capacitive strain sensors were embedded onto a shirt to estimate shoulder motions. Similarly, in [66] a method for fabricating textile strain sensors that have the potential of being used in wearable robotic assistive therapies was proposed.

In contrast to soft motion sensors, the use of soft force sensors has been limited to pressure sensing applications. For example in [122], capacitive textile sensors were placed on the tips of a sensorized glove to detect grasping forces. Similarly, in the study by Osborn *et al.* [123] a conductive resistive fabric was attached to different sections of a prosthetic hand to provide grasping feedback to the user. Some studies have tried to explore the use of soft force sensors to understand the effects of forces applied by the human joints during motion. An example of such study is the one conducted by Basla *et al.* [90], in which a soft stretchable force sensor was developed by combining Gallium-indium liquid metal with a microstructured silicone polydimethylsiloxane (PDMS) to detect forces exerted by the lower limbs during walking motions.

One of the reasons as to why very few studies have explored the use of soft force sensors outside pressure sensing applications is due the high production costs and low scalability challenges found during the development stage [36]. To address these issues simpler methods are required as a manufacturing alternative of soft force sensors.

One of these methods is embroidery, as it has the advantage of allowing mass prototyping of soft sensors due to the ease in its manufacturing process and widespread availability of equipment [66]. However, before creating soft force sensors using the embroidery technique, two main challenges

must be addressed. The first one is that embroidering uses a series of stitches (known as running stitches) that create rigid, non-stretchable structures once the embroidery process is finished. The second issue is related to the conductive thread used as part of the embroidery process. Typically, in embroidering applications, a silver-plated polyamide thread is used as the sensing element. When this thread is subjected to external forces, its conductive layer suffers damages that affect its ability to work properly.

Fortunately, these issues can be addressed by embroidering patterns that enable stretching without compromising the integrity of the conductive threads used. One of these patterns is the Kirigami pattern, which is characterized by a series of cuts that allow deformation of the material [124]. Therefore, in this study a Kirigami-based embroidered force sensor is presented. To assess the efficacy of the Kirigami design, the embroidered force sensor was tested under different dynamic conditions that included stretching the sensor at a slow, medium, and high speed. The outcomes of this testing on the embroidered sensor were analyzed in terms of linearity, sensitivity, hysteresis, and repeatability.

5.2 Materials and Methods

5.2.1 Mechanical Characteristics of the Kirigami Pattern

As previously stated, the sensors presented in this study were created following a Kirigami design (Figure 5.1). These patterns are characterized by a series of cuts placed on a laminar sheet that allow the material to stretch in the presence of forces (Figure 5.1a). When the Kirigami design is stretched, it goes through three main stages of deformation, as shown in Figure 5.1b. During the first stage, the Kirigami structure shows a linear response that satisfies Hooke's law. It is during this first stage when the gaps of the Kirigami design start to separate, causing the Kirigami material to show an in-plane deformation. When the Kirigami structure reaches a critical point, known as the critical buckling strain point [125,126], the out-of-plane and the in-plane deformation forces acting on the Kirigami structure become equal. It is at this point when the second stage starts and the mechanical response of the Kirigami structure plateaus producing a quasi linear response. Finally, after this short deformation stage, the Kirigami structure enters the final stage,

when it becomes stiffer and starts showing signs of plastic deformation.

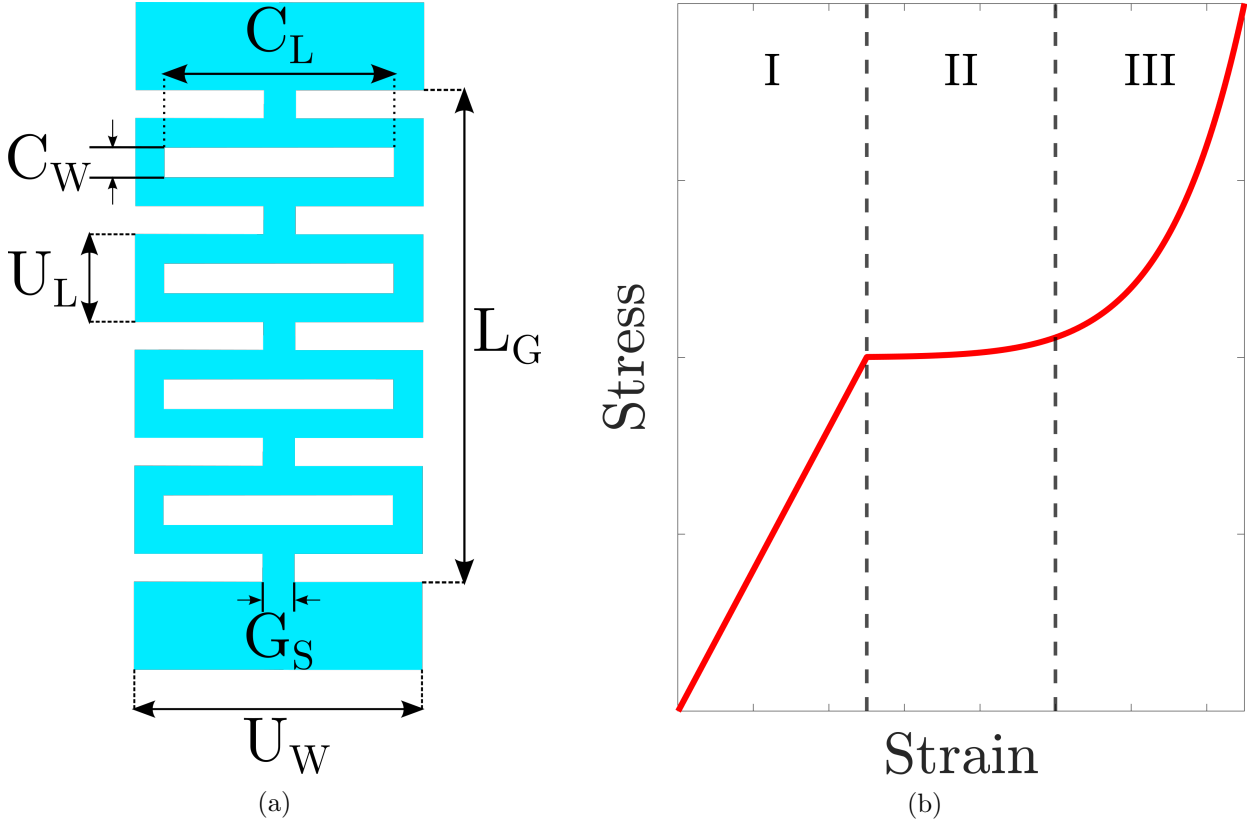


Figure 5.1: (a) An example of a Kirigami pattern depicting the pattern cut length (C_L), cut width (C_W), gap spacing (G_S), stretchable length (L_G), the unit cell width (U_W), and the unit cell length (U_L). (b) Typical stress-strain curve of a Kirigami structure. As the Kirigami pattern is stretched it undergoes through three stages of deformation. Stage I corresponds to a linear response, which is related to an in-plane deformation. Stage II indicates the area where the Kirigami pattern undergoes an out of plane deformation. Stage III is the final stage of deformation, when the Kirigami pattern shows signs of stiffening. Note that no scale is provided for the x and y axis, as no real data were used in this example.

Several studies [125–127] have shown that the amount of strain produced on each deformation stage of the Kirigami structure, and its mechanical properties are dependent on the dimensions of the cuts applied to the Kirigami design. The location of these cuts are shown in Figure 5.1a and have the following parameters: the cut length (C_L), which is the length of the cuts placed across the middle portion of the Kirigami pattern; the cut width (C_W), which is the width of all the cuts placed across the Kirigami pattern; the gap spacing (G_S), which is the gap separating the cuts

placed on the sides of the Kirigami design; the unit cell width (U_W) and the unit cell length (U_L), which are the dimensions of the rectangular pattern with the middle gap that is repeated across the Kirigami design; and the stretchable length (L_G), which defines the stretchable portion of the Kirigami pattern.

In a traditional Kirigami design, all of these dimensions should scale proportionally to each other. However, this is hard to achieve in applications that constrain the space of structures to a small area, such as in e-textile applications [65]. Therefore, in this study the Kirigami parameters were determined experimentally in order to achieve a stretchable structure that fitted in an area of 90 mm long by 25 mm wide. This area was determined by the embroidery machine used in this study, which had an embroidery area of 40 mm by 100 mm. After several iterations, the following dimensions for each parameter were found: $C_L = 10$ mm, $C_W = 1$ mm, $G_S = 5.20$ mm, $U_W = 14$ mm, $U_L = 16$ mm, and $L_G = 60$ mm. Additionally, dimensions of the portions of the Kirigami design that had no cuts were set to 25 mm by 1.5 mm. With these dimensions, the total length of the Kirigami design was of 90 mm.

5.2.2 Sensor Fabrication

Following the steps above, the sensors used in this study were fabricated to work as resistive embroidered sensors. When embroidering a conductive material, which is typically a conductive thread, onto a fabric substrate, it is possible to detect changes in the resistance of the conductive thread when the fabric substrate is under strain or external forces. This happens because when the fabric is stretched, it causes the conductive thread to bundle up together, reducing the conductive base resistance of the conductive material due to an increased number of contact points between the conductive thread itself. It is important to note that the bundling of the conductive thread is only possible when the embroidered pattern is able to show signs of deformation without getting damaged, which in this study is achieved thanks to the Kirigami pattern used.

Knowing the working principle of embroidered resistive sensors, three sensor samples were created using the procedure highlighted in [66]. First, sensors were designed in SolidWorks 2021 (Dassault Systèmes, SolidWorks Corporation, Waltham, MA, USA) to achieve the specific geometry of the pattern used (Figure 5.2a). Then, the computer-aided design (CAD) model of the sensor

was exported to a digitizing software in the form of a drawing exchange format (DXF) file. The digitizing software used was Inkscape (Inkscape Project, Version 1.3) with the Inkstitch extension. This software converted the CAD model of the sensor into a specific format that could be read by an embroidering machine. Specifically, the sensor models were converted into an embroidery pattern that contained information regarding the row spacing between stitches (stitch density), the length of the stitches, the needle paths followed by the embroidery machine, and the areas of the sensor where the conductive and non-conductive thread were used (Figure 5.2b).

Once the sensors were digitized, they were embroidered onto a 70%/30% polyester/rubber knitted fabric using a Janome Memorycraft 15000 embroidery machine. To support the fabric during the embroidery process, two layers of tear-away stabilizer were used, as this has been proven to be useful to provide good stabilization to the stretchable fabric substrate used [66]. During the embroidery process, each sensor was embroidered in three different parts. The first part, known as the underlay, was created by embroidering a non-conductive thread onto the fabric. This served to secure the fabric to the stabilizer and to work as the main frame of the sensor. Then, a Maderia HC-40 silver-plated conductive thread was embroidered on top of the underlay. This conductive thread was strategically placed in the middle portion of the sensor as in a Kirigami design this region deforms without too much stress due to hinging when axial forces are applied [115].

After embroidering the conductive thread, the embroidery process was repeated to cover the remaining areas of the underlay region with non-conductive thread. Once the embroidery process finished, the tear-away stabilizer was removed from the embroidered sensors, and the openings of the Kirigami pattern were manually cut with small scissors. Finally, a pair of wires were attached to each end of the sensors using grommets (Figure 5.2d).

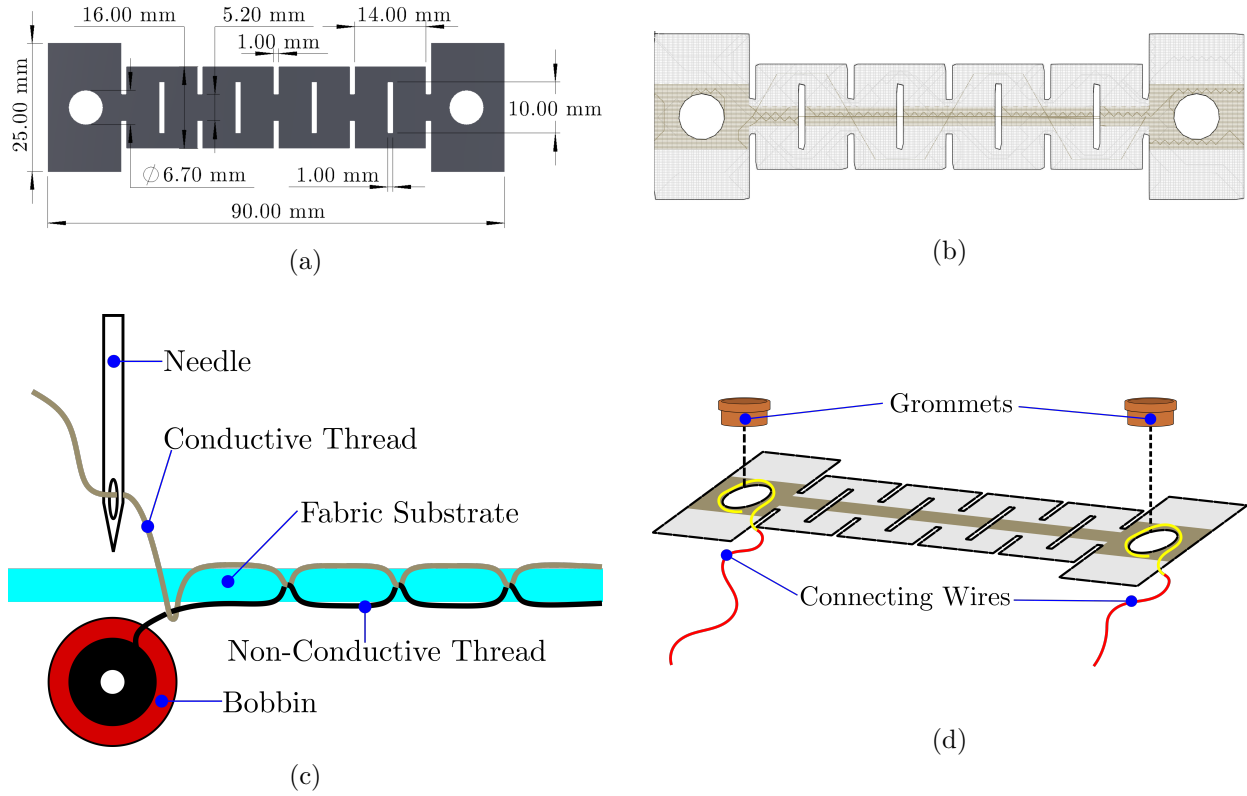


Figure 5.2: Fabrication process of the embroidered sensors. (a) A computer-aided design (CAD) model of the sensor is created to achieve the desired geometry. (b) A digitized version of the CAD model of the embroidered area is created with specific instructions that are read by an embroidery machine. (c) After digitizing the embroidered sensor, it undergoes the embroidery process. The conductive thread is used as the upper thread, whereas a non-conductive thread is used as the bobbin thread. (d) Wires are attached to the embroidered sensor using grommets.

With this procedure, the three sensor samples manufactured resulted in the following base resistances: Sensor S1, with a base resistance of 95Ω ; Sensor S2, with a base resistance of 104.7Ω ; and Sensor S3, with a base resistance of 109.2Ω . The differences in the base resistance values between the three sensor samples were due to an inconsistent resistance value alongside the silver-plated conductive thread, as indicated by the manufacturer.

5.2.3 Sensor Characterization

After embroidering the sensor samples, it was necessary to test them to observe the maximum amount of displacement that they could achieve when they were subjected to stretching forces.

However, it was important to not damage the three sensor samples by subjecting them to forces that would make them go past their elastic region. Therefore, this analysis was performed on a fourth sensor that was embroidered with the same characteristics as the three sensor samples presented in the previous section. To perform the strain–stress analysis, the dummy sensor was fixed to the strain apparatus shown in Figure 5.3a. This apparatus consisted of a fixed buckle piece and a secondary sliding buckle piece mounted on two parallel rails. This secondary piece had a stainless steel cable attached to one end that passed through a pulley and connected to a hook with weights. When the dummy sensor was placed on the sliding buckle, it was stretched by increasing the weights on the hook. On each weight increment, the total length of the sensor was measured. This process was repeated until the dummy sensor showed signs of deformation, which corresponded to the deflection point shown in Figure 5.3b. The data displayed in Figure 5.3b also shows that the sensor behaved linearly up to 16.4 mm of displacement. A line of best fit was applied to this linear region to obtain the stiffness constant of the sensor, which had a value of 1693.04 N/m.

Unfortunately, being able to stretch up to 16 mm is not sufficient for force sensing applications involving joint motions. This is because larger displacements would be required to establish a relationship between the angular displacement of most joints and the linear displacement of the sensor. Therefore, the small displacement that could be achieved by the embroidered force sensors was fixed by attaching them to a strain compensation mechanism made of three elastic bands arranged in series and parallel (Figure 5.4a). This mechanism controlled the rate of displacement of the sensors by reducing the overall stiffness of the whole mechanism.

The working principle of this mechanism can be described as follows. The first elastic band (EB1) of 60 mm long is placed in parallel with the embroidered sensor (Figure 5.4b) to aid the embroidered sensor to recover after being stretched. Then, assuming that the parallel arrangement of EB1 and the embroidered sensor acted as a spring with a stiffness greater than the sensor itself, a second and third elastic bands (EB2 and EB3, respectively) of 90 mm long were placed in series with EB1 and the embroidered sensor to help reduce the overall stiffness of the whole mechanism. The rationale behind this arrangement of series and parallel elements is based on the fact that the force required to displace EB1 and the embroidered sensor is the same as the force required to

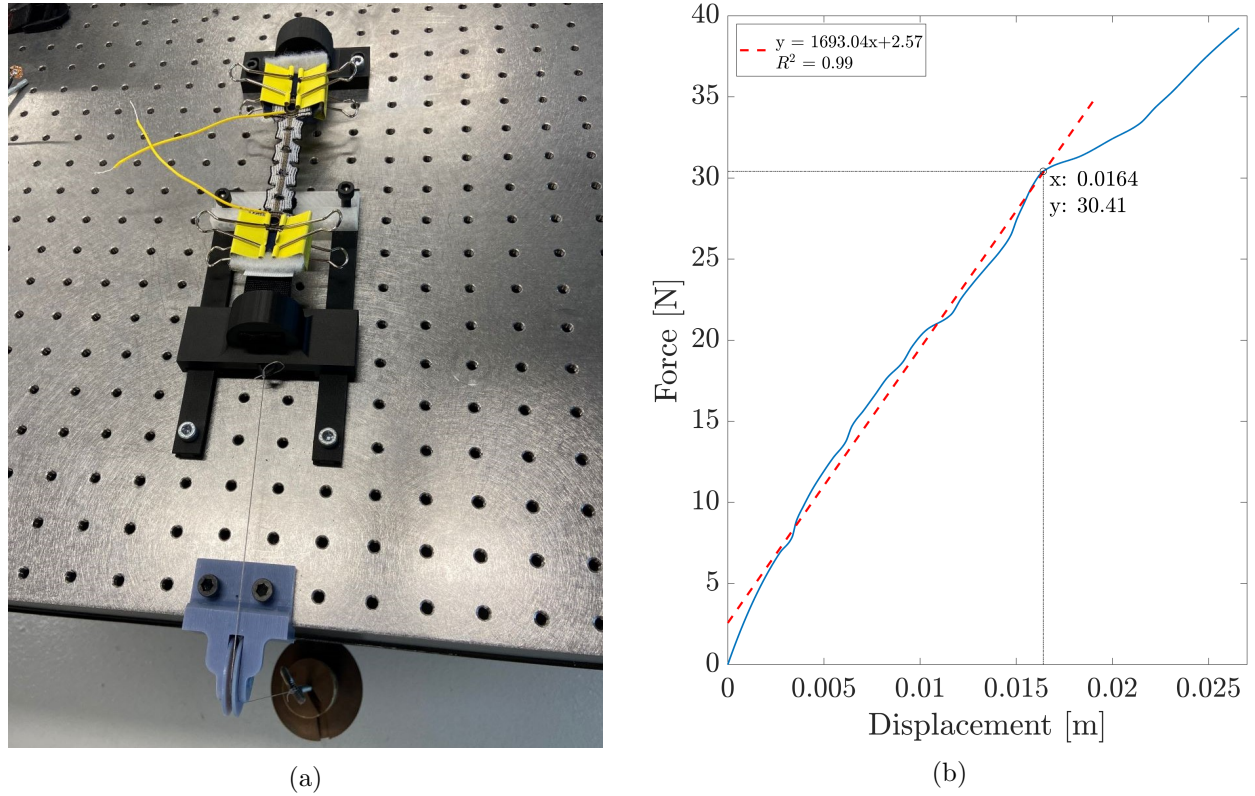


Figure 5.3: (a) Testing of the dummy embroidered sensor to find its maximum displacement. The sensor was horizontally stretched by placing it on a strain apparatus with weights attached to one of its ends. On each successive weight increase, the total displacement of the sensor was measured. (b) Force vs. displacement curve of the dummy embroidered sensor. The intersection of the dotted lines represents the maximum force required to stretch the sensor up to 16.4 mm.

stretch EB2 and EB3. Assuming that the stiffness coefficient of EB2 in parallel with EB3 is lower than the stiffness coefficient of EB1 in parallel with the embroidered sensor, then EB2 and EB3 will stretch further before EB1 and the embroidered sensor can reach a maximum displacement.

The relationship between EB2 and EB3, and EB1 and the embroidered sensor can also be derived from the Duffing equation, which describes the dynamics of nonlinear oscillators that includes both linear and nonlinear stiffness coefficients, and is given as follows [128]:

$$F = kx + \beta kx^3, \quad (5.1)$$

where F is the resulting force, k represents the stiffness coefficient, x is the resulting displacement,

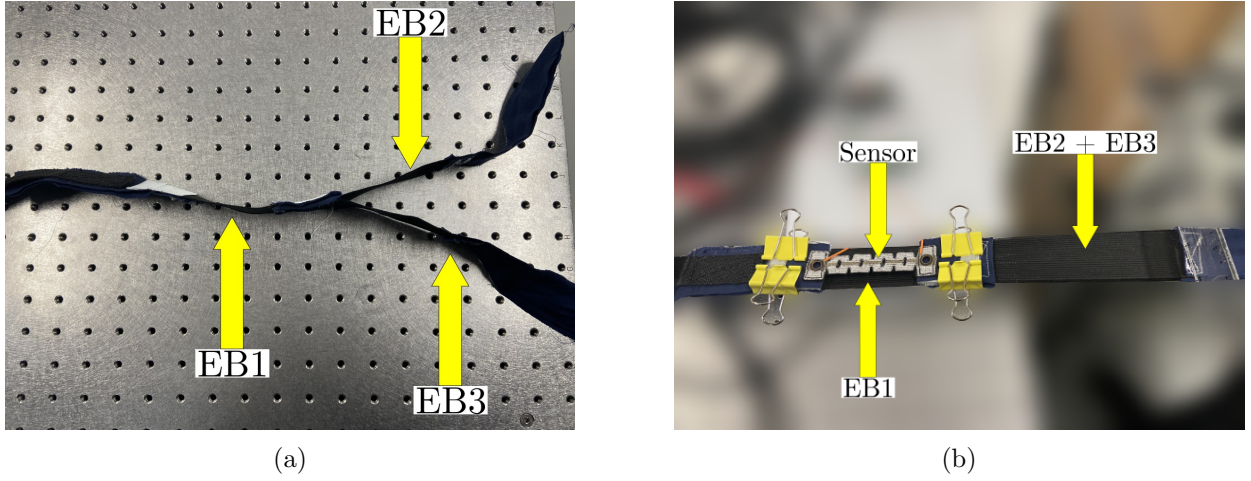


Figure 5.4: Strain compensation mechanism. (a) The mechanism is formed of three elastic bands (EB1–EB3) that control the rate of extension of the embroidered sensor. (b) The embroidered sensor is attached in parallel to EB1 using velcro hooks and butterfly clips.

and β is a constant that contributes to the nonlinear stiffness component. Since elastic bands tend to get stiffer the more they get stretched due to crystallization of its rubber polymers, β in Equation (5.1) will always be greater than zero [128].

Denoting the stiffness of the parallel arrangement between EB1 and the embroidered sensor as k_1 , and the stiffness of the parallel arrangement between EB2 and EB3 as k_2 , and considering that the force applied to k_1 is the same as the force applied to k_2 , the following relationship can be derived from Equation (5.1):

$$\frac{x_1 + \beta_1 \cdot x_1^3}{x_2 + \beta_2 \cdot x_2^3} = \frac{k_2}{k_1}, \quad (5.2)$$

where x_1 and x_2 represent the total displacement of the parallel arrangement between EB1 and the embroidered sensor, and the total displacement of the parallel arrangement between EB2 and EB3, respectively.

Knowing that the working range of the embroidered sensor while attached to the strain compensation mechanism is given by the strain applied to EB2 and EB3, x_2 in Equation (5.2) was set to at least 50% of the total length of EB2 and EB3. This total displacement was set to match other strain sensors such as the ones presented in [47, 51]. Furthermore, because the embroidered

sensor and the elastic bands were made of the same material, it was assumed that β_1 and β_2 were equal. With this information, the left side of Equation (5.2) was estimated to be less than 1, since the denominator term was greater than the numerator, as x_2 was greater than x_1 . This indicated that k_2 needed to be smaller than k_1 to satisfy the equality. However, because the elastic bands behave like nonlinear springs, their stiffness were determined empirically.

5.2.4 Experimental Setup

After implementing the strain compensation mechanism, the embroidered sensors were tested on their ability to measure axial forces. To do so, the sensors were attached to the strain compensation mechanism using velcro hooks and butterfly clips. Then, the sensor compensation mechanism was connected to an ATI Force/Torque sensor (Gamma model, ATI Industrial Automation) as shown in Figure 5.5. This force sensor was selected due to its ability to sense forces and torques in all planes and also, to serve as the ground truth when testing the embroidered force sensor. To prevent slippages that would cause erroneous measurements, the strain compensation mechanism was firmly secured to the ATI sensor using a non-slip webbing strap and a ladder lock buckle.

During the experiments, forces were applied on the z-direction of the ATI force sensor, as it was the axis with the largest resolution according to the sensor specifications. Data received from the ATI force sensor were collected by a 16-bit data acquisition (DAQ) system (USB-6210, National Instruments) at a sample rate of 1 kHz. On the other hand, data from the embroidered sensor were collected by a custom system. This acquisition system consisted of a current driven Wheatstone bridge in a quarter bridge configuration, an amplification stage that amplified the output of the Wheatstone bridge by 100 times, and a 12-bit analog to digital converter that sampled the embroidered sensor data at 1 kHz. To compensate for any resistor imbalances on the legs of the Wheatstone bridge due to unmatched resistor tolerances, or due to variability introduced when embroidering the sensors, an offset voltage compensation circuit was implemented before the amplification stage of the hardware acquisition interface.

Finally, the custom hardware interface was connected to an ESP32 microcontroller that was in charge of driving the offset voltage compensation circuit, and to send the embroidered sensor data serially to a computer running a custom-made software. This software was created in Python, and

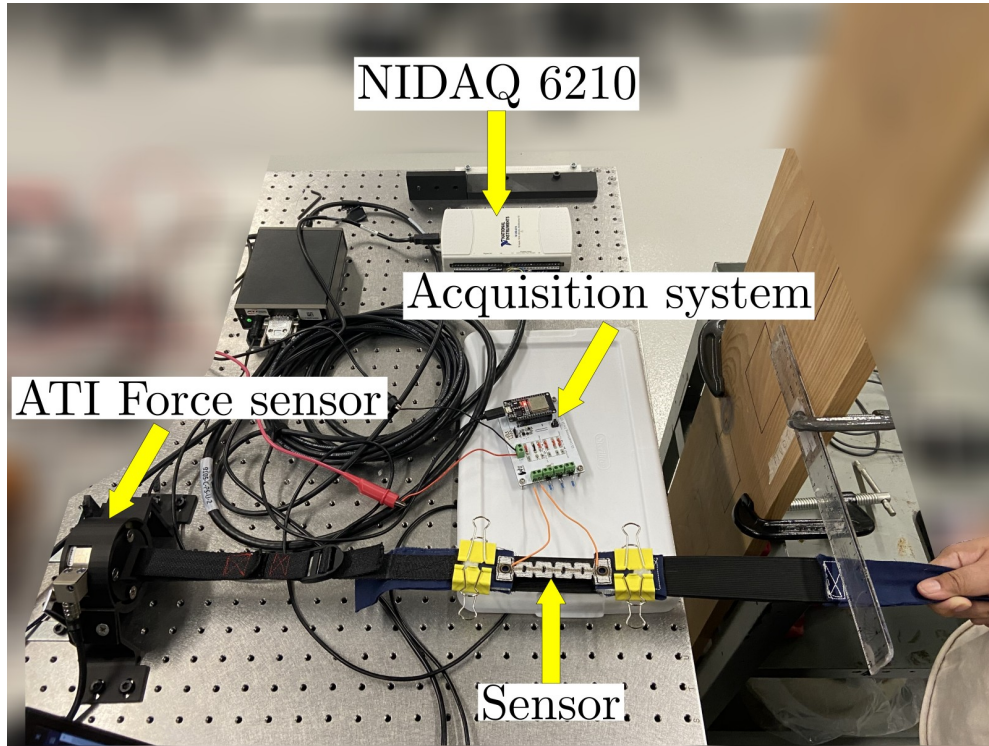


Figure 5.5: Testing setup used for data collection of the embroidered sensor. During the experiments, the embroidered sensor was attached to a strain compensation mechanism. This mechanism was connected to an industrial force sensor that served as ground truth. Data from the force sensor were collected by a data acquisition system (DAQ) at a sample rate of 1 kHz, and data from the embroidered sensor were collected by a custom-made acquisition system at 1 kHz.

served to gather the data collected from the ATI force sensor through the DAQ system, and data collected from the embroidered sensors through the ESP32.

5.2.5 Dynamic Motion Tests

With the experimental setup ready, each sensor was subjected to repeated stretching motions at varying speeds in order to assess their ability to sense forces under dynamic conditions. For this purpose, EB2 and EB3 of the strain compensation mechanism were manually stretched and unstretched for 80 seconds using three different speed profiles: slow speed (30 bpm), medium speed (60 bpm), and fast speed (90 bpm). During each speed profile, every beat corresponded to a state where EB2 and EB3 were either fully stretched or fully unstretched. Furthermore, to track the beats per minute, a digital metronome was used. This process occurred while each embroidered

sensor was attached to the strain compensation mechanism, and repeated three times for each speed profile.

As mentioned in Section 5.2.3, EB2 and EB3 of the strain compensation mechanism were stretched to about 50% of their original length of 90 mm. To prevent overstretching of the elastic bands, a visual guide was placed near the testing setup to indicate that the strain compensation mechanism had reached the total desired displacement.

5.2.6 Signal Processing

After testing the embroidered sensors under dynamic motions, the data collected from the ATI force sensor and from the embroidered sensors during each trial were analyzed offline in MATLAB R2021a (MathWorks, Inc., Natick, MA, USA). First, data from each sensor were smoothed using a window moving average (MAV) filter. For each embroidered sensor and for the ATI force sensor, a window length of 501 samples was used for the MAV filter.

Following smoothing of the data, it was necessary to align the signals collected by the ATI force sensor and the embroidered sensors. This was necessary because even though both groups of sensors started collecting data at the same time, there was a small delay between the arrival times of the signals at the computer running the custom-made acquisition software mentioned in Section 5.2.4. Therefore, data alignment was done using the following procedure. First data from both the ATI force sensor and the embroidered sensors were normalized using the z-score normalization. This allowed data from both sensor modalities to have the same signal amplitudes. After normalization, data from the embroidered sensors were inverted, as in contrast to the data from the ATI force sensor, the output of the embroidered sensors showed a decreasing behaviour. Once both sensor modalities had their data sloping in the same direction, they were aligned using the cross-correlation technique.

5.3 Results

Once data from each sensor modality were fully processed, data from the embroidered sensors were analyzed to understand their ability to sense external axial forces under dynamic conditions. Each

sensor was assessed in terms of linearity, sensitivity, hysteresis, and sensor drift.

To find the linearity of the each sensor sample on each speed profile, the average of the data for all of the three repetitions in a speed profile was computed. Then, a line of best fit was applied on the resulting averaged data. This procedure was repeated for all of the three embroidered sensors at each speed profile (Figure 5.6). During the averaging step, data from the first stretching cycle at each repetition on each speed profile was ignored. This was because the first stretching cycle corresponds to a prestretching phase in which the sensors show a random response [51, 89].

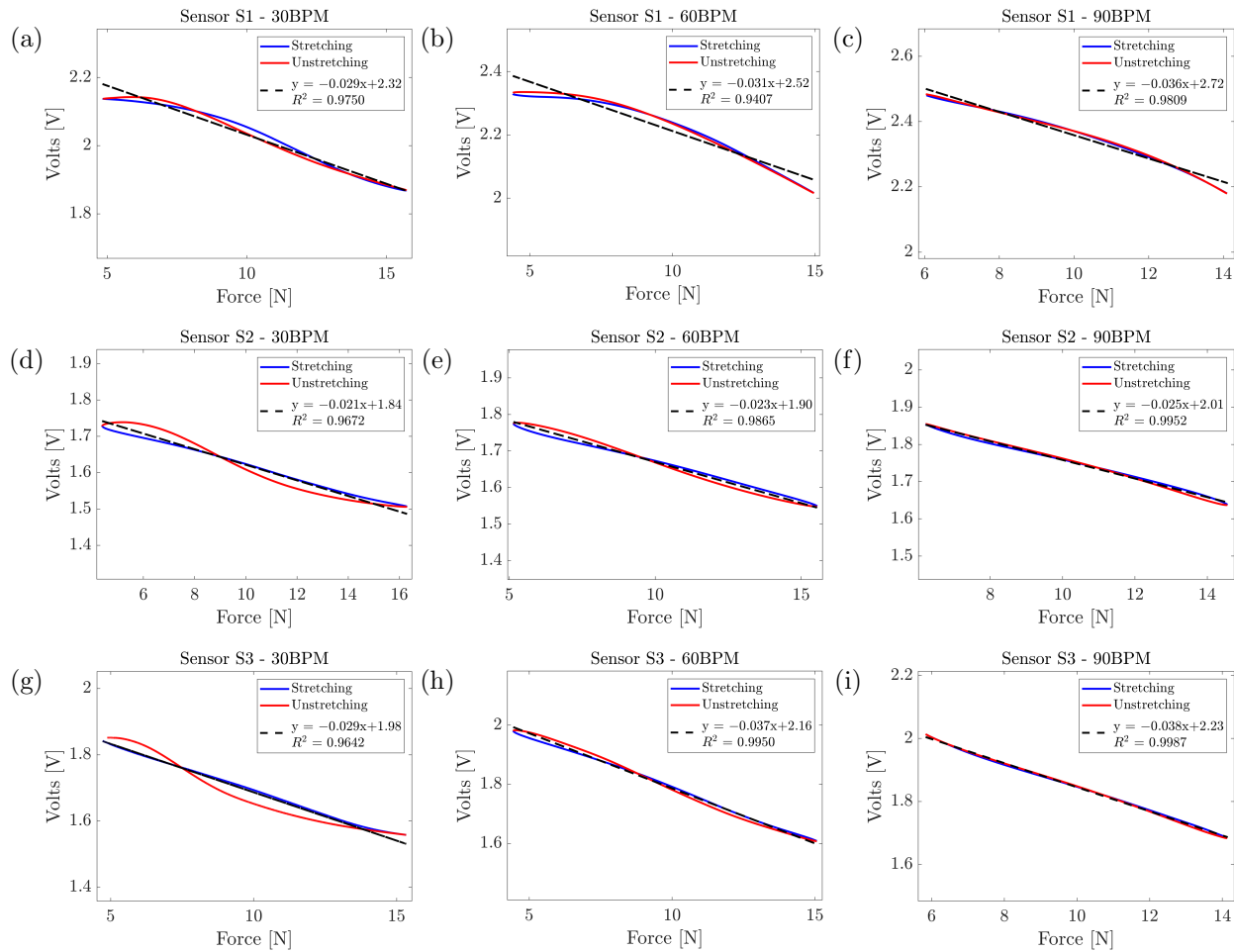


Figure 5.6: Average linear response of each of the three sensor samples at each speed profile. Each row represents a sensor, Sensor S1 at the top, Sensor S2 in the middle, and Sensor S3 at the bottom. Each column represents the speed profile, with 30 bpm on the left, 60 bpm in the middle, and 90 bpm on the right.

From Figure 5.6 it can be observed that all of the sensors had a relatively high linear response,

with Sensor S1 showing the lowest response with an R^2 of 0.9407 when tested at 60 bpm. In contrast, the highest linear response was achieved by Sensor S3 when tested at 90 bpm, with an R^2 value of 0.9987. In fact, Sensor S3 showed the highest linearity response across all of the speed profiles, with an average R^2 value of 0.9860 ± 0.02 . The second high linear response was achieved by Sensor S2, with an average R^2 value of 0.9830 ± 0.01 followed by Sensor S1, with an average R^2 value of 0.9656 ± 0.02 across all of the three speed profiles.

After computing the linearity response of each sensor sample, their sensitivity was estimated from the same line of best fit used for their linearity response. The sensitivity of each sensor is given by the slope of the fitted lines shown in Figure 5.6. It is important to mention that the slope of the lines resulted in a negative value due to the signals showing a decreasing monotonic behaviour, which is why the absolute value of the slope was taken to show the sensitivity of each sensor. The sensitivity of the three sensors ranged from 0.021 V/N to 0.038 V/N, with an average sensitivity of $0.027 \text{ V/N} \pm 0.004 \text{ V/N}$ for all of the three sensors at 30 bpm, an average sensitivity of $0.03 \text{ V/N} \pm 0.007 \text{ V/N}$ at 60 bpm, and an average sensitivity of $0.033 \text{ V/N} \pm 0.007 \text{ V/N}$ for all three sensors at 90 bpm.

The third metric assessed was the hysteresis (H_F) of the sensors, and it was computed as the maximum deviation in force ΔF_h between the stretching and unstretching stages of the sensors at a specific voltage level. The hysteresis was normalized between the maximum (F_{max}) and minimum forces (F_{min}) to account for differences between sensors; and it was computed using the following equation [66]:

$$H_F = \frac{\Delta F_h}{F_{max} - F_{min}} \times 100. \quad (5.3)$$

The hysteresis of the sensors across all speed profiles ranged from 2.23% to 19.09%, with Sensor S1 showing both the maximum and minimum hysteresis percentage between all three sensors. Furthermore, at 30 bpm, an average hysteresis of $15.69\% \pm 2.34\%$ was found between all of the three sensor samples. Similarly, an average hysteresis of $12.05\% \pm 6.47\%$ was found for all of the three sensor samples at 60 bpm. This was followed by an average hysteresis of $3.06\% \pm 1.25\%$ at 90 bpm across all of the three sensor samples. The average hysteresis of all three sensors alongside

the average linearity, and the average sensitivity at 30, 60, and 90 bpm are shown in Tables 5.1 to 5.3, respectively.

Table 5.1: Average performance metrics of each sensor at 30 bpm.

Sensor Name	Linearity (R^2)	Sensitivity (V/N)	Hysteresis (%)
Sensor S1	0.9750	0.029	16.54
Sensor S2	0.9672	0.021	17.48
Sensor S3	0.9642	0.029	13.04
Average	0.9688 ± 0.0056	0.026 ± 0.004	15.69 ± 2.34

Table 5.2: Average performance metrics of each sensor at 60 bpm.

Sensor Name	Linearity (R^2)	Sensitivity (V/N)	Hysteresis (%)
Sensor S1	0.9407	0.031	19.09
Sensor S2	0.9865	0.023	10.69
Sensor S3	0.9950	0.037	6.37
Average	0.9741 ± 0.0292	0.03 ± 0.007	12.05 ± 6.47

Table 5.3: Average performance metrics of each sensor at 90 bpm.

Sensor Name	Linearity (R^2)	Sensitivity (V/N)	Hysteresis (%)
Sensor S1	0.9809	0.036	2.23
Sensor S2	0.9952	0.025	4.50
Sensor S3	0.9987	0.029	2.44
Average	0.9916 ± 0.0094	0.033 ± 0.007	3.06 ± 1.25

The final metric assessed for each sensor sample was their repeatability. This metric refers to the amount of drift each sensor showed under dynamic motions. The drift of each sensor sample is shown in Figure 5.7, where the first and last stretching cycles of each sensor is displayed at the three different speed profiles. From these images, it can be observed that the sensor that drifted

less was Sensor S2, which showed the least drift between all of the three sensor samples when tested at 90 bpm. In contrast, the sensor that showed a more prominent drifting behaviour was Sensor S1, which showed the highest drift when cycled at 60 bpm.

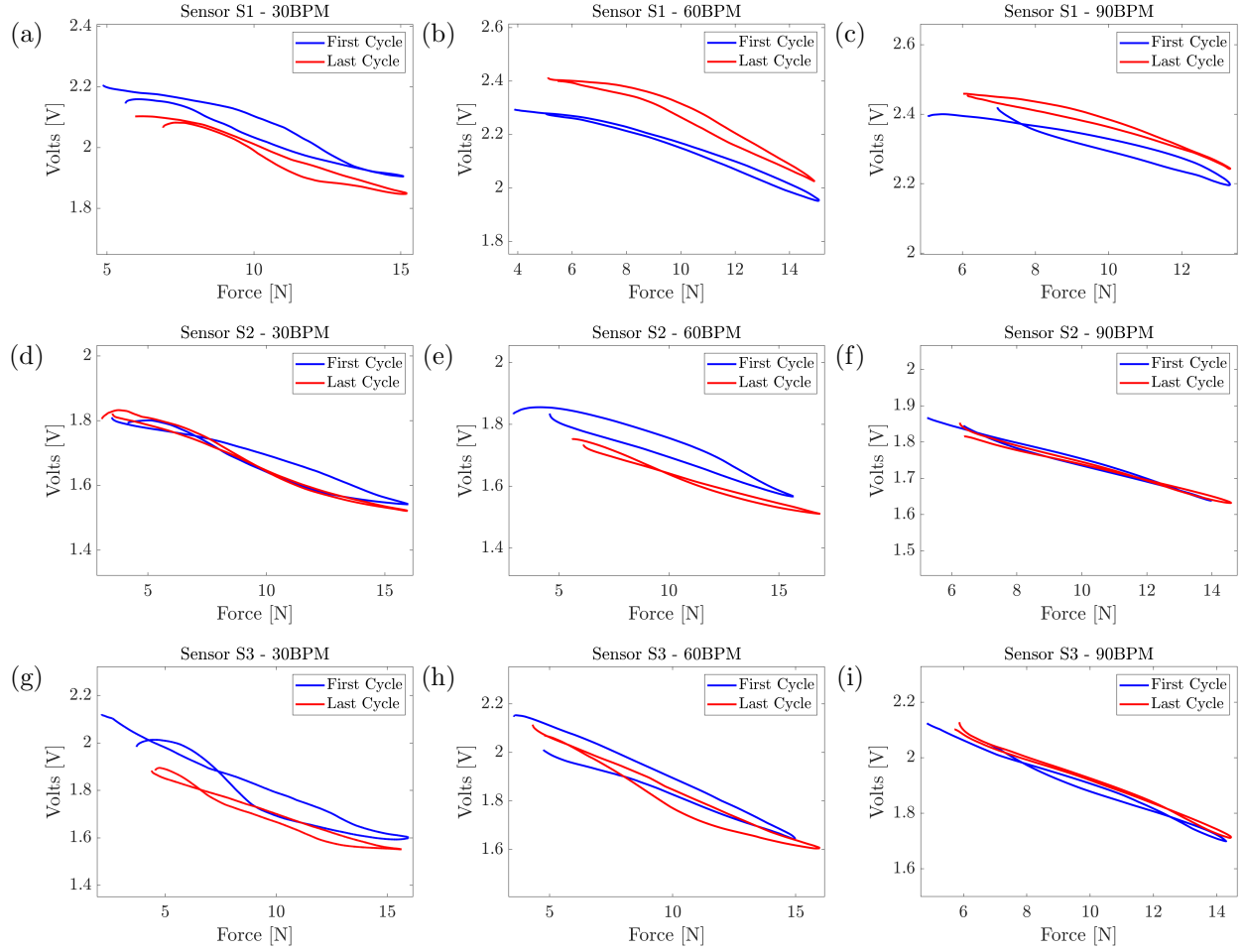


Figure 5.7: Sensors drift over each stretching cycle at the three speed profiles. Each row represents a sensor, Sensor S1 at the top, Sensor S2 in the middle, and Sensor S3 at the bottom. Each column represents the speed profile, with 30 bpm on the left, 60 bpm in the middle, and 90 bpm on the right.

5.4 Discussion

The results of this study show that the Kirigami-based embroidered resistive sensors presented in this study have the potential to be used as a possible alternative to traditional force sensing

applications involving wearable mechatronic devices. This is thanks to their high linearity response, relatively low drift, and low hysteretic behaviour. The high linearity response of the sensors across all of the speed profiles can be attributed to the mechanical response of the Kirigami design. As seen in Figure 5.6, the maximum force applied to the sensors was approximately 16 N. When evaluating this force using the fitted data shown in Figure 5.3b, it can be observed that the sensor response fell within the linear region that follows Hooke's law. However, during the experiments, it was noted that the sensors presented an out-of-plane deformation without significant signs of stretching. This contradicts the mechanical characteristics of a Kirigami pattern, which indicate that the sensor should have been able to easily stretch without the need of higher forces, as an out-plane deformation corresponds to the second stage of deformation of a Kirigami design (Figure 5.1b). A possible explanation of this behaviour is that traditional Kirigami patterns are made of thin laminar sheets such as Kent paper [125, 126], which has a negligible thickness not considered as a design parameter in Kirigami designs. However, for the particular case of the embroidered sensors developed in this study, each one of them had a noticeable thickness of approximately 1 mm, which may have influenced the mechanical response of the Kirigami pattern.

Regarding the hysteresis of the sensor samples, an interesting behaviour was found for all of the sensors across their respective speed profiles. From Tables 5.1 to 5.3, it can be noted that each sensor showed a noticeable reduction in their hysteretic behaviour as the testing speed increased. The exception being Sensor S1, which showed a small increment in hysteresis when increasing the speed from 30 bpm to 60 bpm. However, the hysteretic response of Sensor S1 decreased considerably when the testing speed changed from 60 bpm to 90 bpm. This suggests that the embroidered sensors developed in this study can perform well when used under dynamic conditions in which speed is an important factor to consider. An example of such scenario is when wearable mechatronic devices are used to assess the smoothness of the motion during rehabilitation procedures [129].

Although the hysteresis of each sensor sample was similar to each other at each speed profile, there is some room for improvement. The variability found between each sensor sample is due to irregularities introduced during the embroidering of the sensors and due to the cuts of the Kirigami design, which were created manually. When embroidering the sensors, the conductive thread used

passes through a series of mechanisms in the embroidery machine that put the thread under different tensions. These mechanisms also increase the friction on the surface of the thread, which can cause the conductive layer of the conductive thread to get damaged, resulting in embroidered sensors with different base resistances. Although this issue can be addressed to a certain extent using the offset compensation voltage mentioned in Section 5.2.4, it is hard to completely solve the problem due to the nonlinearities introduced by the circuit itself. On the other hand, the irregularities introduced by creating the cuts of the Kirigami pattern with scissors can be avoided by adopting solutions such as the one presented in [65], where the cuts of the Kirigami pattern were created on a weaved fabric through laser cutting.

As for the repeatability of the sensors, it was observed that although the sensors deviated from their initial response on each consecutive stretching cycle (Figure 5.7), the drifting behaviour was not consistent between the sensor samples. In this sense, some sensors drifted towards higher voltage outputs (Figures 5.7b, 5.7c and 5.7i) while others drifted in the opposite direction (Figures 5.7a and 5.7d to 5.7h). Similar to the hysteresis, the drifting behaviour of the sensors can be attributed to the variability introduced by the manufacturing process of the sensors. Furthermore, in sensor applications where the manufacturing process is based on stitching or embroidering, stitch deformation and recovery play a major role on the sensor drift [130]. As explained before, when the embroidered sensors are put under tension, the conductive thread that forms them tends to bundle up together. When the tension is released, the bundled fibres will try to go to their original position. However, because of the previous tension applied, some stitches may present signs of deformation, which will cause fewer fibres to bundle together on successive stretching cycles, as these fibres will become loose due to the deformed stitches. Therefore, to address this issue, it would be beneficial to implement linearity algorithms that could track the drifting behaviour while also accounting for stitch deformation. One algorithm that could be particularly useful in this scenario would be the one proposed by Kim *et al.* [91], which is the time-delay artificial neural network. This algorithm is useful as it allows drift compensation by making use of transfer learning to account for real time variations of the sensor samples.

With respect to the sensitivity of the sensor samples, it is important to mention that the low sensitivity score obtained by the sensors samples is not a factor that could potentially hinder

the usability of the sensors in wearable mechatronic applications. This is thanks to the strain compensation mechanism that allowed for an increased working range of the sensor samples. In this sense, it would be possible to increase or decrease the rate of displacement of the embroidered sensor by selecting the proper arrangement of spring materials used for the strain compensation mechanism. In this study, the three elastic bands used as the spring materials proved to be enough to achieve a 50% working range. It should be noted though, that this working range was calculated with respect to the length and displacement of the elastic bands EB2 and EB3 of the strain compensation mechanism. Furthermore, to achieve a variable working range that fits the application in which the embroidery sensor is being used, it would be necessary to derive the spring coefficients of the strain compensation mechanism. As mentioned in Section 5.2.3, the spring coefficients of the strain compensation mechanism were found empirically using Equation (5.1) as a starting point. However, other models that represent the elastic bands as viscoelastic systems [131] may provide a better approach to finding their nonlinear spring coefficients.

5.5 Conclusions and Future Work

In this study, a novel embroidered resistive sensor capable of sensing forces under dynamic conditions was presented. The principal characteristic of this type of sensor is that it is based on a Kirigami design that allows the distribution of forces across the embroidered sensor without causing structural damages to the conductive thread used. Furthermore, the Kirigami design allowed the embroidered sensor to achieve stretchable characteristics, which is something difficult to achieve in embroidered structures. Also, the sensors presented in this study showed a low hysteretic behaviour, high linearity, relatively good repeatability, and good sensitivity thanks to the strain compensation mechanism implemented.

Although the results presented in this study show that the Kirigami-based embroidered sensors have the potential to be used in applications involving wearable mechatronic devices, there is room for improvement. For instance, it was found that the thickness of the resulting sensors affected the mechanical response of the Kirigami design. Therefore, future work should aim towards the characterization of the Kirigami pattern that accounts for the material thickness as part of the

parameters used during the Kirigami shape design process. Another potential future direction would be to assess the performance of the sensors by testing different combinations of the design parameters of the Kirigami pattern. By doing so, it may be possible to address some of the issues associated with the repeatability and sensitivity of the embroidered sensors.

Overall, the sensors presented in this study pave the way for potential solutions in the field of rehabilitation robotics in which the testing conditions deviate from lab constrained environments. By enhancing the performance of this type of sensors, it would be possible to move forward in the direction of physical rehabilitation outside of a clinic environment.

Chapter 6

Concluding Remarks

Wearable mechatronic devices have the potential to enhance the rehabilitation outcomes of stroke survivors and individuals affected by MSD. Furthermore, the ability of these devices to provide a more personalized therapy, as well as their portability capabilities, make wearable mechatronic devices great candidates for improving the quality of life of MSD and stroke survivors outside a clinical setting. However, numerous disadvantages such as bulkiness, high manufacturing costs, and the natural rigidity hinder the potential of wearable mechatronic devices to be widely adopted in a clinical setting, let alone as devices used for in-home rehabilitation. This is the reason why soft wearable mechatronic devices have emerged as a potential solution, as these devices are inherently compliant and can easily conform to the human body. One of the key factors to achieve such compliance is the integration of soft sensing elements onto the soft wearable devices. Unlike conventional rigid sensors, soft sensors have the advantage of being lightweight and comfortable, and have the ability to maintain functionality even during dynamic movements.

Advancements in technology have allowed the development of different types of soft sensors, with motion and force sensors being the most commonly used in soft wearable mechatronic devices due to their ease of integration onto these systems. Previous studies showed that these sensing modalities could be achieved by using polymer-based strain sensors. However, these solutions were not optimal, as polymer-based strain sensors lack permeability, which makes them uncomfortable the longer they are used. This is the reason why motion and force sensing have been slowly transitioning to textile-based solutions as they are more comfortable to wear and they have the

distinctive characteristic of potentially being integrated onto every day garments. Among all of these solutions, the comfort of embroidered sensors, as well as their rapid prototyping characteristics makes them an interesting solution for force and motion sensing applications. Therefore, the purpose of this thesis was to expand on the use of embroidered textile sensors to strain sensing applications. To do so, several studies were conducted to assess the feasibility of embroidered sensors as potential substitutes to polymer-based strain sensors.

The first study was performed with the goal of providing a framework for fabricating embroidered textile strain sensors. One of the steps included within this framework was the use of a CAD software to create a model of the sensor with desired dimensions. The next step was the digitization of the CAD model before embroidering the sensor. Some key parameters required to provide the embroidered sensor with stretchable capabilities were identified. Finally, several embroidered strain sensors were fabricated using this framework in order to assess its effectiveness. These sensors were tested in terms of linearity, sensitivity, hysteresis, repeatability, and working range. Although not perfect, these sensors showed similar performance to other textile-based sensors used in the literature. In addition, the ease of manufacturability of the sensors, and the customization capabilities introduced during the digitization of the sensors, showed the effectiveness of the proposed framework.

The second project completed as part of this thesis focused on exploring the effects of using different patterns to enhance the strain sensing capabilities of the embroidered sensors. To this end, it was decided to evaluate the performance of the embroidered textile strain sensor using a honeycomb pattern. The reason of using this pattern was twofold. First, the honeycomb pattern added stretchability to the sensor without compromising the integrity of the embroidery stitches. Second, the honeycomb pattern served to protect the conductive thread from getting damaged due to the strain forces applied. After many iterations, several sensors were embroidered using a rectangular honeycomb pattern and their performance were assessed in terms of linearity, sensitivity, hysteresis, and repeatability.

With the framework for fabricating embroidered textile strain sensor established, and the assessment of the performance of embroidered textile strain sensors using honeycomb patterns, the final project of this thesis focused on the use of embroidered strain sensors as stretchable force

sensors under dynamic motions. As a result, several sensors were fabricated using the framework presented in the first project. Also, instead of a honeycomb pattern a Kirigami design was used to provide stretchability and robustness to the sensors. To evaluate the ability of these sensor to detect forces, the sensors were tested under different speed profiles.

To summarize and to highlight the advantages and areas of improvement, the performance of each of the sensors developed in this thesis is presented in Table 6.1. It is important to note that even though the gauge factor of the sensors created using a honeycomb and a Kirigami design did not achieve high values, these sensors still have the potential to be used in upper-limb rehabilitation. As discussed by Jansen [47], applications involving motion tracking of upper limbs do not require high gauge factors, as long as the data collected by the sensors show low noise levels, which is the case for the sensors developed in this research work.

Table 6.1: Summary of the performance metrics of the sensors developed in this thesis.

Sensor	Thread	Linearity (R^2)	Gauge Factor	Working Range (%)	Hysteresis (%)	Notes
1st Prototype	Stainless Steel	0.77 ± 0.07	1.88 ± 0.51	26	8.54 ± 2.66	The sensors show a drifting behaviour. Also, sensors show a reduction on the working range due to tension issues.
Honeycomb	Silver-Plated	0.80 ± 0.03	0.24 ± 0.06	55	36.85 ± 4.95	Sensors require the use of a strain divider system to increase their displacement. Sensors are robust to stitch deformation. Sensors show low drifting behaviour. The high hysteresis may be caused due to the nonlinearities of the strain divider system.
Kirigami	Silver-Plated	0.9782 ± 0.0119	0.03 V/N $\pm 0.004 \text{ V/N}$	N/A	10.27 ± 6.5	Sensors require the use of a strain divider system to increase their displacement. Sensors are robust to stitch deformation. Sensors show low drifting behaviour. Sensors tend to decrease their hysteresis when stretched at high speed profiles.

6.1 Contributions

The work presented in this thesis showed that embroidered textile sensors have the potential to be used as an alternative solution to polymer-based soft strain sensors. This was achieved through an understanding of the mechanical characteristics of embroidered patterns, such as honeycomb and Kirigami designs. Furthermore, the in depth analysis of the electrical mechanisms that govern this type of sensors resulted in an embroidered sensor capable of detecting forces under dynamic conditions. Although there is room for improvement, this work provides a stepping stone for potential applications involving textile-based sensors and soft wearable mechatronic devices. The specific contributions of this work are as follows:

- Proposed a framework for the development of embroidered textile strain sensors. Previous work regarding the development of textile strain sensors [51–54] lacked information regarding the steps required to fabricate embroidered strain sensors. This is mainly due to the majority of these studies focusing on the implementation of stitched-based textile strain sensors, which in comparison to embroidered-based strain sensors, have fewer design parameters that affect their stretchability. One of the main disadvantages of stitched-based strain sensors is the requirement of specialized sewing machines that are able to create some of the stitches used in the literature. In contrast, embroidered strain sensors can be manufactured using commercial embroidery machines. Nevertheless, there was a gap in terms of information about the embroidery design parameters that needed to be addressed to achieve a stretchable embroidered structure. The proposed framework showed that strain characteristics could be achieved on embroidered sensors, and that these sensors performed similar to stitch-based sensors.
- Presented the effects of honeycomb structures on the performance of resistive embroidered textile strain sensors. Embroidery-based strain sensors have the disadvantage of suffering from stitch deformations in the presence of axial forces required to stretch them. The effect of these deformations causes tension issues on the embroidery structure that severely impacts the ability of strain sensors to properly track motion, as the output of the sensors show a drifting behaviour. Furthermore, stretching forces can severely damage the conductive thread used during the embroidery process, which is also a contributing factor to the drifting behaviour observed in embroidered sensors. To overcome these issues, the effects of using a honeycomb pattern as an embroidery design were explored. The results of this study showed that embroidered sensors created using the honeycomb pattern added robustness to the conductive thread as observed in the constant working range and relative low drifting behaviour throughout all testing cycles.
- Successfully demonstrated the feasibility of the application of embroidered strain sensors as force sensing elements under dynamic conditions. In terms of soft force sensing applications, there is a limited number of solutions in the literature, as most force sensors are typically

relegated to pressure sensing applications. Furthermore, the lack of information regarding the performance of embroidered force sensors in the presence of dynamic motions hinders their potential integration in upper-limb soft wearable mechatronic devices. To bridge this gap, this work explored the performance of embroidered sensors under different speed profiles. To provide robustness and stretchability capabilities to the sensor, a Kirigami pattern was used. The results of this study showed that embroidered strain sensors can effectively be used as force sensing elements. Furthermore, the use of the Kirigami pattern resulted in a force sensor whose output was completely linear.

- Implemented a strain compensation mechanism for both strain and force sensors. Although the Kirigami design and the honeycomb pattern were used to provide stretchability to the embroidered strain sensors, it was noted that the amount of displacement they could achieve was limited. This is the reason why a set of elastic bands connected in series and in parallel to the sensors were used. Although this concept is not new, to the authors knowledge, this is the first time the elements of the strain compensation mechanism were considered as nonlinear springs.

6.2 Future Work

While the work presented in this thesis show that embroidered textile strain sensors have great potential as an alternative solution to polymer-based sensors, there are areas of future work that need to be pursued in order to address some of the limitations discussed for this type of textile-based sensors. These areas are summarized as follows:

- As it has been discussed, embroidered textile strain sensors show a nonlinear behaviour when used for motion sensing. Therefore, it is important to implement linearization techniques before these sensors can be fully integrated into wearable mechatronic systems. Some of these techniques include the implementation of deep learning algorithms that can learn and adapt to these nonlinearities, and compensate for them in real time.
- The embroidered textile strain sensors need to be tested under longer stretching and un-

stretching cycles. With the exception of the drifting behaviour, it is unlikely that the sensors presented in Chapters 4 and 5 will perform differently under prolonged stretching and un-stretching cycles. However, increasing the number of cycles used for testing the sensors would provide information regarding fatigue and breaking point, which are two important characteristics to consider, especially if the sensors will be used for prolonged periods of time.

- Similarly, it is important to test the embroidered strain sensors under different temperature and humidity conditions. Given that the sensors presented in Chapters 3 to 5 behave like resistive sensors, they are prone to be affected by changes in temperature and in the relative humidity. Furthermore, when the embroidered sensors are attached to the user, body temperature and sweat are also factors that can affect their performance. Therefore, it would be important to implement sensor fusion techniques that can track changes in the response of the embroidered sensors due to temperature and humidity, and use the data collected to compensate for these disturbances.
- Although the sensors presented in Chapters 4 and 5 were able to stretch in the presence of axial forces, the amount of displacement they could achieve was very limited. This is the reason why a strain compensation mechanism was implemented to facilitate the stretchability of the sensors. Therefore, it is important that future work focuses on solutions to increase the amount of displacement that these sensors can achieve without compromising their performance. One possible solution would be testing different combinations of the design parameters of the honeycomb and Kirigami patterns to find the right balance between good performance and stretchability.
- Finally, even though the sensors presented in this thesis were soft sensors, their conditioning circuit and acquisition hardware still used hard components. With the current technology, it is hard to avoid this issue, however, several directions can be followed to minimize the amount of hard components used to collect data from the embroidered textile strain sensors. One of these solutions involve using compact electronic elements that cover a minimum surface area compared to the soft sensors.

Although addressing all of these limitations will not suddenly allow upper-limb wearable mecha-

tronic systems to be fully adopted in a clinical setting, they will set the basis for future directions required to ultimately achieve this goal. Furthermore, with the advances in the field of e-textiles, it is possible that new alternatives for textile-based strain sensing will be proposed. Nonetheless, it is expected that the contributions of this work will serve as a stepping stone towards the improvement of the quality of life of MSD and stroke patients.

References

- [1] World Health Organization, “Musculoskeletal health,” 2022, [Online] Available: <https://www.who.int/news-room/fact-sheets/detail/musculoskeletal-conditions>.
- [2] W. Johnson, O. Onuma, *et al.*, “Stroke: a global response is needed,” *Bulletin of the World Health Organization*, vol. 94, no. 9, p. 634, 2016.
- [3] X. Chen, L. Gong, *et al.*, “A wearable hand rehabilitation system with soft gloves,” *IEEE Transactions on Industrial Informatics*, vol. 17, no. 2, pp. 943–952, 2020.
- [4] M. H. Rahman, M. Saad, *et al.*, “Nonlinear sliding mode control implementation of an upper limb exoskeleton robot to provide passive rehabilitation therapy,” in *International Conference on Intelligent Robotics and Applications*. Montreal, QC, Canada: Springer, October 3–5, 2012, pp. 52–62.
- [5] T. Proietti, V. Crocher, *et al.*, “Upper-limb robotic exoskeletons for neurorehabilitation: a review on control strategies,” *IEEE Reviews in Biomedical Engineering*, vol. 9, pp. 4–14, 2016.
- [6] E. Bardi, M. Gandolla, *et al.*, “Upper limb soft robotic wearable devices: a systematic review,” *Journal of NeuroEngineering and Rehabilitation*, vol. 19, no. 1, pp. 1–17, 2022.
- [7] A. F. Pérez Vidal, J. Y. Rumbo Morales, *et al.*, “Soft exoskeletons: development, requirements, and challenges of the last decade,” *Actuators*, vol. 10, no. 7, p. 166, 2021.
- [8] M. Tiboni, A. Borboni, *et al.*, “Sensors and actuation technologies in exoskeletons: a review,” *Sensors*, vol. 22, no. 3, p. 884, 2022.
- [9] T. Desplenter, Y. Zhou, *et al.*, “Rehabilitative and assistive wearable mechatronic upper-limb devices: a review,” *Journal of Rehabilitation and Assistive Technologies Engineering*, vol. 7, p. 2055668320917870, 2020.
- [10] J. G. Colli-Alfaro, A. Ibrahim, and A. L. Trejos, “Design of user-independent hand gesture recognition using multilayer perceptron networks and sensor fusion techniques,” in *IEEE 16th International Conference on Rehabilitation Robotics*, Toronto, Ontario, Canada, June 24–28, 2019, pp. 1103–1108.
- [11] M. Georgi, C. Amma, and T. Schultz, “Fusion and comparison of IMU and EMG signals for wearable gesture recognition,” in *International Joint Conference on Biomedical Engineering Systems and Technologies*, Lisbon, Portugal, January 12–15, 2015, pp. 308–323.

- [12] M. S. Totty and E. Wade, "Muscle activation and inertial motion data for noninvasive classification of activities of daily living," *IEEE Transactions on Biomedical Engineering*, vol. 65, no. 5, pp. 1069–1076, 2017.
- [13] X. An and G. K. Stylios, "A hybrid textile electrode for electrocardiogram (ECG) measurement and motion tracking," *Materials*, vol. 11, no. 10, p. 1887, 2018.
- [14] C. Xu, J. He, *et al.*, "Towards human motion tracking: multi-sensory IMU/TOA fusion method and fundamental limits," *Electronics*, vol. 8, no. 2, p. 142, 2019.
- [15] D. Popov, I. Gaponov, and J.-H. Ryu, "Portable exoskeleton glove with soft structure for hand assistance in activities of daily living," *IEEE/ASME Transactions on Mechatronics*, vol. 22, no. 2, pp. 865–875, 2016.
- [16] H. K. Yap, J. H. Lim, *et al.*, "A soft exoskeleton for hand assistive and rehabilitation application using pneumatic actuators with variable stiffness," in *IEEE International Conference on Robotics and Automation (ICRA)*, Seattle, WA, USA, May 26–30, 2015, pp. 4967–4972.
- [17] T. Du Plessis, K. Djouani, and C. Oosthuizen, "A review of active hand exoskeletons for rehabilitation and assistance," *Robotics*, vol. 10, no. 1, p. 40, 2021.
- [18] M. Hamaya, T. Matsubara, *et al.*, "Design of physical user–robot interactions for model identification of soft actuators on exoskeleton robots," *The International Journal of Robotics Research*, vol. 40, no. 1, pp. 397–410, 2021.
- [19] H. Choi, K. Seo, *et al.*, "Compact hip-force sensor for a gait-assistance exoskeleton system," *Sensors*, vol. 18, no. 2, p. 566, 2018.
- [20] M. A. U. Khalid and S. H. Chang, "Flexible strain sensors for wearable applications fabricated using novel functional nanocomposites: a review," *Composite Structures*, vol. 284, p. 115214, 2022.
- [21] S. Ma, J. Tang, *et al.*, "Performance of flexible strain sensors with different transition mechanisms: a review," *IEEE Sensors Journal*, vol. 22, no. 8, pp. 7475–7498, 2022.
- [22] Z. Liu, Y. Zheng, *et al.*, "Highly breathable and stretchable strain sensors with insensitive response to pressure and bending," *Advanced Functional Materials*, vol. 31, no. 14, p. 2007622, 2021.
- [23] N. Paredes-Acuña, N. Berberich, *et al.*, "Tactile-based assistive method to support physical therapy routines in a lightweight upper-limb exoskeleton," *IEEE Transactions on Medical Robotics and Bionics*, vol. 4, no. 3, pp. 541–549, 2022.
- [24] A. Mancisidor, A. Zubizarreta, *et al.*, "Inclusive and seamless control framework for safe robot-mediated therapy for upper limbs rehabilitation," *Mechatronics*, vol. 58, pp. 70–79, 2019.
- [25] S. Dalla Gasperina, L. Roveda, *et al.*, "Review on patient-cooperative control strategies for upper-limb rehabilitation exoskeletons," *Frontiers in Robotics and AI*, vol. 8, p. 745018, 2021.

- [26] Z. Tang, H. Wang, *et al.*, “An upper-limb rehabilitation exoskeleton system controlled by mi recognition model with deep emphasized informative features in a vr scene,” *IEEE Transactions on Neural Systems and Rehabilitation Engineering*, 2023.
- [27] D. Kong, W. Wang, *et al.*, “Flexible control strategy for upper-limb rehabilitation exoskeleton based on virtual spring damper hypothesis,” in *Actuators*, vol. 11, no. 5. MDPI, 2022, p. 138.
- [28] A. Blanco-Ortega, L. Vázquez-Sánchez, *et al.*, “A robust controller for upper limb rehabilitation exoskeleton,” *Applied Sciences*, vol. 12, no. 3, p. 1178, 2022.
- [29] H. Choi, B. B. Kang, *et al.*, “Exo-wrist: A soft tendon-driven wrist-wearable robot with active anchor for dart-throwing motion in hemiplegic patients,” *IEEE Robotics and Automation Letters*, vol. 4, no. 4, pp. 4499–4506, 2019.
- [30] P. Polygerinos, Z. Wang, *et al.*, “Soft robotic glove for combined assistance and at-home rehabilitation,” *Robotics and Autonomous Systems*, vol. 73, pp. 135–143, 2015.
- [31] Y. M. Zhou, C. Hohimer, *et al.*, “Kinematics-based control of an inflatable soft wearable robot for assisting the shoulder of industrial workers,” *IEEE Robotics and Automation Letters*, vol. 6, no. 2, pp. 2155–2162, 2021.
- [32] C. T. O’Neill, N. S. Phipps, *et al.*, “A soft wearable robot for the shoulder: design, characterization, and preliminary testing,” in *International Conference on Rehabilitation Robotics (ICORR)*, London, UK, July 17–20, 2017, pp. 1672–1678.
- [33] S. Das and Y. Kurita, “Forcearm: a wearable pneumatic gel muscle (PGM)-based assistive suit for the upper limb,” *IEEE Transactions on Medical Robotics and Bionics*, vol. 2, no. 2, pp. 269–281, 2020.
- [34] J. Wilson, “Fibres, yarns and fabrics: fundamental principles for the textile designer,” in *Textile Design: Principles, Advances, and Applications*. Woodhead Publishing, 2011, pp. 3–30.
- [35] M. M. Platt, “Mechanics of elastic performance of textile materials: part IV: some aspects of stress analysis of textile structures—staple—fiber yarns,” *Textile Research Journal*, vol. 20, no. 8, pp. 519–538, 1950.
- [36] A. Angelucci, M. Cavicchioli, *et al.*, “Smart textiles and sensorized garments for physiological monitoring: a review of available solutions and techniques,” *Sensors*, vol. 21, no. 3, p. 814, 2021.
- [37] T. Bashir, M. Ali, *et al.*, “Stretch sensing properties of conductive knitted structures of PEDOT-coated viscose and polyester yarns,” *Textile Research Journal*, vol. 84, no. 3, pp. 323–334, 2014.
- [38] Z. Wang, Y. Huang, *et al.*, “Polyurethane/cotton/carbon nanotubes core-spun yarn as high reliability stretchable strain sensor for human motion detection,” *ACS Applied Materials & Interfaces*, vol. 8, no. 37, pp. 24 837–24 843, 2016.

-
- [39] J. Wang, P. Xue, and X. Tao, "Strain sensing behavior of electrically conductive fibers under large deformation," *Materials Science and Engineering: A*, vol. 528, no. 6, pp. 2863–2869, 2011.
- [40] Y. Ko, J.-s. Kim, *et al.*, "Ultrasensitive strain sensor based on pre-generated crack networks using Ag nanoparticles/single-walled carbon nanotube (SWCNT) hybrid fillers and a polyester woven elastic band," *Sensors*, vol. 21, no. 7, p. 2531, 2021.
- [41] S. J. Kim, W. Song, *et al.*, "High durability and waterproofing rgo/swcnt-fabric-based multifunctional sensors for human-motion detection," *ACS Applied Materials & Interfaces*, vol. 10, no. 4, pp. 3921–3928, 2018.
- [42] C. J. Brinker, "Dip coating," in *Chemical Solution Deposition of Functional Oxide Thin Films*. Springer, 2013, pp. 233–261.
- [43] E. Bihar, T. Roberts, *et al.*, "Fully printed electrodes on stretchable textiles for long-term electrophysiology," *Advanced Materials Technologies*, vol. 2, no. 4, p. 1600251, 2017.
- [44] G. Acar, O. Ozturk, *et al.*, "Wearable and flexible textile electrodes for biopotential signal monitoring: a review," *Electronics*, vol. 8, no. 5, p. 479, 2019.
- [45] A. Walker, "Metalization of functionalized surfaces," in *Encyclopedia of Interfacial Chemistry: Surface Science and Electrochemistry*. Elsevier, 2018, pp. 752–760.
- [46] G. Faraji, H. S. Kim, and H. T. Kashi, "Introduction," in *Severe Plastic Deformation: Methods, Processing and Properties*. Elsevier, 2018, pp. 1–17.
- [47] K. M. Jansen, "Performance evaluation of knitted and stitched textile strain sensors," *Sensors*, vol. 20, no. 24, p. 7236, 2020.
- [48] J. Xie, H. Long, and M. Miao, "High sensitivity knitted fabric strain sensors," *Smart Materials and Structures*, vol. 25, no. 10, p. 105008, 2016.
- [49] Y. Li, X. Miao, *et al.*, "Sensing performance of knitted strain sensor on two-dimensional and three-dimensional surfaces," *Materials & Design*, vol. 197, p. 109273, 2021.
- [50] O. Atalay and W. R. Kennon, "Knitted strain sensors: impact of design parameters on sensing properties," *Sensors*, vol. 14, no. 3, pp. 4712–4730, 2014.
- [51] O. Tangsirinaruenart and G. Stylios, "A novel textile stitch-based strain sensor for wearable end users," *Materials*, vol. 12, no. 9, p. 1469, 2019.
- [52] E. Dupler and L. E. Dunne, "Effects of the textile-sensor interface on stitched strain sensor performance," in *23rd International Symposium on Wearable Computers*, London, United Kingdom, September 9–13 2019, pp. 45–53.
- [53] M. Martínez Estrada, I. Gil, and R. Fernández García, "An alternative method to develop embroidery textile strain sensors," *Textiles*, vol. 1, no. 3, pp. 504–512, 2021.
- [54] S. Y. Park and J.-H. Lee, "Machine embroidered sensors for limb joint movement-monitoring smart clothing," *Sensors*, vol. 21, no. 3, p. 949, 2021.

- [55] Y. Liu, L. Liu, *et al.*, “3D network structure and sensing performance of woven fabric as promising flexible strain sensor,” *SN Applied Sciences*, vol. 2, no. 1, pp. 1–13, 2020.
- [56] Q. Lin, S. Peng, *et al.*, “E-jacket: posture detection with loose-fitting garment using a novel strain sensor,” in *19th ACM/IEEE International Conference on Information Processing in Sensor Networks (IPSN)*, Sydney, NSW, Australia, April 21–24 2020, pp. 49–60.
- [57] Y. Jin, C. M. Glover, *et al.*, “Soft sensing shirt for shoulder kinematics estimation,” in *IEEE International Conference on Robotics and Automation (ICRA)*, Paris, France, May 31–August 31, 2020, pp. 4863–4869.
- [58] H. Park, J. Cho, *et al.*, “Sim-to-real transfer learning approach for tracking multi-dof ankle motions using soft strain sensors,” *IEEE Robotics and Automation Letters*, vol. 5, no. 2, pp. 3525–3532, 2020.
- [59] R. Wu, L. Ma, *et al.*, “Fibrous inductance strain sensors for passive inductance textile sensing,” *Materials Today Physics*, vol. 15, p. 100243, 2020.
- [60] Y. Liu, M. Wang, *et al.*, “Embroidered inductive strain sensor for wearable applications,” in *IEEE International Conference on Pervasive Computing and Communications Workshops (PerCom Workshops)*, Austin, TX, USA, March 23–27, 2020, pp. 1–6.
- [61] A. García Patiño, M. Khoshnam, and C. Menon, “Wearable device to monitor back movements using an inductive textile sensor,” *Sensors*, vol. 20, no. 3, p. 905, 2020.
- [62] J. Zhou, X. Xu, *et al.*, “Coaxial thermoplastic elastomer-wrapped carbon nanotube fibers for deformable and wearable strain sensors,” *Advanced Functional Materials*, vol. 28, no. 16, p. 1705591, 2018.
- [63] A. Atalay, V. Sanchez, *et al.*, “Batch fabrication of customizable silicone-textile composite capacitive strain sensors for human motion tracking,” *Advanced Materials Technologies*, vol. 2, no. 9, p. 1700136, 2017.
- [64] C. C. Vu and J. Kim, “Highly sensitive e-textile strain sensors enhanced by geometrical treatment for human monitoring,” *Sensors*, vol. 20, no. 8, p. 2383, 2020.
- [65] B. M. Li, I. Kim, *et al.*, “Kirigami-inspired textile electronics: KITE,” *Advanced Materials Technologies*, vol. 4, no. 11, p. 1900511, 2019.
- [66] J. G. Colli Alfaro and A. L. Trejos, “Design and fabrication of embroidered textile strain sensors: an alternative to stitch-based strain sensors,” *Sensors*, vol. 23, no. 3, p. 1503, 2023.
- [67] V. Murphy, B. P. Edmonds, and A. L. Trejos, “Characterisation and control of a woven biomimetic actuator for wearable neurorehabilitative devices,” *Actuators*, vol. 10, no. 2, p. 37, 2021.
- [68] R. Xu, X. Zheng, *et al.*, “Enhancing the linearity and stability of a fabric-based strain sensor with microfolded graphene structures,” *Applied Sciences*, vol. 10, no. 18, p. 6230, 2020.
- [69] N. Qaiser, F. Al-Modaf, *et al.*, “A robust wearable point-of-care CNT-based strain sensor for wirelessly monitoring throat-related illnesses,” *Advanced Functional Materials*, vol. 31, no. 29, p. 2103375, 2021.

-
- [70] S. Pal, D. Sarkar, *et al.*, “Design, development and analysis of a conductive fabric based flexible and stretchable strain sensor,” in *3rd International Conference on Advances in Mechanical Engineering (ICAME)*, ser. IOP Conference Series: Materials Science and Engineering, no. 912, Chennai, India, February 24–29 2020, p. 022009.
- [71] K. Elgeneidy, G. Neumann, *et al.*, “Directly printable flexible strain sensors for bending and contact feedback of soft actuators,” *Frontiers in Robotics and AI*, vol. 5, no. 2, pp. 1–14, 2018.
- [72] P. A. Lopes, B. C. Santos, *et al.*, “Reversible polymer-gel transition for ultra-stretchable chip-integrated circuits through self-soldering and self-coating and self-healing,” *Nature Communications*, vol. 12, no. 1, pp. 1–10, 2021.
- [73] M. M. Hasan and M. M. Hossain, “Nanomaterials-patterned flexible electrodes for wearable health monitoring: a review,” *Journal of Materials Science*, vol. 56, no. 27, pp. 14 900–14 942, 2021.
- [74] T. Karthik, P. Ganesan, and D. Gopalakrishnan, “Seams and stitches,” in *Apparel Manufacturing Technology*. CRC Press, 2016, pp. 145–166.
- [75] R. Aigner, A. Pointner, *et al.*, “Embroidered resistive pressure sensors: a novel approach for textile interfaces,” in *2020 CHI Conference on Human Factors in Computing Systems*. Honolulu HI USA: ACM, April 25–30 2020, pp. 1–13.
- [76] A. Shafti, R. B. R. Manero, *et al.*, “Embroidered electromyography: a systematic design guide,” *Transactions on Neural Systems and Rehabilitation Engineering*, vol. 25, no. 9, pp. 1472–1480, 2016.
- [77] R. J. Eike, A. Depping, and A. Cliett, “Technical considerations and specifications for conductive machine embroidery,” *Trends in Textile Engineering and Fashion Technology*, vol. 6, pp. 687–696, 2020.
- [78] S. Park, S. Ahn, *et al.*, “Highly bendable and rotational textile structure with prestrained conductive sewing pattern for human joint monitoring,” *Advanced Functional Materials*, vol. 29, no. 10, p. 1808369, 2019.
- [79] S. Wilson and R. Laing, “Fabrics and garments as sensors: a research update,” *Sensors*, vol. 19, no. 16, p. 3570, 2019.
- [80] T. Karthik, P. Ganesan, and D. Gopalakrishnan, “Sewing thread and needles,” in *Apparel Manufacturing Technology*. CRC Press, 2016, pp. 123–144.
- [81] N. A. Choudhry, A. Rasheed, *et al.*, “Design, development and characterization of textile stitch-based piezoresistive sensors for wearable monitoring,” *IEEE Sensors Journal*, vol. 20, no. 18, pp. 10 485–10 494, 2020.
- [82] S. H. Rho, S. Lee, *et al.*, “Study of the optimization of embroidery design parameters for the technical embroidery machine: derivation of the correlation between thread consumption and electrical resistance,” *Textile Research Journal*, pp. 1550–1564, 2022.

-
- [83] Python Software Foundation, “Python language reference,” version 3.9. Available at <http://www.python.org>.
- [84] J. L. Guinón, E. Ortega, *et al.*, “Moving average and savitzki-golay smoothing filters using mathcad,” in *International Conference on Engineering Education (ICEE)*, Coimbra, Portugal, September 3–7 2007, pp. 1–4.
- [85] M. Müller, “Dynamic time warping,” in *Information Retrieval for Music and Motion*. Springer, 2007, vol. 2, pp. 69–84.
- [86] J. Tarango, E. Keogh, and P. Brisk, “Instruction set extensions for dynamic time warping,” in *IEEE International Conference on Hardware/Software Codesign and System Synthesis (CODES+ ISSS)*, Montreal, QC, Canada, September 29– October 4 2013, pp. 1–10.
- [87] B. Oldfrey, R. Jackson, *et al.*, “A deep learning approach to non-linearity in wearable stretch sensors,” *Frontiers in Robotics and AI*, vol. 6, pp. 1–16, 2019.
- [88] X. A. Nguyen and S. Chauhan, “Characterization of flexible and stretchable sensors using neural networks,” *Measurement Science and Technology*, 2021.
- [89] C. Mattmann, F. Clemens, and G. Tröster, “Sensor for measuring strain in textile,” *Sensors*, vol. 8, no. 6, pp. 3719–3732, 2008.
- [90] C. Basla, A. M. Georgarakis, *et al.*, “A stretchable sensor for force estimation in soft wearable robots,” in *IEEE International Conference on Rehabilitation Robotics (ICORR)*, Rotterdam, Netherlands, July 25–29 2022, pp. 1–6.
- [91] D. Kim, J. Kwon, *et al.*, “Adaptive calibration of soft sensors using optimal transportation transfer learning for mass production and long-term usage,” *Advanced Intelligent Systems*, vol. 2, no. 6, p. 1900178, 2020.
- [92] J. G. Colli Alfaro and A. L. Trejos, “User-independent hand gesture recognition classification models using sensor fusion,” *Sensors*, vol. 22, no. 4, p. 1321, 2022.
- [93] S. W. Kang, H. Choi, *et al.*, “The development of an IMU integrated clothes for postural monitoring using conductive yarn and interconnecting technology,” *Sensors*, vol. 17, no. 11, p. 2560, 2017.
- [94] S. Lee, B. Jamil, *et al.*, “Fabric vest socket with embroidered electrodes for control of myoelectric prosthesis,” *Sensors*, vol. 20, no. 4, p. 1196, 2020.
- [95] A. Vogl, P. Parzer, *et al.*, “Stretcheband: Enabling fabric-based interactions through rapid fabrication of textile stretch sensors,” in *Proceedings of the CHI Conference on Human Factors in Computing Systems*, Denver, Colorado, USA, May 6–11, 2017, pp. 2617–2627.
- [96] X. Zou, X. Li, *et al.*, “Detection of lower-limb motion using a kneepad sensor based on textile strain sensor,” in *IEEE 18th International Conference on Nano/Micro Engineered and Molecular Systems (NEMS)*, Jeju Island, Republic of Korea, May 14–17, 2023, pp. 161–164.

- [97] T. J. Cuthbert, B. C. Hannigan, *et al.*, “HACS: helical auxetic yarn capacitive strain sensors with sensitivity beyond the theoretical limit,” *Advanced Materials*, vol. 35, no. 10, p. 2209321, 2023.
- [98] J. S. Meena, S. B. Choi, *et al.*, “Highly stretchable and robust textile-based capacitive mechanical sensor for human motion detection,” *Applied Surface Science*, vol. 613, p. 155961, 2023.
- [99] A. Byberi, R. K. Amineh, and M. Ravan, “Wearable inductive sensing of the arm joint: comparison of three sensing configurations,” *Magnetism*, vol. 2, no. 3, pp. 195–210, 2022.
- [100] S. Tan, M. R. Islam, *et al.*, “Highly scalable, sensitive and ultraflexible graphene-based wearable e-textiles sensor for bio-signal detection,” *Advanced Sensor Research*, vol. 1, no. 1, p. 2200010, 2022.
- [101] B. Aksoy, Y. Hao, *et al.*, “Shielded soft force sensors,” *Nature Communications*, vol. 13, no. 1, p. 4649, 2022.
- [102] L. Verma, I. Karnawal, *et al.*, “Design and fabrication of flexible carbon fabric PDMS based strain sensor for human motion monitoring,” *IEEE Sensors Journal*, vol. 23, no. 15, pp. 16 729–16 735, 2023.
- [103] L. Lu, Z. Li, *et al.*, “Bioinspired strain sensor using multiwalled carbon nanotube/polyvinyl butyral/nylon cloth for wireless sensing applications,” *IEEE Sensors Journal*, vol. 22, no. 13, pp. 12 664–12 672, 2022.
- [104] M. R. Carneiro, L. P. Rosa, *et al.*, “Tailor-made smart glove for robot teleoperation, using printed stretchable sensors,” in *IEEE 5th International Conference on Soft Robotics (RoboSoft)*, Edinburgh, United Kingdom, April 4–8, 2022, pp. 722–728.
- [105] J. Wagner, H. Winger, *et al.*, “Smart glove with fully integrated textile sensors and wireless sensor frontend for the tactile internet,” *IEEE Sensors Letters*, vol. 7, no. 2, pp. 1–4, 2023.
- [106] J. Cheng, F. Xie, and Z. Liang, “Electronic modeling for resistive textile matrices,” *IEEE Sensors Journal*, vol. 22, no. 16, pp. 16 081–16 088, 2022.
- [107] J. Park, S. Park, *et al.*, “Wearable strain sensor using conductive yarn sewed on clothing for human respiratory monitoring,” *IEEE Sensors Journal*, vol. 20, no. 21, pp. 12 628–12 636, 2020.
- [108] L. Devendorf, S. De Koninck, and E. Sandry, “An introduction to weave structure for HCI: a how-to and reflection on modes of exchange,” in *ACM Designing Interactive Systems Conference*, Australia, June 13–17, 2022, pp. 629–642.
- [109] K. Shaker, M. Umair, *et al.*, “Effect of fabric structure on the performance of 3D woven pressure sensor,” *Fibers and Polymers*, vol. 22, pp. 847–853, 2021.
- [110] X. Ding, W. Zhong, *et al.*, “Highly accurate wearable piezoresistive sensors without tension disturbance based on weaved conductive yarn,” *ACS Applied Materials & Interfaces*, vol. 12, no. 31, pp. 35 638–35 646, 2020.

- [111] K. Shimazaki and D. W. Lloyd, "Opening behavior of lockstitch seams in woven fabrics under cyclic loading conditions," *Textile Research Journal*, vol. 60, no. 11, pp. 654–662, 1990.
- [112] A. K. Stavrakis, M. Simić, and G. M. Stojanović, "A study of the performance degradation of conductive threads based on the effects of tensile forces and repeated washing," *Polymers*, vol. 14, no. 21, p. 4581, 2022.
- [113] L. Dong, C. Jiang, *et al.*, "Design of shape reconfigurable, highly stretchable honeycomb lattice with tunable poisson's ratio," *Frontiers in Materials*, vol. 8, p. 660325, 2021.
- [114] C. Liu, J. Cai, *et al.*, "Highly stretchable electromagnetic interference shielding materials made with conductive microcoils confined to a honeycomb structure," *ACS Applied Materials & Interfaces*, vol. 12, no. 10, pp. 12 101–12 108, 2020.
- [115] J. Pu, X. Wang, *et al.*, "Highly stretchable microsupercapacitor arrays with honeycomb structures for integrated wearable electronic systems," *ACS Nano*, vol. 10, no. 10, pp. 9306–9315, 2016.
- [116] W. Kester, J. Bryant, *et al.*, "Sensor signal and conditioning," in *Op Amp Applications Handbook*. Elsevier, 2005, pp. 227–308.
- [117] G. Castro and S. Hunt, "How to stay out of deep water when designing with bridge sensors," *Analog Dialogue*, vol. 48, p. 3, 2014.
- [118] G. Kwakkel, E. E. van Wegen, *et al.*, "Standardized measurement of quality of upper limb movement after stroke: consensus-based core recommendations from the second stroke recovery and rehabilitation roundtable," *Neurorehabilitation and Neural Repair*, vol. 33, no. 11, pp. 951–958, 2019.
- [119] H. J. Asl, M. Yamashita, *et al.*, "Field-based assist-as-needed control schemes for rehabilitation robots," *IEEE/ASME Transactions on Mechatronics*, vol. 25, no. 4, pp. 2100–2111, 2020.
- [120] J. Jeong, K. Hyeon, *et al.*, "Wrist assisting soft wearable robot with stretchable coolant vessel integrated SMA muscle," *IEEE/ASME Transactions on Mechatronics*, vol. 27, no. 2, pp. 1046–1058, 2021.
- [121] B. P. Edmonds, C. T. DeGroot, and A. L. Trejos, "Thermal modeling and characterization of twisted coiled actuators for upper limb wearable devices," *IEEE/ASME Transactions on Mechatronics*, vol. 26, no. 2, pp. 966–977, 2020.
- [122] Y. M. Zhou, D. Wagner, *et al.*, "Soft robotic glove with integrated sensing for intuitive grasping assistance post spinal cord injury," in *IEEE International Conference on Robotics and Automation (ICRA)*, Montreal, QC, Canada, May 20–24, 2019, pp. 9059–9065.
- [123] L. Osborn, W. W. Lee, *et al.*, "Tactile feedback in upper limb prosthetic devices using flexible textile force sensors," in *5th IEEE RAS/EMBS International Conference on Biomedical Robotics and Biomechatronics*, Sao Paulo, Brazil, August 12–15, 2014, pp. 114–119.

-
- [124] Y. G. Kim, J.-H. Song, *et al.*, “Piezoelectric strain sensor with high sensitivity and high stretchability based on kirigami design cutting,” *Npj Flexible Electronics*, vol. 6, no. 1, p. 52, 2022.
- [125] Y. Wang and C. Wang, “Buckling of ultrastretchable kirigami metastructures for mechanical programmability and energy harvesting,” *International Journal of Solids and Structures*, vol. 213, pp. 93–102, 2021.
- [126] M. Isobe and K. Okumura, “Initial rigid response and softening transition of highly stretchable kirigami sheet materials,” *Scientific Reports*, vol. 6, no. 1, p. 24758, 2016.
- [127] T. C. Shyu, P. F. Damasceno, *et al.*, “A kirigami approach to engineering elasticity in nanocomposites through patterned defects,” *Nature Materials*, vol. 14, no. 8, pp. 785–789, 2015.
- [128] E. Sanmiguel-Rojas, M. Hidalgo-Martínez, *et al.*, “Analytical approaches to oscillators with nonlinear springs in parallel and series connections,” *Mechanism and Machine Theory*, vol. 93, pp. 39–52, 2015.
- [129] V. Falzarano, F. Marini, *et al.*, “Devices and protocols for upper limb robot-assisted rehabilitation of children with neuromotor disorders,” *Applied Sciences*, vol. 9, no. 13, p. 2689, 2019.
- [130] Y. Cho, G. T. Nguyen, *et al.*, “Time-evolution of electrical resistance-strain hysteresis curve of embroidered stretch sensors and their application in reliable human motion tracking,” *Journal of Mechanical Science and Technology*, vol. 36, no. 7, pp. 3573–3584, 2022.
- [131] J. Austin, A. Schepelmann, and H. Geyer, “Control and evaluation of series elastic actuators with nonlinear rubber springs,” in *IEEE/RSJ International Conference on Intelligent Robots and Systems (IROS)*, Hamburg, Germany, September 28–October 2, 2015, pp. 6563–6568.

Appendix A

Permissions and Approvals

MDPI Open Access Information and Policy

All articles published by MDPI are made immediately available worldwide under an open access license. This means:

- everyone has free and unlimited access to the full-text of *all* articles published in MDPI journals;
- everyone is free to re-use the published material if proper accreditation/citation of the original publication is given;
- open access publication is supported by the authors' institutes or research funding agencies by payment of a comparatively low **Article Processing Charge (APC)** for accepted articles.

Permissions

No special permission is required to reuse all or part of article published by MDPI, including figures and tables. For articles published under an open access Creative Common CC BY license, any part of the article may be reused without permission provided that the original article is clearly cited. Reuse of an article does not imply endorsement by the authors or MDPI.

Copyright and Licensing

For all articles published in MDPI journals, copyright is retained by the authors. Articles are licensed under an open access Creative Commons **CC BY 4.0 license** meaning that anyone may download and read the paper for free. In addition, the article may be reused and quoted provided that the original published version is cited. These conditions allow for maximum use and exposure of the work, while ensuring that the authors receive proper credit.

In exceptional circumstances articles may be licensed differently. If you have specific condition (such as one linked to funding) that does not allow this license, please mention this to the editorial office of the journal at submission. Exceptions will be granted at the discretion of the publisher.

Curriculum Vitae

José Guillermo Collí Alfaro

Education

- Jan. 2020 – Present PhD, Biomedical Engineering, Robotics, University of Western Ontario, London, Ontario, Canada
Thesis: Analysis and Characterization of Embroidered Textile Strain Sensors
Supervisor: Dr. Ana Luisa Trejos
- Sept. 2017 – Aug. 2019 MEng, Biomedical Engineering, Robotics, University of Western Ontario, London, Ontario, Canada
Thesis: Implementation of User-Independent Hand Gesture Recognition Classification Models Using IMU and EMG-based Sensor Fusion Techniques
Supervisor: Dr. Ana Luisa Trejos
- Sept. 2009 – Jul. 2013 BEng, Biomedical Engineering, Modelo University, Merida, Yucatan, Mexico

Honours and Awards

- 2022 Canadian MSK Rehab Research Network Travel Award
- 2020 – 2023 Mexican National Council of Science and Technology (CONACYT) Graduate Scholarship Award (PhD)
- 2019 Western University School of Biomedical Engineering Travel Award
- 2017 – 2019 Mexican National Council of Science and Technology (CONACYT) Graduate Scholarship Award (Masters)
- 2016 Mexico INTO by CANIETI International Summer Research Scholarship Award

Research Experience

- Jan. 2020 – Present **Graduate Research Assistant**, University of Western Ontario, Wearable Biomechatronics Laboratory (WearMe Lab)
Designed and developed embroidered textile strain sensors for use in wearable mechatronic devices. Processed and analyzed neck EMG data as part of a project related to a neck rehabilitation device.
- Sept. 2017 – Aug. 2019 **Graduate Research Assistant**, University of Western Ontario, Wearable Biomechatronics Laboratory (WearMe Lab)
Implemented user-independent hand gesture recognition classification models using inertial measurement units (IMU) and surface electromyography (EMG)-based sensor fusion techniques.

May 2016 – **Summer Research Assistant**, Texa A&M University, Human Rehabilitation
Aug. 2016 Group (HUR Group)
Designed and developed virtual environments for use in conjunction with a skin stretch feedback system for post-stroke rehabilitation.

Industry Experience

Apr. 2014 – **Biomedical Engineer**, Star Medica Hospital, Merida, Yucatan, Mexico
May 2016

Teaching Experience

Sep. 2018 – **Graduate Teaching Assistant**, University of Western Ontario, School of
Dec. 2023 Biomedical Engineering
MSE 4401 – Robotic Manipulators
MSE 2202 – Introduction to Mechatronic Design
MSE 3302 – Sensors and Actuators
BME 3201 – Foundations in Biomedical Engineering Design
BME 9508 – Fundamentals of Biomedical Engineering
MME 4452 – Robotics and Manufacturing Engineering Automation
Jul. 2018 – **Biomedical Engineering Summer Academy Instructor**, University of
Aug. 2018 Western Ontario, Western Engineering Summer Academy
Day long workshop where high-school students soldered and assembled an EMG-activated prosthetic finger actuated with a shape memory alloy.
Jan. 2017 – **Course Instructor**, Modelo University, Department of Biomedical Engineer-
Jun. 2017 ing, Merida, Yucatan, Mexico
Course: Installation and Maintenance of Medical Equipment.

Supervisory Experience

May 2023 – Supervision of an undergraduate student project involving the design of a brad-
Aug. 2023 ing machine for e-textile applications.
May 2023 – Supervision of an undergraduate student project involving the design and de-
Aug. 2023 velopment of woven textile strain sensors.
Feb. 2023 – Supervision of a high school co-op student project involving the mechanical
Jun. 2023 characterization of textile sensors.
Sep. 2022 – Supervision of a high school co-op student project involving iterating the pro-
Feb. 2023 totype design of a testing setup for embroidered textile sensors.
May 2022 – Supervision of an undergraduate student project involving the design of em-
Aug. 2022 broidered textile electrodes for biosignals acquisition applications.

Publications

J. G. Colli Alfaro and A. L. Trejos, “Design and fabrication of embroidered textile strain sensors: an alternative to stitch-based strain sensors,” *Sensors*, vol. 23, no. 3, p. 1503, 2023.

T. K. Stanbury, J. G. Colli Alfaro, *et al.*, “Identifying interaction forces via EMG under changing motion dynamics,” in *IEEE International Conference on Rehabilitation Robotics (ICORR)*, Rotterdam, Netherlands, July 25–29, 2022, pp. 1–6.

J. G. Colli Alfaro and A. L. Trejos, “User-independent hand gesture recognition classification models using sensor fusion,” *Sensors*, vol. 22, no. 4, p. 1321, 2022.

J. G. Colli Alfaro, A. Ibrahim, and A. L. Trejos, “Design of user-independent hand gesture recognition using multilayer perceptron networks and sensor fusion techniques,” in *IEEE 16th International Conference on Rehabilitation Robotics*, Toronto, Ontario, Canada, June 24–28, 2019, pp. 1103–1108.

F. J. Heredia López, F. J. Álvarez Cervera, J. G. Colli Alfaro, *et al.*, “An automated y-maze based on a reduced instruction set computer (RISC) microcontroller for the assessment of continuous spontaneous alternation in rats,” *Behavior Research Methods*, vol. 48, pp. 1631–1643, 2016.

Presentations

J. G. Colli Alfaro and A. L. Trejos, “User-Independent Hand Gesture Recognition Using Sensor Fusion Techniques,” *Canadian Bone and Joint Conference*, Virtual Presentation, London, Ontario, Canada, Jun. 12–13, 2020.

Volunteer Experience

Oct. 2018 – Aug. 2023	Lab Outreach Tour Demonstrations , Wearable Biomechatronics Laboratory (WearMe Lab), University of Western Ontario Demonstrated different EMG applications during high-school class tours and university open houses.
Dec. 2018	FIRST Lego League Judge , Western Engineering FIRST LEGO League London Qualifier, University of Western Ontario Participated as a judge in the FIRST Lego League where elementary and middle school students demonstrated their technical and innovative skills to build lego-based robots to complete different challenges.

Professional Memberships

Apr. 2022 – Present	Graduate Student Member, International Consortium for Rehabilitation Robotics (ICORR)
Apr. 2019 – Dec. 2019	Graduate Student Member, Institute of Electrical and Electronics Engineers (IEEE)